

Autonomous Computational Catalysis Research via Agentic Systems

Honghao Chen¹, Jiangjie Qiu¹, Yi Shen Tew¹, Xiaonan Wang^{1*}

¹Beijing Key Laboratory of Artificial Intelligence for Advanced
Chemical Engineering Materials, Department of Chemical Engineering,
Tsinghua University, Beijing, China.

*Corresponding author(s). E-mail(s): wangxiaonan@tsinghua.edu.cn;

Abstract

Fully automating the scientific process is a transformative ambition in materials science, yet current artificial intelligence masters isolated workflow fragments. In computational catalysis, a system autonomously navigating the entire research lifecycle from conception to a scientifically meaningful manuscript remains an open challenge. Here we present CatMaster, a catalysis-native multi-agent framework that couples project-level reasoning with the direct execution of atomistic simulations, machine-learning modelling, literature analysis, and manuscript production within a unified autonomous architecture. Across progressively demanding evaluations, CatMaster achieves perfect scores on four end-to-end short-form catalysis scenarios, reaches near-leaderboard performance on five of six MatBench tasks, performs self-discovery of reaction mechanisms grounded in literature or from scratch, and executes a fully closed-loop single-atom catalyst design problem. Together, these results show that end-to-end autonomous computational catalysis is now practical for research programmes, while highlighting that bridging the gap to genuine scientific closure requires tighter integration with reliable physical engines and domain-rigorous methodologies.

1 Introduction

Artificial intelligence has served as a powerful accelerant for scientific discovery in the past decade, yet historically, its application has remained confined to narrow, well-posed tasks within rigid problem formulations. The advent of modern foundation models has radically expanded this horizon, elevating AI from a tool for

focused prediction and optimization to a dynamic participant in broader scientific reasoning encompassing hypothesis generation, experimental design, data analysis, and manuscript preparation.[1–3] Consequently, the emergence of end-to-end AI pipelines and autonomous co-scientists has triggered a fundamental paradigm shift: the frontier of AI for science is no longer the automation of isolated components, but the autonomous orchestration of entire, comprehensive research lifecycles.[2, 3] In chemistry and materials science, this evolution will be particularly impactful. Much of the discovery process already unfolds computationally, relying on density functional theory (DFT) and atomistic simulations as the fundamental engines connecting molecular structure, energetics and catalytic function.[4] Therefore, the ultimate objective is no longer the mere automation and acceleration of calculations, but the realization of intelligent systems capable of autonomously organizing, critiquing, and dynamically adapting complex computational research.

This transformative shift builds upon a deeply mature computational ecosystem, which provides the necessary scaffolding through general-purpose libraries (e.g., ASE and pymatgen), robust workflow managers (e.g., FireWorks and AiiDA), and vast shared data infrastructures (e.g., the Materials Project).[5–9] Concurrently, agentic systems tailored for chemistry and materials are advancing rapidly across distinct trajectories. Frameworks such as El Agente, Quntur and Sólido focus on natural-language-driven quantum and solid-state simulations; SciToolAgent emphasizes cross-domain tool integration; ChemGraph and DREAMS cast atomistic workflows as agentic tasks; TritonDFT explores multi-agent automation for DFT calculations; and recent catalyst-design studies have begun to couple language models to bounded screening settings, including limited-environment optimization and predefined single-atom ORR workflows.[10–19] Collectively, these efforts signal a swift progression from proof-of-concept assistants toward capable autonomous research systems.

Nevertheless, a critical divide persists between generalized workflow automation and the realization of a truly catalysis-native computational co-scientist. Current intelligent systems are predominantly optimized either for broad, shallow tool orchestration or for rigid, predefined screening loops. In stark contrast, computational catalysis inherently demands a far deeper and more dynamic integration. To sustain genuine scientific inquiry, an agent must seamlessly execute tasks between executing rigorous atomistic calculations, synthesizing literature-grounded physical interpretations, systematically exploring complex scientific landscape, all within a single, cohesive, and continuously pursuing answers for open-ended questions, or so-called scientific discovery.[4]

To bridge this gap, we introduce CatMaster, an autonomous AI agent system engineered specifically for the rigorous demands of computational catalysis and materials science. Rather than treating autonomy as the ability to call tools in correct sequence and parameters, CatMaster is architected around a far foundational requirement: the ability to sustain complete computational research cycles. Within this framework, high-level planning, precise execution, critical evidence inspection, physical interpretation, and manuscript drafting remain linked to a singular scientific objective. This formulation shifts the question from whether language-model agents can assist with

chemistry workflows, to whether they can reliably sustain and advance a complex research across fundamentally diverse modes of scientific inquiry.

We therefore examine CatMaster across a progression of increasingly demanding scientific environments: concise benchmark scenarios, general-purpose materials machine-learning modelling, reaction-mechanism rediscovery and network exploration, and finally a closed-loop single-atom-catalyst design case. Taken together, these comprehensive case studies indicate the current frontier of scientific AI agentic systems are already approaching end-to-end practical usefulness for computational catalysis, while demonstrating that genuine scientific closure still demands the domain-specific rigor or specialized catalysis tools and algorithms.

2 Results

2.1 Agent System Framework

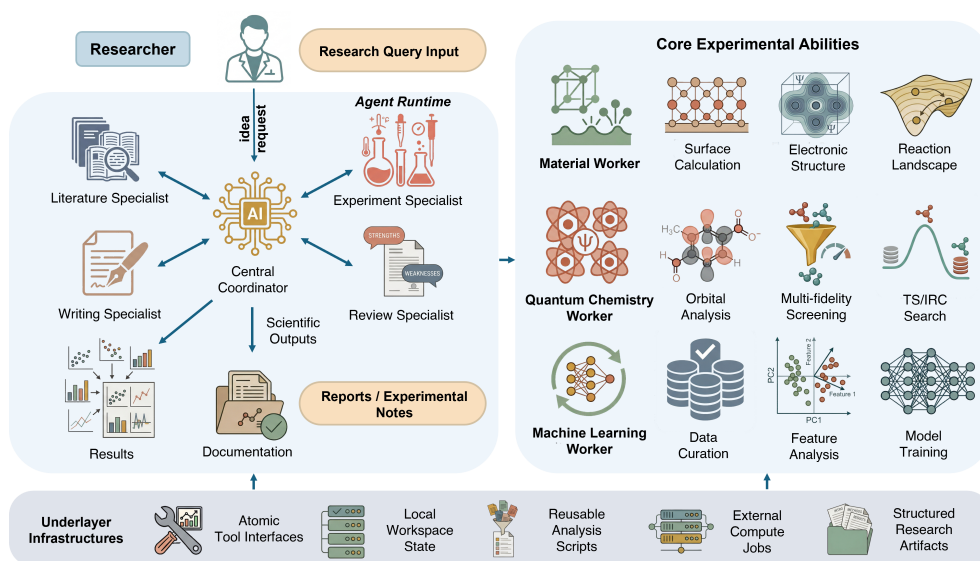


Fig. 1 Conceptual overview of the CatMaster runtime. In the upper agent layer, a central research specialist coordinates the scientific campaign and delegates tasks to four domain specialists: experiment, literature review, writing, and peer review. These specialists then route work to the appropriate downstream workers and tools for atomistic simulation, machine learning, quantum chemistry, manuscript preparation, and critical assessment. Beneath this agent layer, a parallel lower execution layer handles orchestration, artifact management, and interfaces to external computational resources, enabling a closed-loop computational catalysis workflow.

Realizing a true computational co-scientist requires an AI system to move beyond executing isolated computational tasks. It demands an organizational structure that

mirrors actual scientific workflows: maintaining a clear project-level objective, delegating technical work to domain experts, and synthesizing results for interpretation, validation, and publication. CatMaster is explicitly designed around this principle (Fig. 1). A top-level coordinator steers the research direction and manages the lifecycle of active hypotheses, while specialized agents integrate computational execution, literature synthesis, manuscript drafting, and simulated peer review into a cohesive, closed-loop system.

Two design choices are central to this architecture. First, CatMaster employs a shallow agent hierarchy. Specialization is introduced only when a task demands a fundamentally different scientific mode of operation or research area, mirroring the natural division between execution, review, and writing in real-world research. This flat structure keeps high-level reasoning close to the underlying workers that manipulate scientific artifacts, thereby minimizing information loss during extended computational campaigns. Second, CatMaster decouples what the system can execute from how it applies scientific knowledge. Instead of tools that attempt to execute specific workflows, the system’s tool surface comprises narrow but general primitives acting on concrete artifacts (e.g., atomic structures, calculation directories, datasets, models, and manuscript files). Domain-specific expertise is then injected via plug-and-play skill modules, which orchestrate these primitives for more complex tasks like adsorption screening, transition-state search, machine-learning modelling, and scientific writing. Consequently, CatMaster expands its scientific coverage by composing reusable procedures instead of hard-coding rigid workflows. Moreover, beneath the agentic layer, a dedicated orchestration layer manages local workspaces, artifact routing, and interfaces with external computational resources, such as batch job schedulers, making the system ready for complex research resources management. A comprehensive inventory of these roles, tools, and execution interfaces is provided in the Methods and Supplementary Information.

Together, these design principles do more than streamline workflows; they bridge the critical gap between abstract AI reasoning and rigorous physical science. Because its tools operate directly on concrete artifacts, CatMaster can iteratively construct a structured, reusable scientific product collection, ranging from validated thermodynamic data and energy barriers to drafted manuscript sections. This tight coupling of agentic reasoning with data production is the engine of its sustained autonomy. By directly parsing, evaluating, and learning from its own generated evidence, the system independently determines the next logical step in a research cycle without requiring constant human intervention. Powered by this closed-loop mechanism, a single unified runtime can navigate the broad space of computational catalysis. In the following sections, we evaluate these capabilities across a progression of four distinct stages: foundational validation on standard computational task benchmarks, generalized materials machine-learning modelling, canonical reaction-mechanism rediscovery, and an open-ended single-atom-catalyst design case.

2.2 Benchmarking on Standard Computational Scenarios

We first evaluated CatMaster on four benchmark scenarios that cover core computational catalysis operations: materials retrieval and DFT setup selection (T1), CO

adsorption screening on Fe(110) (T2), a MACE-only transition-state benchmark on Au(111)-O (T3), and density-of-states (DOS) analysis for three bulk materials (T4) (Fig. 2a). Importantly, these were not single-step or single-tool microbenchmarks. Each run started from a natural-language request and was scored only after the system completed the entire sequence from workspace initialization to concrete scientific outputs. This included preparing inputs, executing calculations, generating visualizations, and writing a summary report. This end-to-end requirement distinguishes our approach from recent agentic studies. [16] Practically, important failures usually only emerge when multiple reasoning, execution, and reporting steps are combined into a single scenario, which may be hard to observe in narrow workflow slices or limited screening operations. [14]

Under this rigorous testing, a performance gap emerged between the top two models and the others (Fig. 2b). GPT-5.4 achieved a perfect human-reviewed score of 100% across all four scenarios, closely followed by Sonnet-4.6 at 98%. Gemini-3.1 Pro reached 87.7%, and Mimo-V2 Pro (Hunter Alpha) scored 82.5%. This performance gap represents a critical bottleneck for scaling up autonomous workflows. Because long research cycles are built by compounding many short scenarios like these, even minor error rates increase exponentially over time. Therefore, near-ceiling reliability at the single-scenario level is a prerequisite for long-horizon operation. By this measure, GPT-5.4 and Sonnet-4.6 operate in a distinctly higher tier than the other two models.

For the remaining systems, performance dropped for distinctly different reasons, and specific scenarios highlighted exactly how these limitations play out in practice (Fig. 2c). Gemini-3.1 Pro showed strong scientific competence and often produced chemically reasonable outputs, but its score dropped mainly due to incomplete scenario closure rather than major physical mistakes. This was most obvious in the T2 adsorption and T4 DOS scenarios, where missing final summaries or incomplete computational tasks lowered the scores. In contrast, Mimo-V2 Pro exhibited much higher run-to-run variance, showing a clear gap between "good" and "reliable" behavior due to reasoning stability. This weakness was starkly exposed in the T4 DOS scenario, where it suffered a near-catastrophic failure by incorrectly restarting an earlier step, entirely failing to produce the requested outputs.

Interestingly, even the strongest models occasionally showed narrow blind spots when tracking deep mechanistic context. For instance, in the T3 transition-state scenario, Sonnet-4.6 successfully completed the NEB calculation but mistakenly performed the vibrational analysis on the endpoint minimum rather than the transition-state image, leading to its only consistent point loss across the benchmark. This further highlights that agents must be able to actively deduce implicit physical requirements when the exact next step is under-specified according to the task context. Taken together, these results demonstrate that the main difference between these models is not their basic domain knowledge. Rather, the true gap lies in their ability to handle errors, maintain stability during post-processing, and successfully guide a scientific task through to a complete and reliable conclusion.

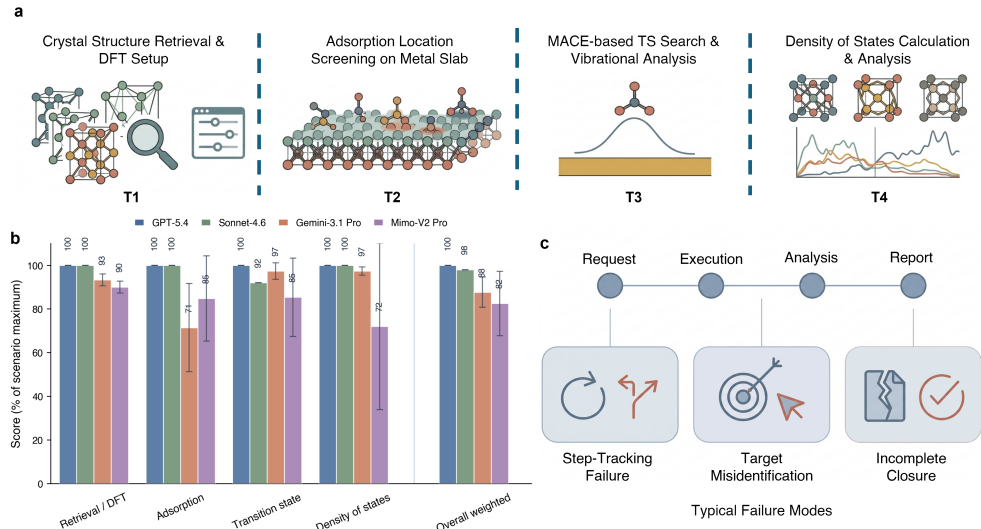


Fig. 2 Benchmarking CatMaster on four standard computational scenarios. **(a)**, Schematic illustrations of the benchmark scenarios: materials retrieval and DFT-parameter selection (T1), adsorption screening on Fe(110) (T2), MACE-only transition-state benchmarking on Au(111) (T3), and density-of-states analysis (T4). **(b)**, Scenario-normalized scores for four contemporary model backends under the CatMaster runtime, with bars showing means over three independent repeats and error bars showing repeat standard deviations. **(c)**, Schematic summary of the dominant failure structure across the full scenario chain from *Request* to *Report*. Scores shown here follow the human-reviewed benchmark ledger detailed in the Supplementary Information.

2.3 General-Purpose ML Modelling capability

To evaluate CatMaster’s capacity for autonomous data science, we next tested its ability to construct and optimize complete materials machine learning pipelines from scratch. To test this, we selected six MatBench scenarios spanning composition-only and structure-aware inputs, regression and classification targets, and dataset sizes ranging from 312 to 106,113 samples.[20] The selected scenarios comprised *steels*, *expt_gap*, *is_glass*, *jdft2d*, *mp_is_metal*, and *phonons*. Each run began from the same natural-language request and required CatMaster to try up to five strategies, deciding on feature engineering and model families, then implementing reproducible code and performing MatBench-compliant model selection and held-out evaluation. Importantly, the runtime was not given one fixed modelling recipe. Instead, each scenario permitted up to five internal strategy rounds, allowing the agent to dynamically decide whether a task favored descriptor-based tabular models, structure-aware handcrafted features, hybrid ensembles, or graph neural networks (GNNs).

In five of the six scenarios, a single autonomous CatMaster episode reached best or near-best performance relative to the MatBench leaderboard baselines used for comparison (Fig. 3). CatMaster ranked first on *jdft2d* (33.09 meV atom⁻¹ MAE; Fig. 3b) and *mp_is_metal* (0.9787 ROC-AUC; Fig. 3e), and second on *steels* (80.66 MAE; Fig. 3c), *expt_gap* (0.3025 eV MAE; Fig. 3a), and *is_glass* (0.9524 ROC-AUC;

Fig. 3d). These outcomes are notable because they were obtained as end-to-end autonomous modelling episodes rather than through manual architecture selection or specialized AutoML searching algorithm. Inspection of the saved workspaces reveals a consistent adaptive pattern under the fixed five strategy search budget used here. For composition-dominant scenarios such as *steels*, *expt_gap*, and *is_glass*, CatMaster converged on descriptor-heavy tabular workflows, typically employing ExtraTrees or XGBoost variants over matminer- or pymatgen-derived features. For structure-dependent scenarios it widened the representation: on *jdft2d* it assembled composition, 2D geometry, and CrystalNN-derived site statistics before selecting a weighted ExtraTrees-HistGradientBoosting ensemble; on *mp_is_metal* it combined composition, elemental fractions, lightweight structure descriptors, and neighbor statistics into a 322-feature XGBoost pipeline. These varied architectural choices indicate that the system successfully emulates the standard practice of a human data scientist by testing a bounded set of inductive biases according to the data properties, selecting the strongest candidate via robust cross-validation, and executing the entire pipeline autonomously.

The *phonons* scenario, however, exposed a distinct limitation (Fig. 3f). Success on this task strictly demands specialized, geometry-aware architectures rather than the general-purpose representations that succeeded earlier. In the first autonomous run, CatMaster’s strongest single model was not the graph network but a handcrafted descriptor search. The final selected model was a validation-weighted blend between that descriptor model and a weaker crystal GNN, yielding an MAE of 45.56 cm^{-1} . Because this lagged well behind the strongest specialized MatBench phonon models, a second self-improvement episode was explicitly authorized (shown separately in Fig. 3f). During this second trial, CatMaster repaired a broken symmetry-feature path, introduced proper XGBoost early stopping, replaced a single holdout set with inner cross-fitted CV, added SOAP descriptors to a routed specialist stack, and tested a new angle-aware graph component. The overall result improved to 37.69 cm^{-1} MAE, but it still remained behind the specialist leaders. Furthermore, the new angle-aware graph pilot underperformed and was not promoted into the final ensemble. This shows while CatMaster is highly capable of reconstructing strong, reproducible materials-ML pipelines across diverse modalities under finite budgets, it cannot yet autonomously discover or faithfully adapt frontier geometry-rich architectures when the model architecture itself is the core scientific bottleneck.

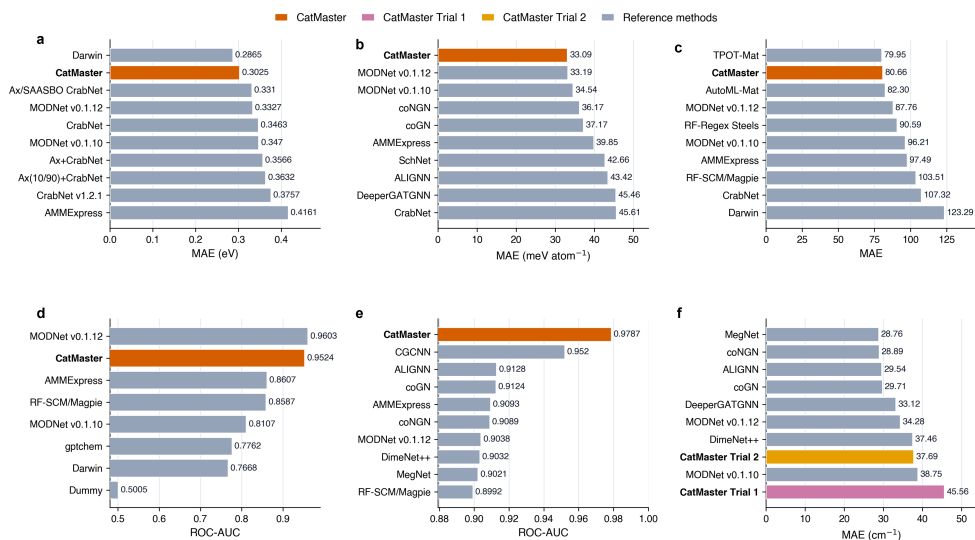


Fig. 3 Comparison of CatMaster against representative MatBench baselines across six general-purpose modelling scenarios: **a**, *expt_gap*; **b**, *jdft2d*; **c**, *steels*; **d**, *is_glass*; **e**, *mp_is_metal*; and **f**, *phonons*. Each panel shows CatMaster together with up to nine of the strongest reference methods reported in the corresponding MatBench baselines, while the *phonons* panel includes both CatMaster trials to illustrate the observed two-trial self-improvement.

2.4 Reaction Mechanistic Validation and Network Exploration

We next evaluated CatMaster’s capacity to execute complex mechanistic studies, a challenge that requires translating symbolic chemical intuition into rigorous geometric state construction and pathway verification. CO oxidation on Pt(111) served as a compact rediscovery baseline. In contrast, the reverse water-gas shift (RWGS) reaction on Cu(111) was selected as a demanding counterpart; its complex binding adsorption landscape makes both endpoint locality and path validity more difficult to establish. For both systems, CatMaster was tasked with selecting a low-coverage slab, enumerating candidate minima, launching NEB calculations, auditing path quality, and synthesizing a mechanistic summary.

On the Pt(111) surface, CatMaster successfully recovered the canonical low-coverage mechanism. Operating on a $3 \times 3 \times 4$ slab, it identified stable CO adsorption on atop sites, shallow molecular O_2 precursor states, a lower-energy dissociated $O^* + O^*$ basin, and a direct $O^* + CO^*$ oxidation event as the rate-controlling step. The computed energy barriers were 0.412 eV for O diffusion, 0.952 eV for O_2 dissociation, and 1.129 eV for direct oxidation. Following approximate thermodynamic corrections at 400 K, the direct oxidation step correctly remained the kinetic bottleneck with a 1.114 eV free-energy barrier (Fig. 4b). Although the system also explored an explicit molecular O_2 -assisted branch (Fig. 4a), no competitive barrier survived its rigorous internal acceptance criteria. Rather than merely reproducing a single

expected value, the system accurately reconstructed the accepted mechanistic hierarchy, confirming that dissociative O_2 activation feeds a lower-energy basin and that the Langmuir–Hinshelwood mechanism dictates the macroscopic rate.

Given the geometric complexity of the Cu(111) landscape, we approached this challenge through two parallel experiments (reports documented in Supplementary Information). The first was a guided rediscovery task. When prompted to reproduce mechanistic families from the literature, the system successfully recovered the carboxyl, direct/redox, and formate branches, reconstructed local states, and initiated NEB calculations. However, only the local formate entry ($CO_2^* + H^* \rightarrow HCOO^*$) survived stringent filtering, yielding a supported barrier of 0.798 eV. Expected CO-forming routes consistently lost force convergence or drifted from intended local products, despite repeated reruns and endpoint repairs. Subsequent manual inspection revealed that these divergence issues did not stem from invalid chemistry, but from the intrinsic unreliability of universal MLIPs on these surface TS problems. In these transition regions, which are underrepresented in pretraining data, the MACE-driven forces frequently stalled or produced unphysical gradients, causing optimizations to fail.[21, 22]

In parallel, we evaluated the system’s capacity for fully autonomous discovery. To prevent the agent from proactively retrieving known mechanistic steps, we explicitly mandated an unbiased investigation without literature priors. This unconstrained search forced the agent to dynamically redefine its pathway construction logic. Instead of treating relaxed minima as static anchors, the system autonomously introduced connectivity-aware endpoint repairs, local-equivalent pseudo-states, hidden-state extraction from interior images, and short local probes to preserve adsorbate connectivity. This robust protocol expanded the search to 41 relaxed minima, assembling a broad reaction map spanning the $CHO_2^* + H^*$, $CH_2O_2^*$, $CHO^* + HO^*$, $CO^* + H^* + HO^*$, and $CO^* + H_2O^*$ regions. The isolation of several locally supported segments-, including CHO_2 entry and a cleavage-like step of 0.364 eV demonstrates that the agent generated chemically sensible hypotheses of local pathways.

Despite these algorithmic advancements, the macroscopic network ultimately did not achieve strict kinetic closure. As the search entered weakly bound rearrangements and transition regions, the exact same backend limitations emerged: MACE-driven trajectories frequently stalled or produced unphysical paths. Thus, the fundamental bottleneck across both the guided and autonomous routes was identical. Severe MLIP out-of-distribution (OOD) behavior on the Cu(111) surface rendered the accurate geometric resolution of transition states impossible, effectively neutralizing the agent’s pathway logic.

Taken together, these parallel Cu(111) experiments clarify another critical operational boundary of general agentic runtimes, exposing a weakness in their meta-reasoning capabilities. While the agent can successfully map broad topologies and formulate sensible chemical hypotheses, it struggles to adapt when its underlying backend engine becomes intrinsically unreliable. Faced with fundamental MACE OOD failures, CatMaster lacked the meta-awareness to "break the loop". Instead of recognizing the tool breakdown and actively adopting alternative strategies such as suggesting an escalation to higher-fidelity DFT calculations or pivoting to different path-search

paradigms, the system became trapped in execution cycles, repeatedly attempting to repair NEB calculations using the same flawed potential. Consequently, this study diagnoses a dual frontier for autonomous catalysis: achieving strict mechanistic closure requires not only domain-specialized rigorous algorithms and frameworks (such as CARE[23]) to resolve physical underlying issues, but also enhanced self-awareness that enables agents to dynamically break out of failing workflows when their foundational tools collapse.

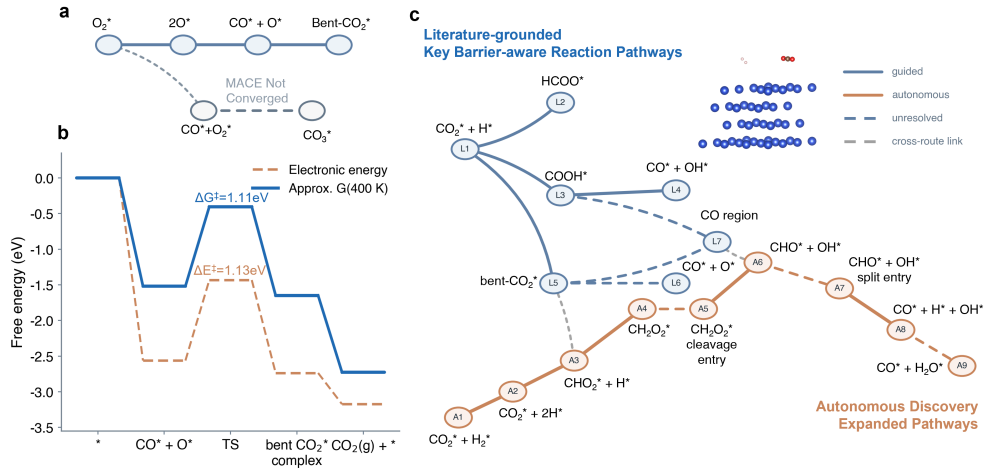


Fig. 4 Reaction-mechanism rediscovery and network exploration by CatMaster under MACE-only evaluation. **a**, Compact Pt(111) mechanism schematic summarizing the accepted terrace route recovered by the agent together with an explored but unconverged molecular O_2 -assisted branch. **b**, Electronic-energy and approximate 400 K free-energy profiles for the accepted direct CO-oxidation route on Pt(111), for which the direct oxidation step remains the kinetic bottleneck. **c**, Cu(111) RWGS network summary combining the literature-guided and autonomous campaigns. Blue edges denote the guided pathway families reconstructed from the literature, orange edges denote the autonomously expanded pathway map, dashed edges indicate unresolved links, and grey dashed links indicate correspondences between the two route representations.

2.5 End-to-End Catalyst Design

To assess the system’s capacity for open-ended discovery, we tasked CatMaster with driving a complete computational catalyst design project. Prompted by a natural-language request to design graphene-supported single-atom catalysts (SACs) for the two-electron CO_2 reduction to CO, the agent was required to define a motif space, execute a surrogate screening, autonomously escalate from an initial probe to a higher-fidelity DFT validation matrix, and synthesize the findings into a formal manuscript. Crucially, this scenario tested the system’s ability to maintain a persistent, closed-loop research thread: when the initially drafted manuscript was flagged as scientifically insufficient by the internal review agent, CatMaster did not terminate. Instead, it

reopened the investigation, designed new computational experiments, repaired failing models, and fundamentally revised the study.

The investigation initiated with a dispersion-inclusive MACE probing of 29 motifs based on a graphene-supported MN_4 template (107 total relaxations) under a vacuum computational hydrogen electrode (CHE) model. At this exploratory stage, the system formulated a phosphorus-centered activation hypothesis: second-shell P substitution consistently lowered the surrogate COOH^* formation energy, emerging as the strongest design lever. Crucially, the system did not halt at this provisional conclusion. To arbitrate these predictions, it autonomously expanded the search space into a 35-motif DFT matrix spanning pristine, single first-shell, and single second-shell variants across bare, COOH^* , and CO^* core states. This evaluation altered the scientific picture. While P-centered motifs retained favorable early-step energetics, they were disqualified as balanced leads due to insurmountable CO-release penalties. Instead, the DFT matrix elevated a refined candidate set comprising B- CoN_4 , NiN_3B , CoN_4 , and N- CoN_4 , explicitly retaining CuN_4 and P- CoN_4 to define the under-activation and overbinding boundaries. CatMaster subsequently drafted a manuscript based on this revised DFT landscape; however, an internal peer-review node rejected the draft as premature, citing insufficient thermodynamic rigor (specifically, the absence of solvation and Gibbs free-energy corrections) and a question of the large model error of the surrogate model.

Rather than terminating the project, CatMaster triggered a closed-loop refinement phase in direct response to this critique. It first repaired alignment in the surrogate model, finetuning it on the accumulated DFT data to dramatically reduce held-out errors (energy MAE improved from 149.75 to 11.72 meV atom⁻¹; force MAE from 0.109 to 0.027 eV Å⁻¹). Then, the system used the upgraded model to rapid triage to nominate additional DFT candidates within the Co/Ni N_3B neighborhood. This targeted follow-up confirmed N- NiN_3B as a competitive novel motif while correctly rejecting B- NiN_3B due to severe hydrogen overbinding. Simultaneously, the agent addressed the physical-chemistry critique by upgrading its evidence hierarchy, transitioning from vacuum descriptors to targeted implicit-solvation validation and explicit adsorbate-frequency calculations. This rigorous thermodynamic layer completed the self-correction cycle: under the solvated CHE ranking, B- CoN_4 , NiN_3B , and N- NiN_3B emerged as the optimal motifs, exhibiting limiting proton-coupled electron transfer costs of 0.015, 0.062, and 0.080 eV, respectively. This progression demonstrates that the agent did not merely update a static ranking, but dynamically revised both its core scientific hypothesis and its standard of evidence prior to project closure.

Ultimately, the project culminated in the autonomous synthesis of these findings into a structured scientific narrative, supported by comprehensive supplementary data and a fully documented internal review history. The ability to distill raw computational executions into defensible claims demonstrates that agentic systems can successfully orchestrate and close an end-to-end research loop. By framing the initial problem, dynamically upgrading its evidence hierarchy, and rigorously responding to physical critique, the system moves well beyond disjointed task execution. Crucially, because CatMaster persists all intermediate decisions, internal review memos, and revised computational artifacts, the hypothesis reversal—from a phosphorus-led

screening artifact to a boron- and nickel-centered thermodynamic ranking—remains completely transparent. In this context, the phosphorus-led branch functions as a critical negative constraint, explicitly bounding the physical limits of the catalyst design space. Consequently, the system achieves more than the mere execution of a complex *in silico* design study; it generates a rigorous, recoverable provenance of how the scientific hypothesis dynamically evolves.

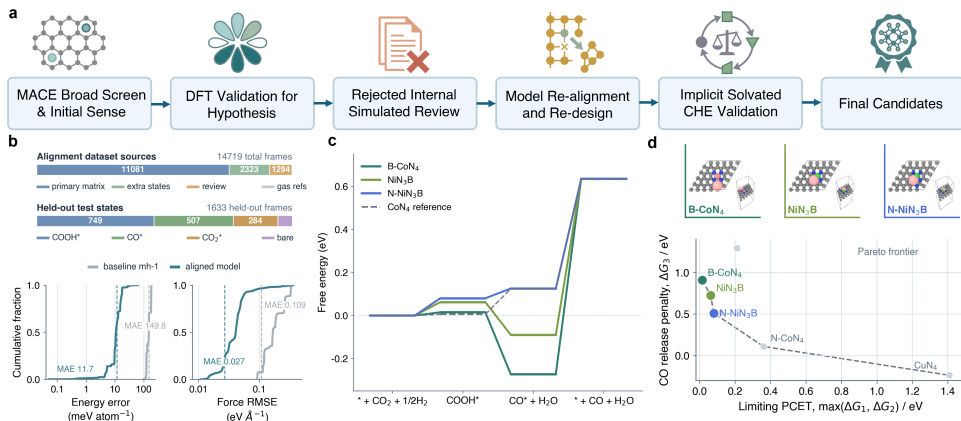


Fig. 5 End-to-end SAC design by CatMaster. **a**, Closed-loop workflow schematic of the SAC campaign, showing how internal review blocked premature closure and forced a reopening toward DFT arbitration, aligned-model repair, focused follow-up, and explicit-CHE closure. **b**, Alignment dataset composition together with held-out cumulative error distributions for the baseline and repaired MACE lanes. **c**, Solvated CHE free-energy profiles for the CoN_4 reference and the three promoted motifs B-CoN_4 , NiN_3B , and $\text{N-NiN}_3\text{B}$. **d**, Final activation-versus-release landscape with the broader Pareto context shown faintly and the three recommended motifs highlighted with representative geometries.

3 Discussion

Taken together, these results demonstrate that CatMaster is highly effective for end-to-end computational research that can be resolved by coupling general reasoning with systematic workflow orchestration. The standard benchmarking scenarios, the MatBench evaluations, and the SAC design study all operate within this domain. Given a well-defined prompt, the system reliably retrieves appropriate artifacts, selects defensible procedures, executes the necessary computations, and synthesizes the outputs into a coherent scientific narrative. Within this operational boundary, modern reasoning backends are sufficiently robust for sustained autonomy, as residual errors are infrequent enough to permit the practical closure of multi-step scenarios.

However, the machine-learning evaluations exposed a critical limit to this autonomy, revealing a distinction between intelligent workflow composition and genuine algorithm invention. Across five of the six MatBench tasks, the agent consistently reconstructed competitive descriptor-based, hybrid, and standard structure-aware pipelines by dynamically routing established tools. The *phonons* scenario, however,

exposed a critical threshold where generalized modelling competence is insufficient. Success on this task strictly requires geometry-rich inductive biases and domain-specific architectural engineering. We observe that within standard iterative loops, the agent naturally gravitates toward composing robust, off-the-shelf representations rather than authoring complex, bespoke neural network architectures from scratch. Our current experiments, however, demonstrate a narrower reality: present agents excel at automating standard materials machine-learning pipelines, but they may not naturally cross into specialized algorithmic invention, in agreement with very recent studies about AutoResearch-like agentic systems.^[24]

The mechanistic case studies expose a second, distinct vulnerability: the system’s susceptibility to meta-reasoning blind spots when facing foundational tool failure. In the Cu(111) RWGS study, the primary bottleneck was not the agent’s symbolic chemical planning, but severe out-of-distribution (OOD) behavior from the underlying MACE potential. As the search entered weakly bound transition regions, the physical backend collapsed, rendering accurate geometric resolution impossible. Faced with these fundamental tool breakdowns, CatMaster lacked the meta-awareness to break the execution loop. Instead of recognizing the potential’s failure and pivoting to alternative strategies, the system became trapped in futile cycles of repairing NEB calculations using the same flawed potential. This highlights a critical frontier: while general agents excel at tool usage, their autonomy may be severely bounded by their inability to dynamically diagnose and escape from backend engine collapses.

These dual limitations fundamentally reframe the current role of human-in-the-loop supervision. Rather than acting as a technical debugger, the human operator increasingly functions as a conceptual architect directing an execution engine that is highly capable but bounded. Throughout this work, the most critical human contribution was not manually intervening in routine computational errors, but providing overarching scientific stewardship: setting resource budgets, injecting creative conceptual leaps, mandating corrective exploration, and deciding whether the accumulated evidence justified project termination. In the machine learning study, human-proposed specialized machine-learning algorithms still excel in hard tasks, and in the Cu(111) RWGS study, explicit human intervention will be required to break the agent out of its MACE-driven execution loops. Human involvement therefore remains essential, not merely as a technical safety net, but as the ultimate arbiter of scientific rigor, dictating when an autonomous investigation must continue and what standard of evidence is required before claims are allowed to stabilize.

The necessity of this high-level expert oversight stems from a fundamental risk in agent-driven research: the divergence between manuscript closure and genuine scientific closure. Because general-purpose systems can seamlessly assemble polished prose and high-quality artifacts around partially resolved data, they risk creating a dangerous illusion of completion. Conversely, when confronted with fundamental tool collapse, their tendency is to elegantly document the failure rather than proactively propose a methodological pivot, creating an equally misleading illusion of a scientific dead end. Moving forward, mitigating this risk will require evolving beyond broad workflow orchestration. General agentic runtimes must be tightly integrated with specialized, domain-rigorous, and validated catalysis frameworks. By anchoring the

agent’s generative capabilities to these expert mechanistic backends, equipping them with the meta-awareness to recognize fundamental tool breakdowns, and establishing strict refusal criteria, future systems may conduct research that never outpaces physical reality.

4 Methods

4.1 Agent Runtime

CatMaster is implemented as a hierarchical, LangChain-based DeepAgent runtime designed around the principle of context isolation.[25, 26] Rather than fragmenting scientific protocols into numerous narrowly scoped micro-agents—which inherently incurs heavy communication overhead and a loss of local detail—CatMaster concentrates orchestration within a small set of highly capable specialists. At the apex of this hierarchy is the *Research Specialist*, the sole orchestration-capable controller responsible for maintaining the active research state. It strategically delegates clear tasks to four primary mid-level coordinators:

(1) the *Experiment Specialist*, which routes computational materials execution, machine learning, molecular quantum-chemistry, and report-generation tasks to dedicated workers; (2) the *Writing Specialist*, which manages author-facing drafting and conservative polishing; (3) the *Literature-review Specialist*, a nested controller that separates broad public-web retrieval from exact scholarly metadata resolution; and (4) the *Peer-review Specialist*, invoked on demand to inspect canonical manuscript PDFs and generate editor-style critiques grounded in reference reports.

By confining execution- or writing-heavy episodes to these dedicated domain specialists and their respective workers, CatMaster drastically reduces delegation depth. Crucially, each execution episode maintains persistence across conversation turns via stable thread identifiers and workspace-level state stores. This design allows the system to continue prior computational work without repeatedly restating the full history of calculations, intermediate files, and earlier decisions in the active model context. Unless otherwise stated, all non-benchmark experiments reported after the model-comparison benchmark were executed with GPT-5.4 using high reasoning effort, selected as the strongest backend from the benchmark evaluation.

4.2 Tool Surface and Skills

The CatMaster tool surface adopts a Unix-style philosophy of composability, heavily tailored for computational catalysis. Instead of deploying monolithic tools that attempt to execute an entire scientific protocol from raw structure to final analysis, tools are defined as typed transformations over concrete scientific artifacts. These artifacts include atomic structures, VASP and ORCA input/output directories,[27–30] datasets, trained models, and analysis parsed-outputs. This atomic design allows agents to dynamically compose preparation, execution, and analysis workflows that were not hard-coded in advance. In practice, the tool surface spans atomistic structure

generation, batch execution, post-processing, literature retrieval, manuscript compilation, and machine-learning operations (e.g., dataset construction and active-learning selection).

Complementing this execution layer are *Skills*—reusable scientific standard operating procedures. Instead of proliferating the agent hierarchy for every recurring protocol, CatMaster stages collections of experiment, machine-learning, quantum-chemistry, and writing skills within the runtime, binding them to specialists as modular guidance. These skills encode domain-specific heuristics (e.g., slab construction, adsorption screening, transition-state routing, and MACE dataset curation[31]) while the actual executable capability remains governed by the active tool binding.

Currently, the active codebase stages 36 explicit skills and 70 registered tools, with only a role-compatible subset exposed to any given specialist. Detailed role, tool, and skill inventories are provided in the Supplementary Information.

4.3 Computational Scenario Evaluation

Benchmark evaluations were launched through the same CatMaster experiment runtime used elsewhere in this study, with each run executed in an isolated workspace and initiated from a natural-language scenario request. We defined four benchmark scenarios that probe complementary aspects of computational catalysis practice: structure retrieval and relaxation-input preparation, adsorption-energy screening, MACE transition-state analysis, and density-of-states interpretation. All models participating in the benchmark used high reasoning effort. For each model backend we ran three independent repeats per scenario, yielding 12 benchmark runs per model. Each candidate model had to complete the full chain from request to persisted scientific deliverables and a final report, rather than merely edit one artifact or answer a narrow question.

Scoring was performed using LLM-as-a-judge and a human-review check based on filesystem evidence using scenario-specific rubrics. During scoring, model backend identities were blinded and exposed only as anonymized labels (*ModelA–ModelD*) to reduce potential model-name bias. Maximum scores and hard-cap rules encoded in the benchmark judge. The judge inspected only persisted outputs under each run workspace, rewarding equivalent evidence even when local file layouts differed. The human-reviewed scores reported in Fig. 2 and discussed in the Results are the final benchmark values used in this manuscript; full prompts, rubric details, manual revisions and repeat-level score tables are provided in the Supplementary Information.

4.4 MatBench Modeling Evaluation

General-purpose modelling evaluations were carried out on six MatBench scenarios chosen to span task type, input primitive, and data scale: *steels*, *expt_gap*, *is_glass*, *jdft2d*, *mp_is_metal*, and *phonons*. [20] Each scenario was launched from a common natural-language prompt template that asked CatMaster to complete feature engineering, model development, hyperparameter search, official benchmark evaluation, and report writing inside the local workspace. The prompt explicitly permitted up to five internal optimization rounds while preserving official MatBench data-splitting

rules. For regression scenarios CatMaster used shuffled five-fold ‘KFold’ splits with ‘random_state=18012019’; for classification scenarios it used shuffled five-fold ‘StratifiedKFold’ splits with the same seed. In all cases outer test folds were reserved for final reporting only, and feature, model, and hyperparameter selection were performed only within each outer-training partition.

For a modelling episode to count as complete, CatMaster had to produce reproducible scripts, saved models and held-out predictions, and a detailed markdown report in addition to the final metric summary. No manual code editing was inserted between the initial request and the official evaluation of a given scenario. The only deliberate exception was *phonons*, where an explicit second self-improvement episode was authorized after the first locked run underperformed. Performance was compared against the method summaries on MatBench result leaderboard accessed in March, 2026. The common prompt template, scenario matrix, recovered workflow summaries, and full performance table are provided in the Supplementary Information.

4.5 End-to-End SAC Design Workflow

The SAC-design case began from a natural-language request to investigate graphene-supported MN_4 catalysts for two-electron CO_2 reduction to CO by varying the metal center together with first-shell and second-shell dopants, while remaining within a limiting exploratory budget and ending in a full report. CatMaster started from a provided graphene/ FeN_4 template structure and was required to decide its own evidence hierarchy. In the first phase it performed broad 29-motif exploration with dispersion-inclusive MACE screening, formed an internal shortlist hypothesis, and then escalated to a complete 35-motif DFT primary matrix for validation. After the first manuscript package was judged insufficient for submission by *Peer-review Specialist*, a second phase was explicitly reopened with additional computational resources and required CatMaster to continue.

Acknowledgements. This work was supported by the National Key R&D Program of China (No. 2022ZD0117501), the Scientific Research Innovation Capability Support Project for Young Faculty (ZYGXQNJSKYCXNLZCXM-E7), the Tsinghua University Initiative Scientific Research Program, and the Carbon Neutrality and Energy System Transformation (CNEST) Program led by Tsinghua University.

Data availability. The relevant original workspaces required to reproduce this study is deposited on figshare with DOI: 10.6084/m9.figshare.31891201

Code availability. The source code required to reproduce this work is available at <https://github.com/q734738781/CatMaster>.

Competing interests. The authors declare no competing interests.

References

- [1] Boiko, D. A., MacKnight, R., Kline, B. & Gomes, G. Autonomous chemical research with large language models. *Nature* **624**, 570–578 (2023).
- [2] Lu, C. *et al.* Towards end-to-end automation of ai research. *Nature* **651**, 914–919 (2026).
- [3] Gottweis, J. *et al.* Towards an ai co-scientist. *arXiv preprint arXiv:2502.18864* (2025).
- [4] Li, S. Density functional theory for catalyst development and mechanistic insights. *Nature Reviews Clean Technology* **1**, 602–602 (2025).
- [5] Hjorth Larsen, A. *et al.* The atomic simulation environment—a python library for working with atoms. *Journal of Physics: Condensed Matter* **29**, 273002 (2017).
- [6] Ong, S. P. *et al.* Python materials genomics (pymatgen): A robust, open-source python library for materials analysis. *Computational Materials Science* **68**, 314–319 (2013).
- [7] Jain, A. *et al.* Fireworks: a dynamic workflow system designed for high-throughput applications. *Concurrency and Computation: Practice and Experience* **27**, 5037–5059 (2015).
- [8] Pizzi, G., Cepellotti, A., Sabatini, R., Marzari, N. & Kozinsky, B. Aiida: automated interactive infrastructure and database for computational science. *Computational Materials Science* **111**, 218–230 (2016).
- [9] Jain, A. *et al.* Commentary: The materials project: A materials genome approach to accelerating materials innovation. *APL materials* **1** (2013).
- [10] Zou, Y. *et al.* El agente: An autonomous agent for quantum chemistry. *Matter* **8** (2025).
- [11] Pérez-Sánchez, J. B. *et al.* El agente quntur: A research collaborator agent for quantum chemistry. *arXiv preprint arXiv:2602.04850* (2026).
- [12] Kumar, S. G. H. *et al.* El agente s\’olido: A new age (nt) for solid state simulations. *arXiv preprint arXiv:2602.17886* (2026).
- [13] Ding, K. *et al.* Scitoolagent: a knowledge-graph-driven scientific agent for multitool integration. *Nature Computational Science* **5**, 962–972 (2025).
- [14] Pham, T. D., Tanikanti, A. & Keçeli, M. Chemgraph as an agentic framework for computational chemistry workflows. *Communications Chemistry* (2026).

- [15] Wang, Z. *et al.* Dreams: Density functional theory based research engine for agentic materials simulation. *arXiv preprint arXiv:2507.14267* (2025).
- [16] Xia, Z. *et al.* An agentic framework for autonomous materials computation. *arXiv preprint arXiv:2512.19458* (2025).
- [17] Chandrasekhar, A., Ock, J. & Farimani, A. B. Catalyst-agent: Autonomous heterogeneous catalyst screening and optimization with an llm agent. *arXiv preprint arXiv:2603.01311* (2026).
- [18] Mok, D. H., Back, S., Fung, V. & Hu, G. Reasoning-driven design of single atom catalysts via a multi-agent large language model framework. *arXiv preprint arXiv:2602.21533* (2026).
- [19] Hu, Z. *et al.* Tritondft: Automating dft with a multi-agent framework. *arXiv preprint arXiv:2603.03372* (2026).
- [20] Dunn, A., Wang, Q., Ganose, A., Dopp, D. & Jain, A. Benchmarking materials property prediction methods: the matbench test set and automatminer reference algorithm. *npj Computational Materials* **6**, 138 (2020).
- [21] Focassio, B., M. Freitas, L. P. & Schleder, G. R. Performance assessment of universal machine learning interatomic potentials: Challenges and directions for materials’ surfaces. *ACS Applied Materials & Interfaces* **17**, 13111–13121 (2024).
- [22] Jacobs, R. *et al.* A practical guide to machine learning interatomic potentials—status and future. *Current Opinion in Solid State and Materials Science* **35**, 101214 (2025).
- [23] Morandi, S. *et al.* An end-to-end framework for reactivity in heterogeneous catalysis. *Nature Chemical Engineering* 1–12 (2026).
- [24] Du, G., Ahlwat, A., Liu, X. & Wu, J. A framework for assessing ai agent decisions and outcomes in automl pipelines (2026). URL <https://arxiv.org/abs/2602.22442>. *arXiv:2602.22442*.
- [25] Mavroudis, V. Langchain (2024).
- [26] LangChain. Deep agents overview (2026). URL <https://docs.langchain.com/oss/python/deepagents/overview>. Accessed March 27, 2026.
- [27] Kresse, G. & Furthmüller, J. Efficient iterative schemes for ab initio total-energy calculations using a plane-wave basis set. *Physical review B* **54**, 11169 (1996).
- [28] Kresse, G. & Joubert, D. From ultrasoft pseudopotentials to the projector augmented-wave method. *Physical review b* **59**, 1758 (1999).

- [29] Neese, F., Wennmohs, F., Becker, U. & Riplinger, C. The orca quantum chemistry program package. *The Journal of chemical physics* **152** (2020).
- [30] Neese, F. Software update: the orca program system—version 6.0. *Wiley Interdisciplinary Reviews: Computational Molecular Science* **15**, e70019 (2025).
- [31] Batatia, I., Kovacs, D. P., Simm, G., Ortner, C. & Csányi, G. Mace: Higher order equivariant message passing neural networks for fast and accurate force fields. *Advances in neural information processing systems* **35**, 11423–11436 (2022).

Supporting Information for Autonomous Computational Catalysis Research via Agentic Systems

Honghao Chen¹, Jiangjie Qiu¹, Yi Shen Tew¹, Xiaonan Wang^{1,*}

¹Beijing Key Laboratory of Artificial Intelligence for Advanced Chemical Engineering Materials,
Department of Chemical Engineering, Tsinghua University, Beijing, China

*Correspondence: wangxiaonan@tsinghua.edu.cn

Contents

1	Implementation Details for CatMaster	3
1.1	Agent Runtime Details	3
1.1.1	Context Isolation and Hierarchical Delegation	3
1.1.2	Persistent State and Reporting Contract	3
1.1.3	Infrastructure Schematic	4
1.1.4	Prompt Contracts for Coordination Specialists	7
1.1.5	Prompt Contracts for Execution and Writing Workers	8
1.1.6	Prompt Contracts for Literature and Metadata Agents	10
1.1.7	Shared Prompt Policies	11
1.2	Tool Surface and Skill Definitions	11
1.2.1	Primitive Design Principles	11
1.2.2	Tool Taxonomy and Access Policies	12
1.2.3	Detailed Primitive Tool Inventory	14
1.2.4	Skill Layer and Role-Specific Exposure	17
2	Benchmark Construction and Evaluation Details	19
2.1	Benchmark Tasks and Operational Prompts	19
2.2	Filesystem-Based Judging and Manual Review	20
2.3	Human-Reviewed Benchmark Results	23
3	General-Purpose Machine Learning Benchmark Details	25
3.1	Common MatBench Prompt and Scenario Matrix	25
3.2	Typical CatMaster Workflow Patterns	26
3.3	Full Performance Summary	27
4	Cu(111) RWGS Case Notes	28
4.1	Two Complementary Cu(111) Routes	28
4.2	Interpretive Scope	28
5	End-to-End SAC Design Project Details	29
5.1	Initial and Continuation Prompts	29
5.2	Project Brief and Closure Trajectory	29
5.3	Final Catalyst-Facing Conclusions and Package Status	30

6	Original Manuscript Drafts Produced by CatMaster	32
6.1	Pt(111) CO-Oxidation Short Paper	32
6.2	Cu(111) RWGS Literature-Guided Short Paper	44
6.3	Cu(111) RWGS Autonomous-Exploration Short Paper	60
6.4	SAC Main Manuscript	79
6.5	SAC Supporting Information	97
	References	110

1 Implementation Details for CatMaster

1.1 Agent Runtime Details

1.1.1 Context Isolation and Hierarchical Delegation

CatMaster uses a DeepAgent-native specialist runtime organized around minimal hierarchy and context isolation.[1, 2] Rather than decomposing every scientific procedure into many communicating micro-agents, the runtime keeps coordination concentrated in a small set of specialists and reserves delegation for bounded subtasks that naturally benefit from local autonomy. This design choice was motivated by the observation that many computational-catalysis operations are not independent atomic actions but short, interdependent episodes. A geometry relaxation, for example, often requires structure preparation, execution, convergence inspection, and local interpretation within one coherent context window. Excessive agent subdivision increases handoff cost, duplicates intermediate summaries, and makes it easier for later agents to lose the operational detail needed to complete the protocol robustly. CatMaster therefore treats agent multiplication as a last resort and introduces specialization mainly when a subtask has a distinct artifact focus or requires a substantially different scientific operating procedure.

The runtime exposes three top-level specialist entrypoints for research coordination, experiment execution, and writing, with an additional peer-review specialist available when formal manuscript review is explicitly requested. The research specialist is the only orchestration-capable controller. It coordinates the scientific campaign, decides when bounded experiments are justified, and delegates only to the experiment specialist, the writing specialist, the literature-review specialist, and the peer-review specialist. The experiment specialist handles bounded computational execution and does not orchestrate other top-level specialists. Instead, it routes materials-centred periodic workflows to a materials worker, dataset and model lifecycle tasks to an ML worker, molecule- or cluster-centred quantum-chemistry work to an ORCA/xTB worker, narrow external grounding to a lightweight literature agent, and execution-facing summaries to a report-writing worker. The writing specialist is similarly constrained: it coordinates author-facing outputs, delegates substantive drafting to a writing worker, uses a dedicated polishing worker only for conservative prose refinement, and calls a lightweight literature agent only when tightly bounded background supplementation is needed for a current manuscript section.

The literature subsystem is itself hierarchical. For broad related-work analysis and citation-oriented review, the research specialist calls a literature-review specialist that internally separates two functions: a broad public-web literature agent for orientation and synthesis, and a metadata agent for exact paper resolution, including DOI, venue, year, authorship and recommendation expansion. This separation avoids conflating exploratory review with citation-grade record disambiguation. In contrast, the experiment and writing specialists receive only a lightweight literature agent intended for narrow contextual checks, preventing those threads from expanding into open-ended review campaigns while execution or drafting is underway.

1.1.2 Persistent State and Reporting Contract

CatMaster persists ongoing work through a stable DeepAgent thread identifier together with workspace-level state stores. Short-term multi-turn continuity is carried by the thread itself, whereas durable state is written to a run snapshot file and SQLite-backed checkpoint and memory stores. The research specialist additionally maintains a lightweight research kernel containing the active scientific question, a small set of current hypotheses, compact run cards, frontier items, and a provisional conclusion draft. This kernel is intentionally small and decision-oriented: it is used to keep the active campaign coherent without reifying every intermediate step into a heavy orchestration schema. Final specialist outputs likewise follow a compact contract centered on summary, facts, and artifact paths, which makes delegation outputs easy to reuse while limiting prompt inflation.

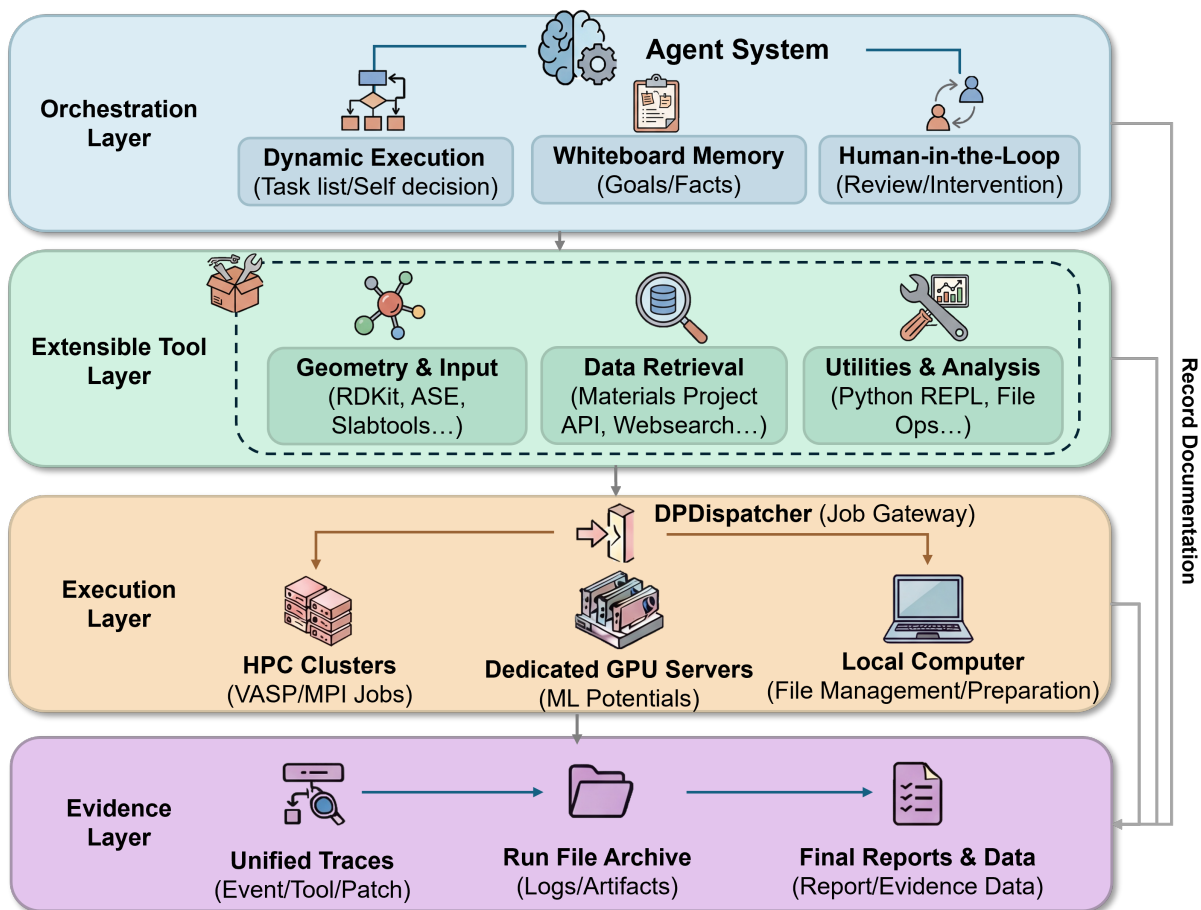


Figure 1: Infrastructure schema of CatMaster beneath the specialist hierarchy. The schematic emphasizes the four lower layers of the runtime: agent-facing control, primitive tool interfaces, executable workspaces and jobs, and persisted evidence artifacts that feed back into analysis and reporting.

Two further implementation choices are important for reproducibility. First, worker threads are encouraged to materialize heavy deterministic logic as reusable scripts inside the workspace when a task becomes high-throughput, batch-oriented, or likely to be rerun, rather than burying the full workflow inside one ephemeral shell call. Second, multimodal outputs are treated as persisted artifacts referenced by path, with only concise textual summaries retained in long-lived history, which improves cross-turn stability for manuscript figures, rendered structures, and reviewed PDFs. Together, these policies allow CatMaster to preserve local depth and operational continuity without coupling the system to a brittle, over-engineered orchestration layer.

1.1.3 Infrastructure Schematic

Figure S1 summarizes the lower infrastructure stack that sits beneath the specialist hierarchy. Whereas the main manuscript figure is intended to emphasize campaign-level coordination, the schematic shown here focuses on the interface between agents, tools, executable work, and evidence. This distinction is important because CatMaster does not operate as a purely conversational orchestration layer: agent decisions are translated into typed tool invocations, tools materialize concrete execution directories and jobs, and completed runs return persisted evidence artifacts that can be inspected, summarized, cited, and re-used by downstream specialists.

Table 1: Hierarchical organization of the CatMaster runtime.

Runtime node	Hierarchical relation	Responsibility
Research specialist	Primary campaign coordinator; delegates to experiment, writing, literature-review, and optional peer-review specialists	The only orchestration-capable specialist. It maintains the lightweight research kernel, decides when bounded experiment work is justified, and determines when author-facing writing or external-style peer review should begin.
Experiment specialist	Receives bounded execution tasks from the research layer or from a direct execution request; delegates to materials, ML, molecular-QC, lightweight literature, and report workers	Bounded execution coordinator. It routes work by the current artifact type and prevents a single worker from swallowing an entire campaign. It is explicitly not allowed to orchestrate other top-level specialists.
Materials worker	Execution worker under the experiment specialist; no further delegation	Periodic and materials-facing execution worker for structure editing, slab and adsorption workflows, VASP preparation and execution, MACE-based surrogate screening, and materials-side post-analysis.
ML worker	Execution worker under the experiment specialist; no further delegation	Dataset and model lifecycle worker for dataset construction from completed runs, MACE training, held-out evaluation, and active-learning candidate selection. The workflow may fall back to reusable local scripts when no dedicated managed tool covers the required code path.
Molecular-QC worker	Execution worker under the experiment specialist; no further delegation	Molecular and cluster quantum-chemistry worker for conformer search, xTB screening, ORCA preparation and execution, and post-analysis for optimization, thermochemistry, transition-state, IRC, and related workflows.
Lightweight literature worker (experiment)	Lightweight worker under the experiment specialist; no further delegation	Narrow external-grounding worker for quick benchmark checks, methods lookups, or limited contextual grounding during execution.
Report worker	Writing worker under the experiment specialist; no further delegation	Report-writing worker for experiment-facing outputs, including validation summaries, QC notes, execution memos, and other bounded reports drawn only from existing evidence. It is not a manuscript-writing lane.
Writing specialist	Receives author-facing drafting requests from the research layer or from a direct writing request; delegates to writing, polishing, and lightweight literature workers	Author-facing writing coordinator. It decides section scope, evidence selection, and revision strategy, and delegates substantive drafting to workers rather than writing long sections directly in the parent thread.
Writing worker	Writing worker under the writing specialist; no further delegation	Section drafting and integration worker. It handles one bounded section or organizational task at a time, can prepare figures or tables from existing evidence, organizes what belongs in the main text versus supporting content, and is responsible for direct L ^A T _E X compilation and repair.
Writing polisher	Writing worker under the writing specialist; no further delegation	Conservative local prose-polishing worker. It improves flow and journal-style phrasing without changing scientific scope, claim strength, evidence selection, figure order, or manuscript structure.

Runtime node	Hierarchical relation	Responsibility
Lightweight literature worker (writing)	Lightweight worker under the writing specialist; no further delegation	Narrow external-grounding worker for tightly bounded manuscript-context lookups, such as missing background phrasing or a narrow benchmark check needed in the current draft.
Literature-review specialist	Literature-review specialist under the research layer; delegates to a broad-review worker and a metadata worker	Literature-review specialist for broad related-work analysis in the research thread. It deliberately separates broad review from exact citation-grade metadata resolution.
Broad-review worker	Broad-review worker under the literature-review specialist; no further delegation	Public-web literature-review worker for orientation, public-source synthesis, and representative evidence gathering.
Metadata worker	Metadata worker under the literature-review specialist; no further delegation	Exact scholarly-metadata worker for DOI, venue, year, author, and recommendation expansion using scholarly metadata services.
Peer-review specialist	Optional review-mode specialist invoked from the research layer or by direct review request; no further delegation	Dedicated review-mode specialist that acts like an editor over a canonical manuscript PDF and returns an editor decision together with reviewer comments.

Table 2: Role-specific executable surfaces and skill bindings.

Runtime node	Bound executable surface	Tool count	Skill binding and policy notes
Research specialist	Research tool surface	4	Receives two filtered skill views, one aligned with experiment conventions and one aligned with writing conventions. These let the top-level coordinator reason about both domains without inheriting the full downstream execution surface.
Experiment specialist	Union of materials, ML, and molecular-QC execution tools	56	Receives the filtered experiment-specialist skill view. Its prompt enforces artifact-based routing and requires each worker handoff to remain a single bounded execution episode.
Materials worker	Materials and periodic-execution surface	39	Receives a filtered experiment skill view and is the only worker equipped with a model-based tool selector. The selector caps the visible domain tools per step while preserving file and execution primitives.
ML worker	ML dataset, training, and evaluation surface	4	Receives the machine-learning skill view. The prompt prioritizes managed MACE tools when applicable but explicitly permits local reusable scripts when the task falls outside dedicated tool coverage.
Molecular-QC worker	Molecular-QC surface	17	Receives the quantum-chemistry skill view for conformer, xTB, ORCA, TS, IRC, and NMR-style molecular workflows.
Lightweight literature worker (experiment)	Lightweight public-web search surface	1	No heavy skill family is attached. This worker is intentionally narrow and is used only for quick contextual checks during execution.
Report worker	Writing and report surface	5	Receives a filtered writing skill view. The prompt explicitly forbids converting execution reports into manuscript-style narratives.

Runtime node	Bound executable surface	Tool count	Skill binding and policy notes
Writing specialist	Writing and review surface	4	Receives the filtered writing-specialist skill view. It owns author-facing writing coordination and may call the lightweight literature worker only for tightly bounded supplementation.
Writing worker	Writing-production surface	5	Receives a filtered writing-production view. It is responsible for section drafting, evidence integration, figure planning from existing artifacts, and direct L ^A T _E X compilation.
Writing polisher	Writing-production surface	5	Receives a filtered writing-production view. It is restricted to local prose polish and must not change the scientific argument.
Lightweight literature worker (writing)	Lightweight public-web search surface	1	No heavy skill family is attached. It is used only for narrow writing-support lookups and must not expand into broad review.
Literature-review specialist	No direct CatMaster domain tools beyond its nested workers	0	It does not act as a direct execution worker. Instead it orchestrates two nested workers, one for broad review and one for exact scholarly metadata.
Broad-review worker	Broad public-web review surface	3	No large skill family is attached. This worker supports review synthesis, page reading, and representative evidence gathering.
Metadata worker	Scholarly-metadata surface	5	No large skill family is attached. A compaction middleware is additionally bound here to manage dense citation-resolution threads.
Peer-review specialist	External-review request surface	1	Receives a filtered writing-side review view and is intentionally isolated from experiment and manuscript-drafting tools.

1.1.4 Prompt Contracts for Coordination Specialists

The active prompt layer is deliberately explicit. Rather than relying on generic tool-use prompts, each coordination specialist is given a narrow operating contract that fixes its delegation rights, the kinds of artifacts it may own, and the conditions under which it should stop, continue, or hand off work. These prompt contracts are central to the CatMaster design because they encode epistemic boundaries in addition to routing behavior.

Table 3: Prompt contracts for coordination specialists.

Role	Core mandate	Prompt constraints and role-specific instructions
Research specialist	Coordinate the scientific campaign and decide when execution, writing, literature review, or peer review should occur	This role is the only orchestration-capable controller. Its prompt restricts delegation to experiment, writing, literature-review, and optional peer-review specialists; requires broad literature review to pass through the literature-review specialist; forbids large direct execution when delegation is more appropriate; and treats returned peer-review text as an authoritative revision brief rather than something to be compressed away. It also requires compact author packets for paper-facing handoffs and compact report packets for execution-facing handoffs.
Experiment specialist	Coordinate bounded computational execution while preserving artifact focus and local context	Its prompt routes work by the current artifact type, requires each worker handoff to cover one bounded execution episode with one primary goal and one completion criterion, and forbids handing an entire high-throughput campaign to a single worker. When tool coverage is incomplete, it must continue through focused local implementation and reusable scripts rather than stopping at the tool boundary. Narrow external checks are allowed for implementation details, but the prompt explicitly forbids turning those checks into broad literature campaigns.
Writing specialist	Coordinate author-facing drafting and revision from existing evidence only	Its prompt forbids new experiments and broad literature review from the writing thread, pushes substantive drafting to the writing worker, and reserves the main thread for planning, evidence selection, revision strategy, and final reconciliation. It additionally requires journal-style titles, figure-aware manuscript assembly, deliberate organization of main text versus supporting content, direct manuscript-PDF review before finalization, and one more bounded revision pass after review.
Peer-review specialist	Act as an editor over one manuscript PDF and return review-grounded publication guidance	Its prompt instructs it to identify one canonical manuscript PDF, call the review-request tool exactly once per review episode, and then synthesize an editor decision and editor comment while preserving raw reviewer comments. It is explicitly forbidden from running experiments, rewriting the manuscript, or taking over research planning.

1.1.5 Prompt Contracts for Execution and Writing Workers

Worker prompts are more operational and artifact-bound than the coordination prompts. Each worker is instructed to stay within one narrow scientific lane, return concise evidence and artifact paths, and avoid silently expanding scope. In this sense, worker prompts implement

the context-isolation principle directly: they are intended to preserve local coherence inside a bounded subtask, not to become miniature research directors.

Table 4: Prompt contracts for execution and writing workers.

Role	Scientific lane	Prompt constraints and role-specific instructions
Materials worker	Periodic materials and catalysis execution	Its prompt covers structure editing, slab and adsorption workflows, VASP preparation and execution, MACE-based surrogate screening, and materials-side post-analysis. It prefers registered managed tools when available, may fall back to focused local implementation when needed, is allowed narrow implementation-oriented web checks, and is instructed to materialize heavy deterministic logic as reusable scripts. The prompt also explicitly prepares handoffs to the ML worker when the resulting artifact becomes a dataset or model task.
ML worker	Dataset and model lifecycle work	Its prompt prioritizes dataset construction, MACE training, held-out evaluation, and active-learning selection. Managed training and evaluation tools are preferred when they fit the task, but the prompt explicitly permits reusable local scripts for unsupported paths. It also requires handoff back to the materials worker when new structures, new reference calculations, or materials-side post-analysis become necessary.
Molecular-QC worker	Molecular and cluster quantum chemistry	Its prompt treats xTB and CREST as the fast exploration layer and ORCA as the higher-fidelity molecular quantum layer unless the task explicitly says otherwise. It requires structure creation or verification before launch, keeps molecular tasks on the molecular lane rather than translating them into periodic workflows, and allows focused local scripting for unsupported bounded tasks.
Report worker	Experiment-facing reporting	Its prompt is explicitly separated from the manuscript lane. It writes validation summaries, QC notes, and execution memos from existing evidence only, preserves failed attempts and QC caveats when they matter, and forbids restarting calculations merely to make the report appear more complete.
Writing worker	Section drafting and manuscript integration	Its prompt handles one section or one organizational task at a time, assumes that the parent already reduced the task to a compact author packet, and requires deliberate organization of main text versus supporting content. It is allowed to add evidence-carrying figures or tables from existing artifacts, but must compile L ^A T _E X itself and repair compile-facing issues before returning.

Role	Scientific lane	Prompt constraints and role-specific instructions
Writing polisher	Conservative local revision	Its prompt is intentionally narrow: it may improve flow, readability, transitions, and journal phrasing, but it may not alter claim strength, evidence selection, structure, references, or scientific scope. If a needed change is argumentative or evidentiary rather than local prose polish, it must report that rather than rewrite around it.

1.1.6 Prompt Contracts for Literature and Metadata Agents

The literature prompts are split by epistemic function rather than by subject area. CatMaster separates broad review, citation-grade metadata resolution, and lightweight contextual checking because those activities reward different search behavior and different stopping rules.

Table 5: Prompt contracts for literature and metadata agents.

Role	Function	Prompt constraints and role-specific instructions
Literature-review specialist	Orchestrate broad review plus exact citation resolution	Its prompt does not perform direct scientific execution. Instead it delegates public-web orientation and synthesis to a broad-review worker, delegates exact record disambiguation to a metadata worker, and uses one or both depending on whether a review needs orientation, metadata, or both.
Broad-review worker	Public-web literature orientation and synthesis	Its prompt instructs it to gather representative, decision-relevant sources, separate retrieved facts from inference, avoid pretending to resolve exact citation metadata, and save reusable literature notes only when that extra artifact is justified.
Metadata worker	Exact scholarly record resolution	Its prompt allows only scholarly metadata tools and emphasizes precision over breadth. When ambiguity remains, it must narrow candidates and state uncertainty rather than guess. The returned structure is explicitly metadata-centered rather than narrative.
Lightweight literature worker for experiment	Narrow execution-side contextual grounding	Its prompt uses only the lightweight web-search tool for benchmark conventions, methods checks, safety notes, or broader public-web answers that matter for the current execution context. It is not allowed to expand into broad literature review.
Lightweight literature worker for writing	Narrow manuscript-context grounding	Its prompt supports only tightly bounded writing-assistance queries, such as missing introduction background or a narrow citation-support check. If the task really requires broad review or citation-grade disambiguation, it must say so rather than continue to expand.

1.1.7 Shared Prompt Policies

Several prompt fragments are shared across roles because they encode platform-level scientific discipline rather than lane-specific behavior. These shared policies are important for understanding why CatMaster uses relatively few specialists while still maintaining consistent manuscript and artifact quality.

Table 6: Shared prompt policies reused across multiple roles.

Shared policy	Function in the runtime
Author packet policy	Requires paper-facing handoffs to be reduced to a compact author packet containing thesis, novelty, core claims, evidence references, main-text priorities, supporting-only material, and target outputs, instead of forwarding raw run history.
Report packet policy	Requires experiment-facing reporting handoffs to be reduced to a compact packet focused on objective, executed scope, key methods, key results, failures or QC, and target outputs.
Peer-review-ready manuscript policy	Forces writing-side roles to formulate the strongest evidence-supported claim directly and to avoid self-cancelling hedging or reflexive underclaiming.
Journal-manuscript discipline	Prevents journal-facing writing from exposing internal workflow provenance such as prompts, agents, tools, files, or run-state details.
Multimodal artifact discipline	Requires images, PDFs, and other non-text outputs to be preserved as workspace artifacts with short textual summaries rather than replayed indefinitely as raw multimodal history.
Workspace-path discipline	Enforces reusable, topic-centered workspace organization and pushes high-throughput or deterministic logic toward explicit scripts rather than one-off shell fragments.
Soft reporting contract	Normalizes closeout into compact summaries, facts, and file paths so that downstream specialists can reuse results without inheriting unnecessarily large contexts.

1.2 Tool Surface and Skill Definitions

1.2.1 Primitive Design Principles

The CatMaster tool surface was designed under a primitive, compositional philosophy. In this framework, tools are defined by the type of scientific artifact they transform rather than by a large scientific task that they claim to solve end to end. The runtime therefore operates over a small typed artifact vocabulary:

S = single structure, SB = structure batch, C = single calculation-input directory,
 CB = input batch, R = single run-result directory, RB = result batch,
 A = analysis artifact, D = dataset, M = model.

Tool classes are then defined as controlled transformations over these artifact types rather than over high-level scientific intentions. In the intended abstraction, modelling tools satisfy

$$S / SB \rightarrow S / SB,$$

preparation tools satisfy

$$S / SB \rightarrow C / CB,$$

execution tools satisfy

$$C / CB \rightarrow R / RB,$$

analysis tools satisfy

$$R / RB \rightarrow A,$$

with optional export of S or SB when a completed run must yield reusable relaxed structures, and machine-learning tools satisfy

$$RB / D \rightarrow D / M / A.$$

This path-typed abstraction was adopted to keep tools scientifically legible, composable, and maintainable. Tools that collapse several of these layers into one interface are treated as exceptions rather than the core abstraction, because they tend to blur failure boundaries, make reuse harder, and reduce the agent’s ability to recombine scientific procedures in new contexts.

This design explicitly rejects oversized bundle tools that try to perform an entire protocol in one step. For example, a single tool that starts from a bulk structure, generates all surfaces, executes all calculations, computes surface energies, and returns a final ranking may appear convenient, but it hides failure boundaries, impedes recombination, and makes the tool surface difficult to maintain as scientific practice evolves. In CatMaster, such workflows are instead assembled from narrower primitives, such as structure retrieval, slab construction, atomic constraints, adsorption-site enumeration, adsorbate placement, input preparation, batch execution, and post-analysis. The resulting surface is more verbose at the tool level but substantially more flexible at the system level, because agents can recombine the same primitives to address new mechanistic or design questions without requiring a new dedicated tool for each variant of the task.

1.2.2 Tool Taxonomy and Access Policies

The active registered tool surface spans several domains. For atomistic and geometry operations, CatMaster includes tools for molecular structure generation from SMILES, conformer enumeration and filtering, slab construction, supercell generation, unique-site enumeration, defect or dopant construction, adsorption-site enumeration, adsorbate placement, reaction-image generation for nudged elastic band calculations, strain generation, phonon displacement preparation, and structure rendering or image-based inspection. For electronic-structure preparation and execution, the surface includes VASP input preparation, band-structure preparation, VASP NEB and dimer setup, batch VASP execution, ORCA preparation and execution, xTB batch runs, CREST conformer search, and MACE-based relaxation, single-point, and NEB screening. Analysis tools convert completed runs into numerical summaries or manuscript-ready artifacts through utilities for VASP, ORCA and xTB analysis, trajectory inspection, thermochemical corrections, text compilation, PDF review, figure generation, and prose polishing. Machine-learning tools support dataset construction from completed runs, MACE training and evaluation, and active-learning candidate selection. Additional tools support retrieval from external materials databases and exact scholarly metadata resolution.

The tool surface is not presented uniformly to every agent. Each specialist and worker receives a restricted allowlist tailored to its responsibilities. Tool exceptions are surfaced back to the model as non-fatal, model-readable errors, allowing specialists to diagnose or reroute failed steps rather than collapsing the entire run.

Table S1 groups the regular executable surface by functional family. This table is intended as an organizational overview rather than as a substitute for the per-tool descriptions below. Its main purpose is to show that the apparent breadth of CatMaster arises from a small number of recurring transformation classes applied across different scientific artifacts.

Table 7: Non-agentic registered CatMaster tool inventory grouped by functional family (63 tools total).

Tool family	Primitive role in the runtime	Registered tools
Materials and atomistic modelling, execution, and analysis	Structure generation and editing, periodic input preparation, periodic execution, screening, structure rendering, and post-analysis for materials and catalysis workflows	<code>mp_search_materials</code> , <code>mp_download_structure</code> , <code>create_molecule_from_smiles</code> , <code>build_slab</code> , <code>fix_atoms_by_layers</code> , <code>fix_atoms_by_height</code> , <code>fix_atoms_by_indices</code> , <code>supercell</code> , <code>enumerate_unique_sites</code> , <code>create_vacancy</code> , <code>substitute_species</code> , <code>insert_interstitial_at_coords</code> , <code>enumerate_adsorption_sites</code> , <code>place_adsorbate</code> , <code>generate_batch_adsorption_structures</code> , <code>make_neb_geometry</code> , <code>generate_strained_structures</code> , <code>generate_kpath</code> , <code>generate_phonon_displacements</code> , <code>vasp_prepare</code> , <code>vasp_band_prepare</code> , <code>vasp_neb_prepare</code> , <code>vasp_dimer_prepare</code> , <code>make_dimer_mode_from_neb</code> , <code>make_dimer_mode_from_mace</code> , <code>mace_analyze_frequencies</code> , <code>mace_relax_batch</code> , <code>mace_sp_batch</code> , <code>mace_neb_batch</code> , <code>vasp_execute_batch</code> , <code>analyze_vasp_results</code> , <code>analyze_vasp_neb_results</code> , <code>analyze_trajectory</code> , <code>vaspkit_adsorbate_thermo_correction</code> , <code>vaspkit_gas_thermo_correction</code> , <code>render_structure_views</code> , <code>identify_structure_fragments</code> .
Machine learning	Dataset curation, training, held-out evaluation, and active-learning candidate selection	<code>build_dataset_from_runs</code> , <code>mace_train</code> , <code>mace_evaluate</code> , <code>calculate_al_candidates</code> .
Quantum chemistry	Molecular structure preparation, conformer generation, xTB screening, ORCA preparation and execution, and molecular post-analysis	<code>enumerate_molecular_conformers</code> , <code>filter_conformer_ensemble</code> , <code>extract_optimized_molecules</code> , <code>crest_conformer_search</code> , <code>xtb_run_batch</code> , <code>analyze_xtb_results</code> , <code>orca_prepare</code> , <code>orca_scan_prepare</code> , <code>orca_optts_prepare</code> , <code>orca_nebts_prepare</code> , <code>orca_irc_prepare</code> , <code>orca_execute_batch</code> , <code>analyze_orca_results</code> .
Literature and metadata	Scholarly metadata resolution, web lookup, and page-level source inspection	<code>search_openalex</code> , <code>search_semantic_scholar</code> , <code>get_openalex_record</code> , <code>get_semantic_scholar_record</code> , <code>recommend_semantic_scholar</code> , <code>search_public_web</code> , <code>open_public_page</code> , <code>find_in_page</code> .
Writing and runtime utilities	Manuscript compilation and bounded workspace utilities	<code>compile_text</code> , <code>bash</code> , <code>apply_aider_edits</code> .

Some model-mediated utilities are intentionally excluded from the regular primitive inventory and listed separately in Table S2. These functions call external multimodal or reviewer-style models and therefore behave differently from deterministic scientific primitives. Separating them makes the boundary clearer between the core execution substrate of CatMaster and higher-level agentic services used for interpretation, figure generation, or manuscript review.

Table 8: Agentic or model-mediated tools kept separate from the regular primitive tool inventory.

Tool name	Short description
analyze_images	Analyze one or more local images with a multimodal model and return structured findings.
generate_nanobanana_figure	Generate a conceptual or manuscript-oriented figure from text instructions.
peer_review_pdf_manuscript	Run a lightweight external-model peer review on one local manuscript PDF.
peer_review_request	Send one manuscript PDF to all configured peer-review models and collect raw reviews.
polish_academic_prose	Read a manuscript file, polish its language with the academic polisher model, and write the result back.
review_pdf_manuscript	Review a local manuscript PDF directly with a multimodal model and return comment-only suggestions.
run_literature_research	Run a precise literature-grounding workflow and return a compact context pack.

1.2.3 Detailed Primitive Tool Inventory

Table S3 provides a one-sentence description for each regular tool. This level of detail is important because the CatMaster tool surface is meant to be scientifically interpretable: each entry states the minimal transformation that the runtime can execute directly, thereby making visible where a workflow must be composed from several primitives rather than delegated to a single opaque bundle.

Table 9: Detailed description table for the regular CatMaster tool surface.

Tool name	Family	Short description
mp_search_materials	Materials and atomistic	Search Materials Project with flexible criteria and export candidate materials metadata.
mp_download_structure	Materials and atomistic	Download one or more structures from Materials Project into the workspace.
create_molecule_from_smiles	Materials and atomistic	Build a 3D molecule from a SMILES string using RDKit.
build_slab	Materials and atomistic	Build slab models from bulk structures for specified Miller indices and terminations.
fix_atoms_by_layers	Materials and atomistic	Freeze the bottom atomic layers of slab structures.
fix_atoms_by_height	Materials and atomistic	Freeze atoms within specified height windows of slab structures.
fix_atoms_by_indices	Materials and atomistic	Fix (freeze) atoms by explicit 0-based indices for one structure or a directory batch.
supercell	Materials and atomistic	Create supercells from structure file(s) while preserving selective dynamics in POSCAR/VASP outputs.
enumerate_unique_sites	Materials and atomistic	Enumerate symmetry-inequivalent atomic sites for one structure and optionally write a JSON report.

Tool name	Family	Short description
create_vacancy	Materials and atomistic	Remove one explicit site or generate one vacancy structure per symmetry-inequivalent site group.
substitute_species	Materials and atomistic	Replace one explicit site or generate one substitution structure per symmetry-inequivalent site group.
insert_interstitial_at_coords	Materials and atomistic	Insert one or more explicit interstitial atoms at user-specified fractional or Cartesian coordinates.
enumerate_adsorption_sites	Materials and atomistic	Enumerate representative adsorption sites on a slab.
place_adsorbate	Materials and atomistic	Place an adsorbate on a slab and write the adsorbed structure with metadata.
generate_batch_adsorption_structures	Materials and atomistic	Generate batches of adsorbate-on-slab structures for screening.
make_neb_geometry	Materials and atomistic	Generate interpolated image geometries for a nudged elastic band workflow.
generate_strained_structures	Materials and atomistic	Generate a strain set from explicit deformation matrices or from a mode/value grid.
generate_kpath	Materials and atomistic	Generate a high-symmetry line-mode KPOINTS file from a relaxed bulk structure.
generate_phonon_displacements	Materials and atomistic	Generate finite-displacement supercell structures for a phonon force-constant workflow.
vasp_prepare	Materials and atomistic	Prepare a canonical single-structure VASP input set for relax/static/freq/dos/md presets.
vasp_band_prepare	Materials and atomistic	Prepare a dedicated line-mode VASP band-structure input set from a relaxed structure, explicit band KPOINTS, and optional fixed CHGCAR.
vasp_neb_prepare	Materials and atomistic	Prepare a canonical NEB VASP input tree from endpoint structures or an existing image tree.
vasp_dimer_prepare	Materials and atomistic	Prepare an official VASP improved-dimer input directory (IBRION=44).
make_dimer_mode_from_neb	Materials and atomistic	Derive a raw dimer direction from the two images adjacent to a chosen TS image.
make_dimer_mode_from_mace	Materials and atomistic	Approximate a dimer direction by finite-difference ASE/MACE vibrations on a TS guess.
mace_analyze_frequencies	Materials and atomistic	Compute MACE vibrational frequencies and export all mode records.
mace_relax_batch	Materials and atomistic	Submit multiple MACE relaxations in one DPDispatcher submission.
mace_sp_batch	Materials and atomistic	Run MACE single-point jobs for structures under one directory.
mace_neb_batch	Materials and atomistic	Submit MACE NEB jobs through DPDispatcher from explicit image-tree task directories.
vasp_execute_batch	Materials and atomistic	Submit prepared VASP calculations in single-folder or recursive batch mode.

Tool name	Family	Short description
analyze_vasp_results	Materials and atomistic	Summarize one VASP result directory or a batch of result directories into JSON and CSV artifacts.
analyze_vasp_neb_results	Materials and atomistic	Summarize a completed VASP NEB result directory into barrier, profile CSV, and profile plot artifacts.
analyze_trajectory	Materials and atomistic	Analyze an MD trajectory with MSD, diffusion-fit, RDF, and temperature/energy summary outputs.
vaspkit_adsorbate_thermo_correction	Materials and atomistic	Run VASPKIT task 501 for adsorbate thermochemistry and return parsed corrections.
vaspkit_gas_thermo_correction	Materials and atomistic	Run VASPKIT task 502 for gas-phase thermochemistry and return parsed corrections.
render_structure_views	Materials and atomistic	Render a structure into a stable four-view panel for visual inspection.
identify_structure_fragments	Materials and atomistic	Probe connected fragments in a periodic structure and return fragment-index summaries.
build_dataset_from_runs	Machine learning	Build an extxyz training dataset from one VASP result directory or a batch of VASP result directories using ASE's vasprun.xml parser.
mace_train	Machine learning	Launch a remote MACE training or fine-tuning job using the validated reference-script style MACE CLI contract.
mace_evaluate	Machine learning	Run remote MACE evaluation on an extxyz dataset and collect error metrics and per-configuration outputs.
calculate_al_candidates	Machine learning	Rank candidate structures for active learning using diversity and optional MACE committee disagreement.
enumerate_molecular_conformers	Quantum chemistry	Enumerate 3D molecular conformers from a SMILES string with RDKit ETKDGv3.
filter_conformer_ensemble	Quantum chemistry	Filter a conformer ensemble by energy window and geometry similarity.
extract_optimized_molecules	Quantum chemistry	Collect optimized molecular geometries from ORCA/xTB result folders into one reusable ensemble directory.
crest_conformer_search	Quantum chemistry	Run CREST conformer search for one molecule or a molecular batch.
xtb_run_batch	Quantum chemistry	Submit one molecular structure or a molecular batch to xTB.
analyze_xtb_results	Quantum chemistry	Summarize xTB/CREST result folders into JSON/CSV evidence.
orca_prepare	Quantum chemistry	Prepare ORCA input directories for molecular single-point, optimization, frequency, TDDFT, or NMR work.
orca_scan_prepare	Quantum chemistry	Prepare ORCA scan input directories for bounded molecular reaction-coordinate workflows.
orca_optts_prepare	Quantum chemistry	Prepare ORCA OptTS input directories for molecular transition-state refinement.

Tool name	Family	Short description
orca_nebts_prepare	Quantum chemistry	Prepare an ORCA NEB-TS job from reactant and product geometries.
orca_irc_prepare	Quantum chemistry	Prepare ORCA IRC input directories from a transition-state structure.
orca_execute_batch	Quantum chemistry	Submit one prepared ORCA job directory or a prepared batch root via DPDispatcher.
analyze_orca_results	Quantum chemistry	Summarize ORCA result folders into JSON/CSV evidence.
search_openalex	Literature and metadata	Search OpenAlex for exact scholarly metadata, not broad background search.
search_semantic_scholar	Literature and metadata	Search Semantic Scholar for exact paper metadata, abstracts, or seed papers.
get_openalex_record	Literature and metadata	Fetch one OpenAlex work by OpenAlex id or DOI.
get_semantic_scholar_record	Literature and metadata	Fetch one Semantic Scholar paper by paper id or DOI.
recommend_semantic_scholar	Literature and metadata	Expand a small seed set with Semantic Scholar recommendations.
search_public_web	Literature and metadata	Search the public web for broad scientific background or landing-page summaries.
open_public_page	Literature and metadata	Open a public page and extract normalized visible text.
find_in_page	Literature and metadata	Search normalized text within a previously identified public page.
compile_text	Writing and runtime utilities	Compile or statically validate a manuscript bundle and return LaTeX diagnostics and artifacts.
bash	Writing and runtime utilities	Execute a bounded bash script inside the workspace.
apply_aider_edits	Writing and runtime utilities	Apply structured search-and-replace edits to workspace files.

1.2.4 Skill Layer and Role-Specific Exposure

Skills form the second layer of CatMaster’s capability surface. Whereas tools define what operations are executable, skills define how recurring scientific procedures should be conducted. CatMaster stages experiment, machine-learning, quantum-chemistry, and writing skills into the DeepAgent runtime as modular instruction packages. The experiment skill set covers, among others, materials discovery and bulk selection, slab construction and surface modelling, adsorbate and intermediate generation, adsorption-site screening, surrogate screening and relaxation with MACE, VASP input preparation, batch execution, transition-state and NEB workflows, thermochemical reporting, defect and dopant screening, band-structure and density-of-states analysis, phonon workflows, and literature grounding. The machine-learning skill set covers MACE dataset curation, fine-tuning and benchmark evaluation, and active-learning relabel loops. The quantum-chemistry skill set covers conformer search and pre-optimization, xTB screening and pruning, ORCA optimization and thermochemistry, scan-to-transition-state procedures, NEB-to-IRC workflows, and NMR ensemble workup. The writing skill set includes scientific writing, citation management, figure design and captioning, results-and-discussion drafting, scientific visualization, venue templates, and manuscript-formatting modules.

An important implementation distinction is that skill metadata, including any recommended allowed-tool list in a skill header, does not itself define the executable runtime surface. Skills

serve as reusable, plug-and-play scientific operating procedures that shape specialist behavior, whereas the actual visible tools are determined by the specialist or worker to which those skills are bound. This separation is central to the CatMaster design. It allows new domain expertise to be added by authoring or refining skill modules without forcing a parallel expansion of the agent hierarchy, and it preserves a clear contract between scientific guidance and executable capability. In practice, this is how CatMaster reconciles a deliberately small specialist hierarchy with broad scientific depth: experts are introduced as modular skill packages, and tools remain composable primitives over well-defined artifact types.

Tables S4 and S5 summarize the staged skill inventory and its role-specific exposure. These tables should be read as the procedural complement to the primitive tool inventory above: the tools specify what can be executed, whereas the skills specify how recurring scientific procedures are organized and constrained within each specialist view.

Table 10: CatMaster skill inventory by family (36 skills total before role-specific filtering).

Skill family	Count	Skill modules
Experiment	20	adsorbate-and-intermediate-generation, adsorption-screening, adsorption-site-screening, band-and-dos-analysis, bulk-relax-and-reference, defect-and-dopant-screening, elastic-property-workup, literature-grounding, mace-screening-and-relaxation, materials-discovery-and-bulk-selection, md-diffusion-analysis, phonon-displacement-workflow, reaction-neb-analysis, slab-construction-and-surface-modeling, structure-visual-inspection, surface-and-termination-screening, thermo-free-energy-and-reporting, transition-state-neb, vasp-batch-execution, vasp-input-preparation.
Machine learning	3	active-learning-relabel-loop, mace-dataset-curation, mace-finetuning-and-benchmark.
Quantum chemistry	6	conformer-search-and-preopt, nebts-and-irc, nmr-ensemble-workup, orca-optfreq-thermochemistry, scan-to-ts, xtb-screen-and-prune.
Writing	7	achemso-latex-manuscript, citation-management, figure-design-and-captioning, results-and-discussion-writing, scientific-visualization, scientific-writing, venue-templates.

Table 11: How skill families are exposed to runtime roles after role-specific filtering.

Runtime role or view	Skill-family exposure in the active implementation
Research experiment view	Filtered subset of experiment skills staged for the research specialist so that top-level planning can reason about experiment conventions without inheriting the full execution surface.
Research writing view	Filtered subset of writing skills staged for the research specialist so that top-level planning can reason about manuscript structure and deliverables without becoming the primary drafting worker.

Runtime role or view	Skill-family exposure in the active implementation
Experiment-specialist and materials-worker views	Filtered experiment-skill views compatible with their bound periodic and materials tool surfaces, including skills for literature grounding, structure inspection, adsorption screening, slab construction, VASP preparation, and transition-state workflows.
ML-worker view	Full machine-learning family staged as a filtered role-specific view, including MACE dataset curation, fine-tuning and benchmark evaluation, and active-learning relabel loops.
Molecular-QC-worker view	Full quantum-chemistry family staged as a filtered role-specific view, including conformer, xTB, ORCA, TS/IRC, and NMR-oriented modules.
Writing-side views	Filtered writing-family views staged for author-facing drafting, local polishing, experiment-facing reporting, and peer-review preparation, with scientific writing retained across these writing-side views.

2 Benchmark Construction and Evaluation Details

2.1 Benchmark Tasks and Operational Prompts

The benchmark suite was designed to test whether a model embedded inside CatMaster could complete short but realistic computational-science episodes from an initial natural-language request to final evidence-bearing deliverables. Each scenario therefore specified not only a scientific objective but also explicit output requirements, including preserved structures, plots when required, and a final written summary. This design differs from narrow artifact-level checks because it forces the model to maintain consistency across retrieval, setup, execution, analysis, and reporting within one bounded scenario.

Table 12: Benchmark scenario definitions and operational prompt requirements.

Scenario	Scientific scope	Operational prompt and constraints	Required deliverables
T1	Retrieval and DFT-awareness benchmark	Retrieve experimentally grounded structures for bcc Fe, Si and SrTiO ₃ from Materials Project, prepare calculation-ready VASP relaxation inputs, and choose suitable metal versus semiconductor smearing and spin settings. Public web browsing was disallowed; the scenario had to be completed through the designated materials-access tools.	Calculation-ready VASP input folders for the three materials, together with a <code>summary.md</code> recording the selected materials-project identifiers and key DFT settings.
T2	Adsorption screening benchmark	Starting from a provided Fe(110) slab and CO adsorbates, enumerate relevant adsorption sites and both molecular orientations, run standard PBE geometry optimizations without dispersion, and identify the best adsorption configuration together with its energetics and bond length.	Relaxed final geometries for the enumerated adsorption cases and a final summary reporting adsorption energies, the energy definition, the preferred configuration, and the relevant bond length.

Scenario	Scientific scope	Operational prompt and constraints	Required deliverables
T3	Transition-state benchmark	Starting from provided initial and final structures for O migration on Au(111), first relax both endpoints with MACE, then perform a MACE-only CI-NEB calculation with three intermediate images and an O-only vibrational analysis. The scenario explicitly forbade escalation to DFT.	Relaxed endpoint structures, a usable MEP or barrier artifact under results/ , and a final summary reporting the barrier with respect to hollow0 together with the three O-atom vibrational modes.
T4	Density-of-states benchmark	Starting from three relaxation-ready bulk inputs, continue to DOS calculations without redoing bulk relaxation, determine metallic versus gapped behaviour, estimate band gaps when present, determine spin polarization, and provide physically grounded DOS interpretations with plots.	DOS outputs and one DOS plot per material, plus a final summary reporting metallic or gapped classification, band gap where present, and spin polarization including magnetic moment when relevant.

In the benchmark launcher, each scenario was instantiated as an isolated workspace and run through the same CatMaster experiment lane used for ordinary execution. Three independent repeats were performed for each scenario-model pairing, so each model contributed 12 runs in total. Because the benchmark prompts required final written summaries and persisted artifacts, models that reached scientifically plausible intermediate states but failed to close the reporting loop were intentionally penalized.

2.2 Filesystem-Based Judging and Manual Review

Automated scoring was implemented in the benchmark judge using scenario-specific prompt text, rubric items, scenario maxima, hard-cap rules and reference facts encoded in the repository source. The judge inspected only persisted workspace evidence and explicitly avoided assuming a fixed internal folder layout below the benchmark root. Equivalent deliverables discovered under alternative paths were still creditable, whereas unsupported claims, missing final summaries, missing key artifacts, protocol violations and hallucinated interpretations triggered deductions or hard caps depending on the scenario. To reduce evaluator bias, model identities were blinded throughout judging and subsequent manual review: both the LLM judge and the human review ledger operated on anonymized labels (*ModelA–ModelD*) rather than backend names. This scoring policy was important for distinguishing scientific correctness from workflow closure and evidence traceability.

The judging agent operated with two explicit prompt layers. First, a fixed system prompt instructed the judge to score only from filesystem evidence, treat the mounted root / as the candidate `files` directory, avoid assuming any deeper fixed path layout, prefer targeted discovery over large indiscriminate reads, give credit to valid deliverables found at nonstandard locations, avoid rewarding stylistic confidence, ignore hidden assumptions outside the mounted root, and apply hard caps exactly when triggered. Second, a scenario-specific user prompt provided the original benchmark scenario text, the full rubric, the encoded hard caps, scenario-specific reference facts, keyword hints, and a shallow tree preview of the candidate workspace. The user prompt template was:

```
Judge the benchmark run for scenario T<ID> (<label>).
Candidate workspace: root “/” is the run’s files directory only;
```

workspace name; anonymized model label only.
 Original scenario prompt: full benchmark scenario prompt.
 Scoring rubric (max score): rubric items.
 Hard caps: encoded hard-cap rules.
 Reference facts: scenario-specific reference facts.
 Search hints: start from the shallow tree preview below;
 use keyword-driven discovery; useful keywords for this scenario.
 Shallow tree preview: directory preview.
 Required behavior: explore the candidate root fairly;
 cite actual evidence files used; credit valid deliverables at
 nonstandard locations; reduce the score conservatively when
 evidence is weak or missing.

For reproducibility, the scenario-specific rubric items and weights used by the judge are listed below exactly as encoded in the benchmark source.

Table 13: Scenario-specific rubric items and score weights encoded in the automated judge.

Scenario	Rubric item	Max score	Criterion
T1	T1-1	5.0	Retrieval correctness: correct Materials Project identities and experimentally grounded selection, with fair treatment of SrTiO ₃ polymorph ambiguity.
T1	T1-2	5.0	Structure preparation completeness: all three materials have calculation-ready VASP input directories or equivalent prepared inputs.
T1	T1-3	4.0	DFT awareness: Fe spin handling, metal versus semiconductor smearing, and reasonable ISMEAR/SIGMA choices.
T1	T1-4	1.0	Summary traceability: summary clearly records mp-id and key parameters.
T2	T2-1	6.0	Slab and adsorption setup quality: sensible use of the provided Fe(110) slab and adsorbates.
T2	T2-2	8.0	Site enumeration breadth: major adsorption site families and both orientations are covered.
T2	T2-3	6.0	DFT protocol correctness: standard PBE, no dispersion, Fe spin handled, and no obvious protocol misuse.
T2	T2-4	6.0	Geometry optimization completeness: most enumerated cases actually ran and relaxed structures are preserved.
T2	T2-5	5.0	Result quality and chemical sanity: strongest candidates and key bond lengths or energies are scientifically reasonable.
T2	T2-6	4.0	Summary and provenance quality: final summary exists, cases are reported coherently, and best-configuration interpretation is present.
T3	T3-1	7.0	Protocol compliance: MACE-only, mace-mh-1, no dispersion, CI-NEB, 3 intermediate images, correct thresholds, and no DFT.
T3	T3-2	4.0	Endpoint relaxation quality: both endpoints relaxed below 0.01 eV Å ⁻¹ first.
T3	T3-3	6.0	NEB and MEP execution quality: usable path, barrier evidence, and image outputs.
T3	T3-4	4.0	Barrier accuracy: barrier and highest-energy image are close to reference.
T3	T3-5	3.0	Vibration analysis quality: O-only analysis, 3 modes, and one imaginary mode near the transition state.

Scenario	Rubric item	Max score	Criterion
T3	T3-6	1.0	Summary and evidence quality.
T4	T4-1	6.0	DOS workflow completeness for all three materials.
T4	T4-2	6.0	Metallic versus gapped classification correctness.
T4	T4-3	6.0	Bandgap and spin interpretation quality.
T4	T4-4	5.0	DOS plot delivery and physically grounded interpretation.
T4	T4-5	2.0	Summary completeness and provenance.

The scenario-specific hard caps used by the judge are listed below exactly as encoded in the benchmark source.

Scenario	Hard-cap rules encoded in the automated judge
T1	If key reported data contains model hallucination unsupported by workspace evidence, total score must be ≤ 9 .
T2	If key reported data contains model hallucination unsupported by workspace evidence, total score must be ≤ 20 . If only 1–2 sites were evaluated without meaningful enumeration, total score must be ≤ 15 . If there are failed or incomplete runs and the candidate does not produce a final summary deliverable, total score must be ≤ 20 . If relaxed structures are not delivered anywhere in the workspace, total score must be ≤ 22 .
T3	If key reported data contains model hallucination unsupported by workspace evidence, total score must be ≤ 15 . If the run performs DFT for the transition-state scenario, total score must be 0. If the model is not <code>mace-mh-1</code> or the protocol is not MACE-only, total score must be ≤ 10 . If vibration analysis is missing, total score must be ≤ 20 . If endpoint relaxation before NEB is missing, total score must be ≤ 16 .
T4	If key reported data contains model hallucination unsupported by workspace evidence, total score must be ≤ 15 . If bulk relaxation is redone instead of continuing from provided starts, total score must be ≤ 18 . If DOS plots are missing, total score must be ≤ 20 . If Fe is judged non-spin-polarized, total score must be ≤ 15 . If bandgaps are omitted entirely, the T4-3 subscore cannot exceed 2.

Because several runs exposed borderline rubric interpretations, we performed a targeted human review pass and updated the final ledger wherever the automated judge was clearly over- or under-penalizing a scientifically acceptable or unacceptable behaviour. The principal manual changes are summarized in Table S6. These revised scores, rather than the raw first-pass judge outputs, are the values used in the main-text figure and Results discussion.

Table 15: Manual-review overrides applied to the raw judge ledger.

Run	Final score	Reason for manual adjustment
ModelA T2_R2	35.0 / 35	The raw deduction was driven by the appearance of <code>IVDW_NL</code> in <code>vasprun.xml</code> . Manual review concluded that this field can be written automatically in newer VASP versions and is not by itself evidence that dispersion was enabled. The score was therefore restored to full credit, while retaining the provenance issue only as a red flag.

Run	Final score	Reason for manual adjustment
ModelA T4_R1	25.0 / 25	The raw judge penalized direct or indirect gap language in a DOS-only benchmark. Manual review judged this as an overextended statement rather than a failure of the required DOS deliverables, so the deduction was removed.
ModelB T1_R1	14.0 / 15	SIGMA=0.1 for Fe was not treated as a substantive error, but the summary placement remained incorrect, so the run stayed at 14.0 with the location issue preserved as the main deduction.
ModelB T1_R3	13.5 / 15	An additional deduction was introduced because the summary was written to the wrong location, lowering the score from the raw judge value.
ModelB T2_R1	20.0 / 35	Manual review reclassified the main issue as incomplete scenario closure rather than adsorption-energy-definition wording. Because the case enumeration was unfinished and the required final summary was missing, the run was reduced to the hard-cap regime for incomplete execution.
ModelB T2_R2	35.0 / 35	The same IVDW_NL provenance issue as in ModelA was judged non-fatal, so the run was restored to full credit.
ModelB T2_R3	20.0 / 35	This run was likewise reinterpreted as incomplete, with missing final closure and unresolved failed cases dominating the score rather than prose-level adsorption-energy-definition issues.
ModelB T4_R3	24.0 / 25	A visual-readability concern in the DOS plot was removed as a deduction. Only a light reporting/provenance penalty was retained.
ModelC T4_R1–R3	25.0 / 25 each	The deduction pattern previously applied to the DOS scenario was judged inapplicable under the final aligned rubric. All three repeats were therefore treated as full-credit DOS runs, leaving T3 as the only stable deficit for this model.
ModelD T2_R2	34.0 / 35	Manual review concluded that one damaged case had not actually been resolved. The run still received high credit because the anomaly was honestly reported, but it was no longer treated as perfect.
ModelD T2_R3	20.0 / 35	A failed or corrupted adsorption case was written up as though it were normal. Manual review therefore treated the run as containing hallucinated downstream interpretation and lowered it into the hard-cap regime.
ModelD T3_R2	15.0 / 25	The NEB or path result for this repeat was not actually usable after inspection of the underlying calculation evidence. The path and barrier sub-scores were therefore removed, substantially lowering the total.

2.3 Human-Reviewed Benchmark Results

The final human-reviewed benchmark results are summarized in Tables S7 and S8. The two strongest models were GPT-5.4 (high reasoning effort) and Sonnet-4.6 (high reasoning effort), which reached near-ceiling performance across the four short end-to-end scenarios. Gemini-3.1 Pro retained substantial scientific capability but lost more score through incomplete closure and weaker reporting discipline. Mimo-V2 Pro (high reasoning effort) remained workable inside CatMaster but showed a clear gap in robustness and failure isolation relative to the frontier tier.

Table 16: Human-reviewed aggregate benchmark performance.

Internal id	Model backend	Overall mean	T1	T2	T3	T4
ModelA	GPT-5.4 (high)	100.000 / 100	15.000	35.000	25.000	25.000
ModelC	Sonnet-4.6 (high)	98.000 / 100	15.000	35.000	23.000	25.000
ModelB	Gemini-3.1 Pro (high)	87.667 / 100	14.000	25.000	24.333	24.333
ModelD	Mimo-V2 Pro (high)	82.500 / 100	13.500	29.667	21.333	18.000

Table 17: Human-reviewed repeat-level scores and dominant interpretation for each scenario.

Model	Scenario	R1	R2	R3	Mean	Dominant interpretation
ModelA	T1	15.0	15.0	15.0	15.000	Fully successful retrieval and DFT-parameter selection across all repeats.
ModelA	T2	35.0	35.0	35.0	35.000	Complete adsorption screening with stable closure after manual removal of a provenance-only deduction.
ModelA	T3	25.0	25.0	25.0	25.000	Fully successful bounded transition-state workflow across all repeats.
ModelA	T4	25.0	25.0	25.0	25.000	Fully successful DOS workflow after removal of a non-essential overclaim penalty.
ModelC	T1	15.0	15.0	15.0	15.000	Fully successful retrieval benchmark across repeats.
ModelC	T2	35.0	35.0	35.0	35.000	Fully successful adsorption screening across repeats.
ModelC	T3	23.0	23.0	23.0	23.000	Stable but systematically flawed transition-state reasoning: vibration analysis was placed on the endpoint minimum rather than on the transition-state structure.
ModelC	T4	25.0	25.0	25.0	25.000	Stable and complete DOS execution after manual removal of legacy rubric artifacts.
ModelB	T1	14.0	14.5	13.5	14.000	Good structure retrieval and setup knowledge, with losses mainly from reporting location and parameter-tailoring details.
ModelB	T2	20.0	35.0	20.0	25.000	Scientifically promising adsorption reasoning, but unstable scenario closure with two repeats failing to complete the required reporting loop.
ModelB	T3	25.0	23.0	25.0	24.333	Mostly strong transition-state execution, with one repeat applying frequency analysis to the wrong structure.
ModelB	T4	24.0	25.0	24.0	24.333	Largely successful DOS workflow, with only light reporting and provenance penalties.

Model	Scenario	R1	R2	R3	Mean	Dominant interpretation
ModelD	T1	13.0	13.5	14.0	13.500	Acceptable retrieval performance but weaker treatment of polymorph ambiguity and nonmagnetic INCAR cleanup.
ModelD	T2	35.0	34.0	20.0	29.667	Strong best-case adsorption reasoning, but inconsistent handling of damaged runs and one hallucinated write-up of a failed case.
ModelD	T3	25.0	15.0	24.0	21.333	Large variance, including one repeat with unusable path evidence and another with a non-O-only vibration analysis.
ModelD	T4	24.5	25.0	4.5	18.000	The strongest robustness failure in the suite: one repeat restarted the wrong upstream step and failed to deliver the required DOS products.

3 General-Purpose Machine Learning Benchmark Details

3.1 Common MatBench Prompt and Scenario Matrix

The general-purpose modelling study was designed to test whether CatMaster could carry a materials-machine-learning project from request to final benchmark report under the same autonomous runtime used elsewhere in this work. We therefore did not provide prewritten training scripts or fixed modelling recipes. Instead, each scenario was launched from a common prompt template that asked the agent to complete feature engineering, model training, hyperparameter search, official MatBench evaluation, reproducible script generation, and final markdown reporting within the local workspace. The prompt explicitly allowed the agent to optimize its modelling strategy in at most five rounds while requiring that all model selection remain strictly confined to the training portion of each official outer fold.

In the workspace, there exists a MatBench {dataset} dataset. Complete the machine-learning modelling task, including feature engineering, model training, hyperparameter searching, and evaluation. Write a detailed report describing the modelling methods, chosen features, model classes, and best hyperparameters, and save all relevant scripts needed to reproduce the workflow from scratch. You may optimize the featurization, modelling, and training strategy in a maximum of five rounds, but you must not violate the official MatBench split principle. For regression tasks, generate test folds with shuffled five-fold `KFold`; for classification tasks, generate test folds with shuffled five-fold `StratifiedKFold`; in both cases use `random_state= 18012019`. For each fold, train, validate, and select the best model using only that fold’s training data, then predict the untouched test fold, record the mean MAE or ROC-AUC, and save the test-fold data and model artifacts.

Table 18 summarizes the six selected scenarios. Together they span composition-only and composition-plus-structure inputs, regression and classification objectives, and dataset sizes ranging from a few hundred entries to more than 10^5 structures.

Table 18: MatBench scenario matrix used for the general-purpose modelling evaluation.

Scenario	Input primitive	Task type	Metric	Samples	Role in the benchmark
Steels	Composition	Regression	MAE	312	Small-data experimental mechanical-property regression used to test whether CatMaster could build compact descriptor pipelines rather than overcomplicate the workflow.
<code>expt_gap</code>	Composition	Regression	MAE	4,604	Moderate-size electronic-property regression with a strongly zero-inflated target distribution, useful for testing whether the agent would discover nonstandard regression strategies.
<code>is_glass</code>	Composition	Classification	ROC-AUC	5,680	Composition-only classification task used to test whether CatMaster could move from regression-style descriptor search to probabilistic classification under fold-safe selection.
<code>jdft2d</code>	Structure + composition	Regression	MAE	636	Small structure-aware 2D materials regression task probing whether CatMaster would augment composition descriptors with geometry and local-environment information.
<code>mp_is_metal</code>	Structure + composition	Classification	ROC-AUC	106,113	Very large structure-aware classification task testing whether the agent could scale to high-throughput feature construction and stable GPU-accelerated model selection.
Phonons	Structure + composition	Regression	MAE	1,265	Structure-dominated regression task chosen as the hardest case, where strong published performance depends on specialized geometric graph models rather than only descriptor engineering.

3.2 Typical CatMaster Workflow Patterns

The analysis for workspaces show that CatMaster did not apply one generic AutoML template across all six scenarios. Instead, it used the allowed five-round budget to test a bounded family of candidate inductive biases and then locked the best fold-safe pipeline. In the composition-only scenarios, the search mostly remained in the descriptor-plus-tabular regime. On steels, CatMaster generated several composition feature banks and selected a compact observed-element-fraction representation paired with ExtraTrees. On `expt_gap`, it compared ElasticNet, ExtraTrees, XGBoost, SVR, and a two-stage hurdle XGBoost, ultimately selecting the hurdle model in all five outer folds because the target distribution contained many zero-gap entries. On `is_glass`, it converged on extended composition descriptors with XGBoost, with and without SelectKBest, and both winning folds remained within that same descriptor family.

For the structure-aware scenarios, the representation widened rather than simply switching to a graph model by default. On `jdft2d`, CatMaster compared composition-only, composition-plus-geometry, and composition-plus-geometry-plus-CrystalNN feature families, and then selected a weighted ExtraTrees-HistGradientBoosting ensemble over the richest descriptor set. On `mp_is_metal`, it progressively grew the feature space from composition-only inputs to a 322-feature representation combining composition, elemental fractions, lightweight structural descriptors, and neighbor statistics, then selected GPU XGBoost in every outer fold. These

runs show that CatMaster already behaves like an adaptive materials-ML practitioner: it can infer when a task is best handled by compact descriptors, rich handcrafted structure features, or ensemble selection, without requiring a human to precommit to a model family in advance.

The phonons scenario was qualitatively different. In Trial 1, CatMaster executed a fixed five-round workflow that moved from composition descriptors to JARVIS-CFID, then to a hybrid handcrafted descriptor stack, then to a crystal GNN, and finally to a validation-weighted blend of the descriptor and graph experts. Importantly, the best single expert in that run was still the handcrafted descriptor model, not the graph network. After the user explicitly requested one additional self-improvement opportunity, CatMaster reinvestigated the workspace, diagnosed a broken symmetry-feature path, enabled real XGBoost early stopping, replaced a single holdout with inner cross-fitted CV, added SOAP-based geometry descriptors, and built a routed descriptor specialist stack. It also implemented a new angle-aware graph pilot on small scale. However, that pilot underperformed the previously saved graph expert and therefore was not promoted into the final one-shot full benchmark. The final Trial 2 result improved through better descriptor-side modelling and routing, but it still did not close the gap to the strongest specialized phonon GNN baselines. This shows a clear boundary of the present CatMaster system.

3.3 Full Performance Summary

Table 19 compiles the CatMaster outcomes used in the main-text comparison. In five of the six scenarios, the first autonomous CatMaster run already landed at or near the top of the official MatBench leaderboard. The only clear exception was phonons, where even the improved second trial remained behind specialized structure-centric baselines.

Table 19: Full performance summary for the general-purpose modelling evaluation.

Scenario	Run	CatMaster locked pipeline	CatMaster result	Strongest reference on official leaderboard	Relative outcome
Steels	Trial 1	Round 4 observed-element-fraction features + ExtraTreesRegressor	80.6594 MAE	TPOT-Mat, 79.9468 MAE	Near-best; CatMaster ranked second on the official leaderboard.
<code>expt_gap</code>	Trial 1	Round 5 hurdle XGBoost on the all-union composition feature bundle	0.3025 eV MAE	Darwin, 0.2865 eV MAE	Near-best; CatMaster ranked second.
<code>is_glass</code>	Trial 1	Extended composition descriptors + XGBoost / SelectKBest-XGBoost	0.9524 ROC-AUC	MODNet v0.1.12, 0.9603 ROC-AUC	Near-best; CatMaster ranked second.
<code>jdft2d</code>	Trial 1	Composition + 2D geometry + CrystalNN site descriptors with a 0.4 ExtraTrees / 0.6 HistGradientBoosting ensemble	33.0868 meV atom ⁻¹ MAE	CatMaster, 33.0868 meV atom ⁻¹ MAE	Best result on the official leaderboard.
<code>mp_is_metal</code>	Trial 1	322-feature composition + fraction + structure + neighbor-statistics representation with GPU XGBoost	0.9787 ROC-AUC	CatMaster, 0.9787 ROC-AUC	Best result on the official leaderboard.
Phonons	Trial 1	Validation-weighted blend of the Round 3 hybrid descriptor search and the Round 4 crystal GNN	45.5630 cm ⁻¹ MAE	MegNet, 28.7606 cm ⁻¹ MAE	Clear gap to specialized phonon baselines.

Scenario	Run	CatMaster locked pipeline	CatMaster result	Strongest reference on official leaderboard	Relative outcome
Phonons	Trial 2	Routed descriptor specialist stack + SOAP geometry descriptors + frozen graph expert fusion after one self-improvement cycle	37.6924 cm ⁻¹ MAE	MegNet, 28.7606 cm ⁻¹ MAE	Substantial self-improvement over Trial 1, but still below specialized phonon GNN leaders.

4 Cu(111) RWGS Case Notes

The Cu(111) RWGS study was retained in the submission package as a boundary case rather than a headline success case. In contrast to the Pt(111) rediscovery, the clean Cu(111) terrace presented a weakly binding adsorption landscape in which both endpoint definition and barrier optimization became substantially less stable. The purpose of this note is therefore not to restate a completed mechanism, but to clarify what the two retained Cu(111) routes were designed to test and why the main text treats them conservatively.

4.1 Two Complementary Cu(111) Routes

The literature-guided route asked whether CatMaster could translate the clean-Cu(111) literature into a bounded simulation-ready baseline and then validate those canonical branch families under one strict MACE protocol. In practice, this route recovered the expected carboxyl, direct/redox, and formate branch families, rebuilt several local endpoints successfully, and obtained one quantitatively accepted elementary event: local formate entry. However, the remaining CO-forming branches were not retained because the decisive bands stayed high-force or multi-step, or because validated local product minima could not be maintained under unconstrained relaxation.

The autonomous-exploration route asked a different question: whether CatMaster could recover a comparable Cu(111) basin structure without branch-level priors. This route expanded to a much broader low-coverage state space and assembled a larger network packet, including CHO₂* + H*, CH₂O₂*, CHO* + HO*, CO* + H* + HO*, and CO* + H₂O* regions. It also produced several locally supported microsegments and one strict split-basin handoff. Nevertheless, the network remained globally discontinuous because the unresolved handoffs repeatedly collapsed into high-force bands, hidden intermediates, or plateau-like and non-primitive paths.

4.2 Interpretive Scope

Taken together, these two Cu(111) routes support a narrower but more informative conclusion than a simple success-or-failure label. The literature-guided route shows that CatMaster can reconstruct a constrained mechanistic baseline and test it without overclaiming. The autonomous route shows that the same runtime can recover a substantially broader reactive state space, while still leaving an auditable record of why strict closure was not yet earned. In both cases, the limiting factors were not purely symbolic chemical reasoning, but the combination of geometry-sensitive path semantics and a MACE NEB lane that often stalled on the weakly binding Cu(111) adsorption landscape. The corresponding original manuscript drafts for both routes are archived in Section 6.

5 End-to-End SAC Design Project Details

The graphene-supported single-atom catalyst project was the strongest closure case in the present study. Unlike the benchmark scenarios, the MatBench episodes, or the mechanism papers, this campaign required CatMaster to keep the same research thread alive across scope definition, surrogate-stage exploration, higher-fidelity DFT arbitration, thermodynamic upgrading, model repair, manuscript drafting, and editor-style review. The scientific endpoint was not a single calculation but an ACS-style manuscript package anchored to a retained DFT evidence hierarchy.

5.1 Initial and Continuation Prompts

Two user prompts defined the SAC campaign closure logic. The first established the scientific scope and the requirement to end in a publication-level short paper. After that first bounded paper was judged insufficient, a second continuation prompt explicitly reopened the same project and required CatMaster to continue through higher-fidelity validation and submission-facing revision rather than terminating at the screening stage.

Initial project prompt.

In the workspace exist a template 5x5 graphene and FeN₄ motif single atom catalyst structure (unoptimized). Next I want you to conduct a systematic research on 2e CO₂RR SACs (CO₂ →CO) within a topic: systematically investigate the effect of central atom / 1st round shell dopant (N₄ sites, choose one site and one dopant to dope) and 2nd round shell dopant (C connecting the N). You should choose some chemically reasonable metal and dopants for investigation. You can use MACE mh-1 with dispersion for large scale screening and should be the major information source as DFT surrogate (better less than 500 geometry relaxation tasks), and you can perform some DFT calculation data collection then fine-tuning before large scale screening if you think it is a better option. What you should consider are two major factors, one is the stability of the SAC, and the second is the CO₂ to CO reaction energy profile (where you should at least consider CO₂ →COOH*, COOH*→CO*, and CO*→CO(g)). You should use dispersion correction along the calculations. Make a reasonable scope of investigation proposal and finally write a formal publication-level short paper about your findings in the end with some kind of novelty.

Continuation prompt after the bounded first paper.

You are allowed more experimental resources, complete the validation and investigation and do not stop as bounded screening. Please complete the free-energy treatment and MACE finetuning for alignment more complete results, and limited implicit solvation validation and comparison are allowed (though do not make it a large-scale screening due to computational resources budget), make it a submission-ready ACS-style catalysis research paper. Do not make it bounded, I have allowed you a sufficient resources.

5.2 Project Brief and Closure Trajectory

The original request asked CatMaster to start from a provided graphene/FeN₄ template and systematically investigate two-electron CO₂ reduction to CO by varying the central metal, a single first-shell substitution, and a second-shell dopant, while primarily using MACE mh-1 with dispersion as the screening engine and ending in a formal short paper. After the first campaign terminated as a bounded screening note, a second explicit continuation request reopened the project with additional resources and required CatMaster to complete free-energy treatment, local model alignment, targeted higher-fidelity validation, and a submission-facing manuscript package rather than stopping at preliminary screening.

Table 20: Closure-stage ledger for the SAC design campaign.

Stage	What CatMaster completed	Representative artifacts
Initial brief	Parsed the open-ended catalyst-design request and defined a bounded graphene-supported MN ₄ motif space with metal-center, first-shell, and second-shell substitutions.	metadata/runs/run_20260324_014422_508f69/ui_prompt.txt; metadata/runs/run_20260324_014422_508f69/run_state.json
Broad surrogate screen	Executed a 29-motif, 107-relaxation MACE + dispersion exploration and generated the first catalyst shortlist and screening report.	co2rr_sac_screening/notes/co2rr_sac_screening_report.md; co2rr_sac_screening/notes/co2rr_descriptor_map_v2.png
Primary DFT arbitration	Expanded to a 35-motif DFT matrix over bare, COOH*, and CO* core states and retained only motifs that preserved the intended anchored pocket.	co2rr_sac_screening/notes/submission_grade/primary_matrix_dft_ranking.csv; co2rr_sac_screening/notes/submission_grade/primary_matrix_dft_summary.json
Solvation and explicit thermodynamics	Completed limited implicit-solvation checks and explicit adsorbate-frequency CHE analysis on the retained shortlist, converting the study from vacuum screening to publication-facing solvated thermodynamics.	co2rr_sac_screening/notes/submission_grade/solvation_validation/solvation_validation_report.md; co2rr_sac_screening/notes/submission_grade/thermo_package/submission_grade_thermo_report_with_n_nin3b.md
Local model repair	Diagnosed the stale/incomplete aligned-model lane, repaired it, and demonstrated major held-out improvement before using it only for triage.	co2rr_sac_screening/notes/submission_grade/model_alignment_status.md; co2rr_sac_screening/calculations/submission_grade/model_alignment/analysis/test_metrics_overall_comparison.csv; co2rr_sac_screening/calculations/submission_grade/model_alignment/analysis/test_parity_comparison.png
Bounded DFT follow-up	Used the repaired aligned model to nominate a narrow Co/Ni N ₃ B follow-up, confirmed N–NiN ₃ B by DFT, and rejected B–NiN ₃ B because of strong H overbinding.	co2rr_sac_screening/notes/submission_grade/aligned_followup_dft_summary.md; co2rr_sac_screening/notes/submission_grade/n_nin3b_submission_grade_extension.md
Manuscript package generation	Drafted and compiled a new ACS-style manuscript, Supporting Information, and TOC graphic around the upgraded evidence hierarchy.	writing/co2rr_sac_submission_grade/manuscript.pdf; writing/co2rr_sac_submission_grade/supporting_information.pdf; writing/co2rr_sac_submission_grade/toc_graphic.png
Internal peer-review recovery	Ran editor-style review, revised the package through a minor-revision cycle, and reached a final readiness judgment.	notes/peer_review/

5.3 Final Catalyst-Facing Conclusions and Package Status

The final catalyst conclusions were assigned to the upgraded DFT and solvated-thermodynamic package rather than to the surrogate screen. In the final explicit solvated ranking, B–CoN₄,

NiN₃B, and N–NiN₃B occupied the top three positions with limiting proton-coupled electron transfer costs of 0.015, 0.062, and 0.080 eV, respectively. CoN₄ remained a robust benchmark at 0.118 eV, P–CoN₄ was retained as a chemically informative overbinding comparator at 0.211 eV, N–CoN₄ defined a more release-favored edge at 0.361 eV, and CuN₄ remained the easy-CO-release but underactivated boundary at 1.409 eV. The aligned-model repair did not alter this evidence hierarchy directly; instead, it changed the project by surfacing N–NiN₃B as a real DFT-confirmed extension while preventing the system from overcommitting to B–NiN₃B.

The project also closed at the publication package level more strongly than any other case in this paper. The final editor-style readiness memo concluded that the remaining blocker was no longer scientific. Instead, the package was judged “Conditionally Acceptable / Ready pending human-supplied submission metadata,” meaning that author names, affiliations, contact information, funding, and acknowledgments still had to be inserted, but the scientific narrative, evidence hierarchy, and manuscript package itself had reached a publication-facing form.

Table 21: Final SAC catalyst ranking used in the archived manuscript package.

Motif	ΔG_1 / eV	ΔG_2 / eV	ΔG_3 / eV	Interpretation
B–CoN ₄	0.015	-0.288	0.908	Strongest activation-side motif in the final solvated explicit CHE ranking.
NiN ₃ B	0.062	-0.152	0.725	Closest overall competitor to B–CoN ₄ in the retained set.
N–NiN ₃ B	0.080	0.045	0.510	DFT-confirmed aligned-follow-up entrant that remained third after full thermodynamic upgrade.
CoN ₄	0.006	0.118	0.512	Benchmark motif that shifts the limiting PCET from COOH* formation to COOH* reduction.
P–CoN ₄	-0.868	0.211	1.292	Overbinding comparator: favorable early stabilization paired to a severe CO-release penalty.
N–CoN ₄	0.361	0.164	0.110	Release-favored Co-based edge of the retained catalyst landscape.
CuN ₄	1.409	-0.537	-0.237	Easy-release boundary with strongly unfavorable initial activation.

6 Original Manuscript Drafts Produced by CatMaster

This section archives the original manuscript artifacts produced within the CatMaster project workspaces, reproduced here as appended PDFs rather than summarized fragments. The source records come from the corresponding project `files/writing/` directories in the Pt(111), Cu(111) RWGS, and SAC case workspaces, so that the submission package preserves the raw draft-level outputs generated during each campaign.

6.1 Pt(111) CO-Oxidation Short Paper

The following pages reproduce the original CatMaster-written Pt(111) short paper from `Materials/project_space/Pt_111_CO/files/co_oxidation_pt111/writing/co_oxidation_pt111_short_paper.pdf`. The corresponding archived source file is `Materials/project_space/Pt_111_CO/files/co_oxidation_pt111/writing/co_oxidation_pt111_short_paper.tex`.

Dissociative O₂ Activation and Direct O* + CO* Oxidation on Pt(111) in a Fully MACE-mh-1 Reaction Network

Author Name

Department of Chemistry, Institution, City, Country

E-mail:

Abstract

Low-coverage CO oxidation on clean Pt(111) is often discussed in terms of dissociative oxygen activation followed by a Langmuir–Hinshelwood reaction between adsorbed O and CO, but the balance between terrace-level atomic and molecular branches depends on how broadly the reaction network is explored.^{1–5} Here, a compact reaction-network study was carried out using only the MACE-mh-1 potential on a Pt(111) $3 \times 3 \times 4$ slab with the bottom two layers fixed, without any DFT refinement. The accepted network identifies CO adsorption on top sites at -1.625 eV, molecular O₂ precursors near -0.720 eV, dissociated OO* at -1.731 eV, and weakly bound CO₂* at -0.051 eV relative to the corresponding gas-phase references. The accepted barriers are 0.412 eV for O diffusion, 0.952 eV for O₂ dissociation, and 1.129 eV for the direct oxidation event from the lower-energy CO* + O* basin to a bent CO₂*-like product complex. An explicit molecular O₂-assisted branch was constructed, but no robust accepted competitive barrier was recovered on the clean terrace. An approximate 400 K free-energy profile referenced to CO(g) + 0.5 O₂(g) + * gives a 1.114 eV barrier for the direct oxidation transition state, which remains the kinetic maximum of the

accepted route, while $\text{CO}_2(\text{g}) + *$ is strongly downhill thermodynamically. Within this low-coverage terrace model, MACE-mh-1 therefore recovers the canonical ranking in which dissociative O_2 activation feeds a lower-energy $\text{CO}^* + \text{O}^*$ basin and direct $\text{O}^* + \text{CO}^*$ oxidation defines the controlling barrier on Pt(111).

Introduction

CO oxidation on Pt(111) remains a useful benchmark for terrace-level heterogeneous catalysis because the system is simple enough for elementary-step analysis, yet rich enough to expose competition between adsorption, precursor-mediated oxygen activation, lateral arrangement effects, and product formation.¹⁻⁵ Early periodic DFT work established the importance of the local $\text{O}^* + \text{CO}^*$ reaction coordinate for CO_2 formation on clean Pt(111), while later studies emphasized that molecular O_2 -assisted channels can exist on Pt(111) under appropriate coadsorption conditions and that systematic route-network exploration is valuable for identifying nearby alternatives rather than assuming a single hand-built sequence.¹⁻³ At the same time, oxygen activation depends strongly on coverage and local topology, so terrace-only low-coverage models should be interpreted as mechanistic baselines rather than universal kinetic descriptions.^{4,5}

This short paper tests whether a fully MACE-mh-1-based exploration can yield a coherent main route for low-coverage CO oxidation on clean Pt(111) when no DFT calculations are introduced at any stage. The goal is to evaluate whether a compact literature-grounded network containing CO^* , O_2^* precursors, dissociated O pairs, $\text{CO}^* + \text{O}^*$ motifs, a direct CO_2 -forming step, and one explicit O_2 -assisted branch yields a coherent mechanistic ranking under strict no-DFT constraints. The study is restricted to clean Pt(111) at low coverage with terrace motifs only, MACE electronic energies throughout, and an approximate 400 K thermochemical correction only for the accepted direct route.

Methods

All quantitative energies and forces were obtained from MACE-mh-1 using the `omat_pbe` head with dispersion disabled. The surface model was a Pt(111) $3 \times 3 \times 4$ slab built from a MACE-relaxed fcc Pt bulk reference. The bottom two layers were fixed, leaving 18 of 36 Pt atoms mobile. This geometry corresponds to 1/9 ML single-adsorbate coverage for isolated species and provides the low-coverage clean-terrace setting used throughout the study.

The bounded network was assembled around the literature-grounded motifs most relevant to CO oxidation on Pt(111): clean slab, CO adsorption, O adsorption, molecular O₂ precursors, dissociated OO* states, coadsorbed CO* + O* configurations, an explicit CO* + O₂* entrance state, and CO₂-containing products.¹⁻⁵ Twenty-nine candidate states were relaxed, key minima were selected, and six nudged elastic band tasks were prepared to probe O diffusion, O₂ dissociation, direct CO oxidation, and a molecular O₂-assisted oxidation branch. In the discussion below, accepted states and steps are those that yielded converged relaxations or converged NEBs; provisional labels are retained for paths that were numerically consistent with accepted trends but remained slightly above the force threshold; unstable-not-accepted labels denote constructed branches that did not produce a robust physically credible barrier.

Approximate 400 K thermochemistry was evaluated only for the accepted main direct route. Gas-phase CO, O₂, and CO₂ were corrected at 400 K and 1 bar with ASE `IdealGasThermo` using the saved MACE finite-difference frequencies. Adsorbate-containing minima and the transition-state image were corrected with ASE `HarmonicThermo` using only the adsorbate vibrational modes, with slab atoms excluded; for the accepted route these active atoms are the adsorbate indices [36, 37, 38]. Before applying the harmonic correction, every retained positive adsorbate mode was subjected to a 50 cm⁻¹ low-frequency floor, and the single imaginary mode was removed only for the transition state. The resulting profile is therefore an approximate Gibbs/free-energy representation of the selected route rather than a full surface phonon treatment. No explicit CO₂ desorption barrier was computed.

Results and Discussion

Representative structures and literature-grounded network scope

Figure 1 collects the representative MACE-optimized structures that anchor the accepted terrace network: the lower-energy $\text{CO}^* + \text{O}^*$ reactant basin, the dissociated adjacent O^*O^* state reached after O_2 activation, and the direct oxidation transition state. Together with the Pt(111) $3 \times 3 \times 4$ slab definition given in the Methods section, these structures define the low-coverage terrace motifs carried into the accepted route analysis. Within this fixed setting, the network remains mechanistically inclusive: molecular oxygen adsorption and dissociation were retained because precursor-mediated O_2 activation is central to Pt(111) chemistry,^{1,4} the direct $\text{O}^* + \text{CO}^*$ route was retained because it is the canonical terrace-level CO_2 -forming step,^{1,3} and one explicit O_2 -assisted branch was retained because earlier Pt(111) studies showed that such channels can become relevant in coadsorbed environments even when they are not dominant under clean low-coverage conditions.²

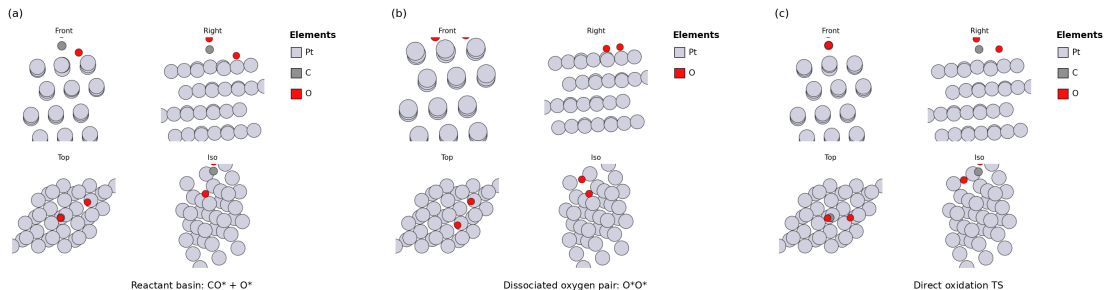


Figure 1: Key MACE-optimized structures for the accepted Pt(111) route/network: (a) the reactant $\text{CO}^* + \text{O}^*$ basin, (b) the dissociated O^*O^* state, and (c) the direct oxidation transition state. Each panel shows front, right, top, and isometric views of the corresponding terrace configuration.

The model is intended as a low-coverage terrace baseline rather than a full catalytic microkinetic treatment. No step or edge sites were introduced, no high-coverage CO-poisoned states were targeted, and no disordered oxygen domains were sampled. That limitation should be kept in mind when comparing the present numbers with the literature: Shan

and co-workers showed that O_2 dissociation becomes much less favorable as CO coverage increases,⁴ and Kinne and co-workers demonstrated that local oxygen topology strongly affects reactivity on Pt(111).⁵ Within that scope, the value of the present model is a reproducible low-coverage terrace baseline in which the accepted route and branch competition can be read directly from one internally consistent MACE potential.

Adsorption states and site-resolved minima

The key relaxed minima are summarized in Table 1. CO binds most strongly in the sampled single-adsorbate set as an atop species at -1.625 eV relative to $CO(g) + *$. Oxygen adsorption is more site-sensitive: the fcc hollow is the lowest accepted O^* minimum at -0.896 eV relative to $0.5 O_2(g) + *$, whereas the hcp hollow lies 0.249 eV higher. Molecular oxygen forms two nearly isoenergetic precursors, fcc-like and bridge-like, both near -0.720 eV relative to $O_2(g) + *$. These intact precursors sit more than 1 eV above the dissociated adjacent fcc/hcp OO^* state, which is stabilized to -1.731 eV and therefore supports dissociative activation as the preferred oxygen-entry picture within the accepted compact network.

Table 1: Compact summary of key adsorption and product-side minima from the accepted network. Energies are reported relative to the gas-phase reference listed in the third column.

State	Description	Reference	ΔE (eV)
CO^* atop minimum	C-down atop adsorption geometry	$CO(g) + *$	-1.625
O^* fcc hollow	Lowest oxygen adsorption minimum	$0.5 O_2(g) + *$	-0.896
O^* hcp hollow	Higher-energy oxygen hollow minimum	$0.5 O_2(g) + *$	-0.647
O_2^* fcc-like precursor	Molecular oxygen precursor	$O_2(g) + *$	-0.720
O_2^* bridge-like precursor	Bridge-like molecular oxygen precursor	$O_2(g) + *$	-0.719
Adjacent O^*O^* pair (fcc/hcp)	Lowest dissociated oxygen-pair state	$O_2(g) + *$	-1.731
CO_2^* flat bridge minimum	Weakly bound flat adsorbed CO_2	$CO_2(g) + *$	-0.051

The coadsorbed $CO^* + O^*$ minima also help explain later barrier trends. The lower-energy adjacent $CO^* + O^*$ basin lies at -2.562 eV relative to $CO(g) + 0.5 O_2(g) + *$ and serves as the accepted entrance state for the main Langmuir–Hinshelwood route; in the

machine-readable tables this state is labeled CO_0_hcp_adj. A higher-energy far-separated CO* + O* arrangement is 0.967 eV above that basin and appears as CO_0_fcc_far in the supporting data. On the product side, the bent CO₂*-like complex generated by the accepted direct oxidation path is slightly more stable than the main reactant basin, but the flat adsorbed CO₂* minimum binds only weakly relative to CO₂(g) + *. Together with the near-zero electronic energy of the far-desorbed CO₂ reference, this weak binding supports the interpretation that chemisorbed CO₂ is not a deep product well on the clean terrace.

Elementary-step barriers and branch competition

The accepted and nonaccepted step summaries are listed in Table 2 and visualized in Figure 2. Three accepted barriers define the compact mechanistic picture. First, O diffusion from fcc to hcp proceeds with a 0.412 eV barrier, confirming that local oxygen rearrangement is facile compared with bond-breaking chemistry. Second, O₂ dissociation from the bridge-like molecular precursor requires 0.952 eV and is exergonic by 1.011 eV, which places dissociative activation below the main direct oxidation event but still high enough to remain mechanistically meaningful. Third, the direct oxidation step from the lower-energy CO* + O* basin to the bent CO₂*-like product complex carries the largest accepted barrier, 1.129 eV, making it the kinetic maximum of the accepted terrace network.

Table 2: Elementary-step summary extracted from the machine-readable NEB and state analysis. The O₂-assisted branch was constructed but did not yield a robust accepted barrier.

Step	Initial state	Final state	ΔE_{rxn} (eV)	Barrier (eV)	Status
O diffusion fcc→hcp	O* fcc hollow	O* hcp hollow	0.249	0.412	Accepted
O ₂ dissociation from bridge precursor	O ₂ * bridge-like precursor	Adjacent O*O* pair	-1.011	0.952	Accepted
O ₂ dissociation from fcc precursor	O ₂ * fcc-like precursor	Adjacent O*O* pair	-1.011	0.952	Provisional
Direct CO oxidation from low-energy CO* + O* basin	Adjacent CO* + O* basin	Bent CO ₂ *-like product complex	-0.175	1.129	Accepted
Direct CO oxidation from higher-energy far-separated basin	Far-separated CO* + O* basin	Bent CO ₂ *-like product complex	-1.142	0.162	Accepted
Explicit O ₂ -assisted oxidation branch	CO* + O ₂ * entrance state	CO ₃ *-like bridge product	-1.836	—	Not accepted

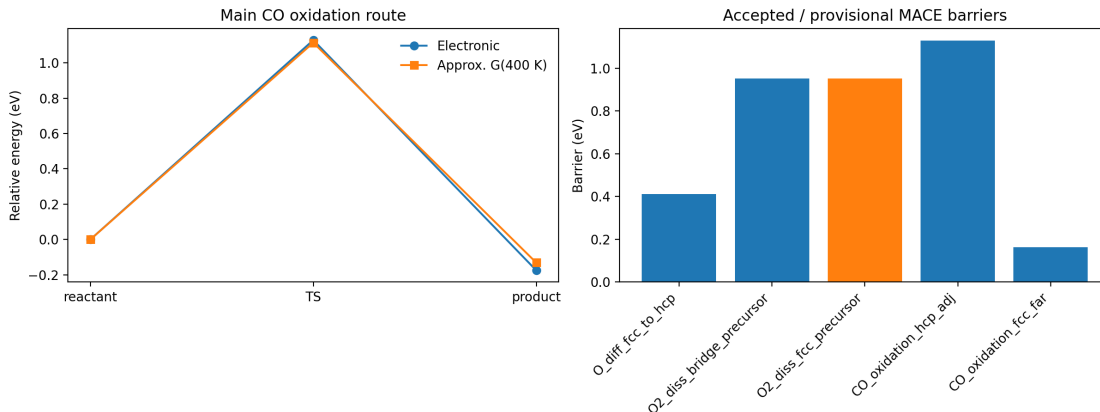


Figure 2: Summary of the Pt(111) CO oxidation network. The left panel provides a compact comparison between the accepted direct-route electronic profile and the corresponding approximate 400 K free-energy profile under the audited thermochemistry convention. The right panel collects accepted and provisional barrier heights for diffusion, O₂ dissociation, and direct CO oxidation steps.

The low 0.162 eV barrier found from the higher-energy far-separated CO* + O* basin does not overturn the main mechanistic assignment, because that entrance state is itself almost 1 eV above the lower-energy coadsorbed basin. The relevant kinetic competition is therefore not simply the local barrier from each basin, but the basin energy plus the local barrier. Once that distinction is made, the accepted direct oxidation event from the lower-energy adjacent CO* + O* state remains the controlling terrace-level step.

The explicit molecular O₂-assisted branch was evaluated but not retained as competitive. This branch was included because Eichler and Hafner showed that molecular pathways are mechanistically real on Pt(111), especially in coadsorbed environments.² In the present clean-terrace model, however, the O₂-assisted path did not yield a stable accepted barrier: the first pass suggested a sub-eV path without full convergence, whereas the refined restart diverged to an unphysical high barrier and large residual forces. Under the acceptance criteria used here, that behavior is insufficient to support a competitive molecular route on clean low-coverage Pt(111).

400 K Gibbs/free-energy profile of the accepted main route

The approximate 400 K free-energy profile for the accepted main route is shown in Figure 3 with the convention $\text{CO}(\text{g}) + 0.5 \text{O}_2(\text{g}) + * = 0$. Within this representation, the coadsorbed $\text{CO}^* + \text{O}^*$ basin lies at -1.518 eV , the direct oxidation transition state at -0.404 eV , and the bent CO_2^* -like product complex at -1.649 eV . The corresponding intrabasin free-energy barrier is 1.114 eV under the audited thermochemistry convention, slightly below the electronic barrier of 1.129 eV but still the highest accepted point along the route. The $\text{CO}_2(\text{g}) + *$ thermodynamic endpoint lies much lower, at -2.726 eV , showing that the overall oxidation event is strongly downhill even though the explicit desorption barrier from the bent product complex was not calculated.

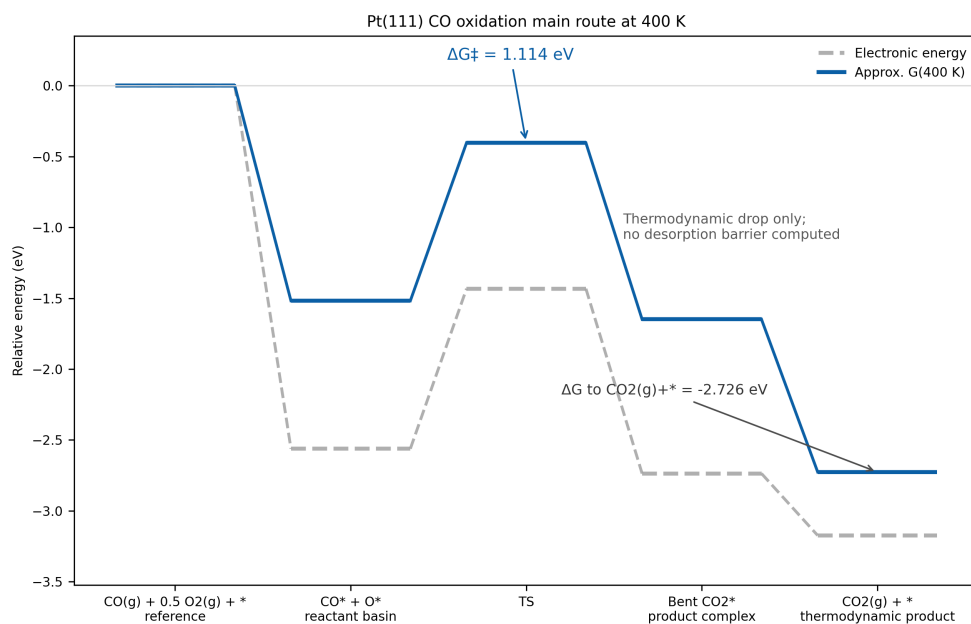


Figure 3: Approximate 400 K free-energy profile for the accepted direct CO oxidation route on Pt(111), referenced to $\text{CO}(\text{g}) + 0.5 \text{O}_2(\text{g}) + *$. Gas references use ASE `IdealGasThermo`, whereas adsorbate-containing states use adsorbate-only ASE `HarmonicThermo` with slab atoms excluded. The plotted endpoint at $\text{CO}_2(\text{g}) + *$ is thermodynamic only; no explicit CO_2 desorption barrier was computed in this study.

This free-energy profile should be interpreted with the approximations used to construct it. Gas-phase CO , O_2 , and CO_2 use ASE `IdealGasThermo` at 400 K and 1 bar. Adsorbate

minima and the transition state use ASE `HarmonicThermo` applied only to adsorbate-local modes with slab atoms excluded; for the accepted route the active atom indices are [36, 37, 38], the single imaginary mode is removed only for the transition state, and retained positive modes are floored to 50 cm^{-1} before correction. Because no retained positive adsorbate mode required flooring, the audited `HarmonicThermo` treatment leaves the resulting free-energy profile unchanged to practical precision. The qualitative message is therefore unchanged and internally consistent with the electronic network analysis: dissociative oxygen activation feeds a lower-energy $\text{CO}^* + \text{O}^*$ basin, the direct $\text{O}^* + \text{CO}^*$ transition state remains the kinetic maximum, and the final $\text{CO}_2(\text{g}) + *$ state is thermodynamically favored. In this sense, the 400 K correction refines the magnitude of the barrier without changing the accepted mechanistic ranking.

Conclusions

A reaction-network exploration performed entirely with MACE-mh-1 supports a coherent low-coverage picture of CO oxidation on clean Pt(111). Within the accepted compact network, molecular O_2 adsorbs in shallow precursor states, dissociates exergonically to a lower-energy OO^* pair, and ultimately feeds a Langmuir–Hinshelwood $\text{O}^* + \text{CO}^*$ oxidation event whose transition state is the highest accepted barrier both electronically and in the approximate 400 K free-energy profile. The explicit O_2 -assisted branch was mechanistically worth testing, but it was not retained as a robust competitive channel on the clean terrace. For the $3 \times 3 \times 4$ low-coverage Pt(111) slab studied here, MACE-mh-1 therefore recovers the canonical terrace-level ranking without DFT intervention: dissociative O_2 activation establishes the relevant $\text{CO}^* + \text{O}^*$ basin, and direct local CO_2 formation rather than oxygen diffusion or an accepted molecular branch defines the main route. No explicit CO_2 desorption barrier was included in this analysis.

References

- (1) Alavi, A.; Hu, P.; Deutsch, T.; Silvestrelli, P. L.; Hutter, J. CO Oxidation on Pt(111): An Ab Initio Density Functional Theory Study. *Physical Review Letters* **1998**, *80*, 3650–3653.
- (2) Eichler, A.; Hafner, J. Reaction channels for the catalytic oxidation of CO on Pt(111). *Physical Review B* **1999**, *59*, 5960–5967.
- (3) Sugiyama, K.; Sumiya, Y.; Takagi, M.; Saita, K.; Maeda, S. Understanding CO oxidation on the Pt(111) surface based on a reaction route network. *Physical Chemistry Chemical Physics* **2019**, *21*, 14366–14375.
- (4) Shan, B.; Kapur, N.; Hyun, J.; Wang, L.; Nicholas, J. B.; Cho, K. CO-Coverage-Dependent Oxygen Dissociation on Pt(111) Surface. *The Journal of Physical Chemistry C* **2009**, *113*, 710–715.
- (5) Kinne, M.; Fuhrmann-Lieker, T.; Zhu, J.; Whelan, C. M.; Denecke, R.; Steinrück, H.-P. Kinetics of the CO oxidation reaction on Pt(111) studied by in situ high-resolution x-ray photoelectron spectroscopy. *The Journal of Chemical Physics* **2004**, *120*, 7113–7122.

Supporting Information

Supporting information for this short paper should include the machine-readable final-state and elementary-step tables, the numerical 400 K main-route profile, and the bare-slab Pt(111) rendering used to define the terrace model. These materials provide the extended numerical context behind the compact main-text tables and figures.

6.2 Cu(111) RWGS Literature-Guided Short Paper

The following pages reproduce the original CatMaster-written literature-guided Cu(111) RWGS short paper from `Materials/project_space/Cu111_RWGS_Lit/files/writing/rwgs_cu111_short_paper.pdf`. The corresponding archived source file is `Materials/project_space/Cu111_RWGS_Lit/files/writing/rwgs_cu111_short_paper.tex`.

Formate Entry as the Only Quantitatively Accepted Elementary RWGS Step on Clean Cu(111) in a Strict MACE-Only Network Study

Author Name Placeholder

Affiliation Placeholder

Abstract

Reverse water-gas shift (RWGS) on copper is commonly discussed in terms of competing carboxyl, direct dissociation, and formate branches, with clean Cu(111) literature usually prioritizing carboxyl chemistry for CO formation while treating direct dissociation as disfavored and formate as a real but often sink-like competitor.[1–9] Here, an autonomous mechanism-discovery stage was used to translate that literature baseline into a geometry-aware elementary-step network for an ideal clean Cu(111) terrace, and the resulting network was then evaluated *de novo* using only MACE-mh-1+D. No DFT calculations were used. The executed model was a clean 4-layer 3×3 Cu(111) slab with 15 Å vacuum and the bottom two layers fixed. Final acceptance required float64 minima with forces ≤ 0.03 eV/Å and TS/NEB segments with forces ≤ 0.05 eV/Å, together with single-step path character. Under those criteria, the only quantitatively accepted elementary event was local formate entry, $\text{CO}_2^* + \text{H}^* \rightarrow \text{HCOO}^*$, with $E_a = 0.798390$ eV, $\Delta E = -0.238081$ eV, and $\Delta G^\ddagger(600\text{ K}) = 0.888528$ eV. The corresponding local-pair-to-HCOO* free-energy change at 600 K was +0.058987 eV. Alternative CO-forming branches were left unresolved rather than assigned surrogate barriers because no unconstrained local $\text{CO}^* + \text{OH}^*$ or $\text{CO}^* + \text{O}^*$ product minima survived and the best carboxyl/direct NEBs remained multi-step or high-force. The resulting conclusion is therefore a bounded disagreement with literature expectations on this specific clean-terrace MACE model, not a claim that carboxyl chemistry is absent on copper in reality.

1 Introduction

Mechanistic descriptions of RWGS on copper have long emphasized a competition between associative carboxyl chemistry, direct or redox CO_2 dissociation, and formate-centered alternatives. For clean Cu(111), the literature baseline used here is internally consistent in two important ways. First, it generally treats COOH^* formation and cleavage as the priority route to CO on the ideal terrace. Second, it places direct dissociation on Cu(111) in a higher-barrier, less favorable role while still recognizing it as a meaningful comparator, and it treats HCOO^* as a genuine Cu(111) adsorbate that can compete with CO-forming chemistry even if it is not usually identified as the dominant CO-forming route.[1–9]

That literature picture is mechanistically informative, but it does not by itself guarantee that every nominal branch can be validated as a single elementary step on one exact surface model under one exact level of theory. The present work addresses that gap with a strict from-scratch network study on ideal clean Cu(111). An autonomous literature-to-network stage first identified the branch families and converted them into geometry-aware, NEB-ready elementary hypotheses. A bounded MACE-mh-1+D campaign then evaluated those hypotheses on a single clean-terrace

model using explicit local endpoints and strict path-quality criteria. All quantitative results in this paper come from MACE-mh-1+D; no DFT calculations, imported DFT barriers, or surrogate kinetic assignments were used.

The main outcome is clear and deliberately bounded. Intact COOH* and HCOO* minima were both found on the clean terrace, but only the local formate-entry step passed the full acceptance criteria. Carboxyl formation, COOH* cleavage, direct/redox CO formation, and subsequent O*/OH* hydrogenation segments all remained unresolved on this model because the required local endpoints or valid single-step NEBs were not obtained. The paper therefore reports a defensible negative result: on this specific ideal Cu(111) model, only formate entry is quantitatively accepted.

2 Computational protocol and autonomous mechanism-discovery workflow

The surface model was a clean four-layer 3×3 Cu(111) slab with 15 Å vacuum and the bottom two layers fixed. All production acceptance decisions were based on MACE-mh-1+D. Float32 calculations were used only for inexpensive triage or endpoint screening, whereas final state and barrier judgments were made from float64 results. Minima were accepted only when the maximum force was ≤ 0.03 eV/Å, and transition-state or NEB segments were accepted only when the maximum force was ≤ 0.05 eV/Å. In addition to those force criteria, a path had to remain a single local chemical event. Bands that mixed bond making or breaking with terrace diffusion, long-range reorientation, or multiple substeps were rejected even if they suggested chemically plausible motifs.

The autonomous mechanism-discovery stage was designed to produce a simulation-ready clean-Cu(111) baseline rather than an exhaustive catalytic ontology. Literature-derived mechanism families were mapped into explicit elementary steps with local endpoint requirements. This procedure retained three baseline families for the clean terrace: a carboxyl branch, $\text{CO}_2^* + \text{H}^* \rightarrow \text{COOH}^* \rightarrow \text{CO}^* + \text{OH}^*$; a direct/redox comparator, $\text{CO}_2^* \rightarrow \text{CO}^* + \text{O}^*$ followed by oxygen removal; and a formate branch, $\text{CO}_2^* + \text{H}^* \rightarrow \text{HCOO}^*$.^[1–9] Water-assisted, oxide-assisted, step-assisted, or reconstruction-dependent variants were intentionally excluded from the baseline because the executed model contains none of those ingredients.

A key protocol consequence is that nominal chemistry was not accepted by formula alone. Each branch required an actual local reactant state, an actual local product state, and a geometry-consistent single-step pathway connecting them. If a local product minimum relaxed into a separated coadsorbate, reclosed to the parent intermediate, or collapsed into a different precursor class, that branch was left unresolved. Likewise, if an NEB developed multiple maxima or high-force images that signaled more than one subevent, the branch was not assigned a surrogate barrier. This strict protocol is central to the interpretation of the negative result reported below.

3 Discovered RWGS mechanisms on clean Cu(111)

The autonomous discovery stage recovered the same hierarchy that dominates the clean-Cu(111) literature. Carboxyl chemistry emerged as the literature-priority associative family, direct dissociation remained the standard higher-barrier comparator, and formate remained a required competing branch because HCOO* is experimentally and computationally well established on Cu(111).^[1–11] That ranking defined the initial network hypotheses, but the present work did not assume that literature priority would translate automatically into accepted elementary steps on the chosen model.

The resulting branch map for the clean terrace is summarized in Table 1. The important distinction is between literature-supported mechanistic expectation and present-work validation

status. In that sense, the network contains both positive and negative information: some species are real local minima on this model, but not every nominal reaction between them survives the single-step QC required for quantitative use.

Table 1: RWGS branch map retained for clean Cu(111) and its validation status on the executed MACE-only model.

Branch family	Literature expectation on clean Cu(111)	Present MACE-only status on the executed model
Carboxyl ($\text{CO}_2^* + \text{H}^* \rightarrow \text{COOH}^* \rightarrow \text{CO}^* + \text{OH}^*$)	Priority associative route to CO; often preferred over formate.[1, 2, 6, 7]	COOH^* exists as an intact minimum, but formation remained an invalid multi-step/high-force NEB and no local $\text{CO}^* + \text{OH}^*$ cleavage product minimum survived.
Direct/redox ($\text{CO}_2^* \rightarrow \text{CO}^* + \text{O}^*$)	Real comparator but usually disfavored on ideal terraces.[3, 4, 8, 9]	No validated local $\text{CO}^* + \text{O}^*$ product minimum survived; only OCO-like precursor states were retained, and the precursor NEB was invalid.
Formate ($\text{CO}_2^* + \text{H}^* \rightarrow \text{HCOO}^*$)	Real competing branch or sink; usually not the favored route to CO.[1, 5-7, 10, 11]	The only quantitatively accepted elementary step, with an accepted local H-transfer barrier and 600 K free-energy segment.

4 MACE reaction-network results on Cu(111)

The accepted state inventory on clean Cu(111) includes the clean slab, H^* , O^* , OH^* , weak CO_2^* capture states, H_2O^* , one intact COOH^* motif, and bidentate HCOO^* motifs, together with separated coadsorbate references such as $\text{CO}_2^* + \text{H}^*$, $\text{CO}^* + \text{OH}^*$, $\text{O}^* + \text{H}^*$, and $\text{OH}^* + \text{H}^*$. This inventory is already informative. It shows that the MACE-only model does not erase oxygenated chemistry wholesale: both COOH^* and HCOO^* exist as local minima on the clean terrace. The decisive question is instead whether the corresponding elementary steps can be validated under the strict local single-step protocol.

Only one step satisfied that standard. The accepted float64 CI-NEB for $\text{CO}_2^* + \text{H}^* \rightarrow \text{HCOO}^*$ connects a validated local $\text{CO}_2^* + \text{H}^*$ pair to a local bidentate formate endpoint and gives $E_a = 0.798390$ eV and $\Delta E = -0.238081$ eV. The maximum NEB force was 0.049562 eV/Å, which satisfies the ≤ 0.05 eV/Å acceptance criterion, and the path-quality checks support a single local H-transfer event rather than a hidden diffusion sequence. Within the present bounded network, this is the only quantitatively accepted elementary RWGS step.

The carboxyl branch remained unresolved for two distinct reasons. For $\text{CO}_2^* + \text{H}^* \rightarrow \text{COOH}^*$, repaired local endpoints could be obtained, including a local hcp-side $\text{CO}_2^* + \text{H}^*$ reactant and an intact bridge-leaning COOH endpoint. However, the best float64 NEB still produced a two-maxima profile with barrier 0.861458 eV, reaction energy $+0.443938$ eV, and maximum force 0.184556 eV/Å. COOH formation was already achieved partway through the band, and a second OH reorientation substep followed before the endpoint. Because this band was neither low-force nor single-step, it was rejected as a quantitative carboxyl-formation barrier. For COOH^* cleavage, explicit local $\text{CO}^* + \text{OH}^*$ product seeds relaxed either to separated $\text{CO}^* + \text{OH}^*$ minima with C-to-OH distances

of about 3.35–3.51 Å or back to intact COOH*. No unconstrained local CO* + OH* product minimum survived, so a cleavage NEB would not have represented a validated elementary event.

The direct/redox branch remained still more incomplete. Explicit local CO* + O* product seeds collapsed into bent OCO-like precursor states rather than a distinct local CO* + O* minimum, and dedicated activated-CO₂ precursor seeds flattened back toward capture-state-like CO₂*. The lowest retained precursor was therefore only a precursor, not an accepted CO-forming product state. A float64 NEB from flat CO₂* to that precursor gave an attempted barrier of 1.213421 eV with maximum force 0.300311 eV/Å and obvious multi-step character involving O ejection. That result strengthens the exclusion of a validated direct/redox step on this model but does not justify quantitative reporting of the precursor as successful CO₂ dissociation.

The same logic governed the downstream oxygen-removal segments. Local O* + H* seeds collapsed directly to OH*, and close OH* + H* seeds either collapsed to H₂O* or relaxed back to separated OH* + H*. Because no validated local prereactive minima existed for those segments, no surrogate hydrogenation barriers were assigned. This was an intentional feature of the protocol, not missing bookkeeping: unresolved branches were left unresolved precisely to avoid converting endpoint instability into false kinetic completeness.

5 600 K free-energy analysis

Because only the formate-entry step was accepted electronically, the 600 K thermochemical analysis was intentionally restricted to that same local segment. The free-energy reference was clean Cu(111) + CO₂(g) + $\frac{1}{2}$ H₂(g), using adsorbate-only harmonic corrections with a 50 cm⁻¹ floor for adsorbates, ideal-gas corrections for CO₂ and H₂ at 600 K and 1 atm, and omission of one imaginary mode for the transition state. Under that convention, the separated CO₂* + H* minimum lies at 0.579231 eV, the validated local CO₂* + H* pair at 0.595635 eV, the transition state at 1.484162 eV, and the aligned local HCOO* endpoint at 0.654621 eV relative to the gas-phase reference.

The resulting kinetic and thermodynamic quantities remain modest but unambiguous. The accepted local formate-entry segment has $\Delta G^\ddagger(600\text{ K}) = 0.888528\text{ eV}$ and local-pair-to-HCOO* $\Delta G(600\text{ K}) = +0.058987\text{ eV}$. Thus, the only profiled step is electronically exothermic but slightly uphill in free energy at 600 K when referenced to the validated local reactant pair. Figure 1 shows this accepted free-energy segment. It does not attempt to extend the profile onto carboxyl or direct/redox CO-forming branches, because those branches were not converged as accepted local elementary steps. Appendix A tabulates the full NEB optimization-trial record, the network-relevant endpoint relaxations, and the 600 K bookkeeping retained for this bounded network.

6 Comparative discussion versus literature

The clearest comparison with prior work is not that the present study reverses the literature ranking in favor of formate as the dominant RWGS route to CO. That stronger claim is not supported. Instead, the present result is a bounded disagreement between literature-level mechanistic priority and model-level elementary-step validation. The literature baseline for clean Cu(111) still points first to carboxyl chemistry, treats direct dissociation as a disfavored but relevant comparator, and recognizes formate as a real competing branch or sink.[1–11] On the present ideal clean terrace, however, only formate entry satisfies the combined requirements of local endpoint stability, acceptable forces, and single-step path character.

This distinction matters because the negative result is informative only if it is stated precisely. The MACE-only network does not show that carboxyl chemistry is absent on copper, nor does it

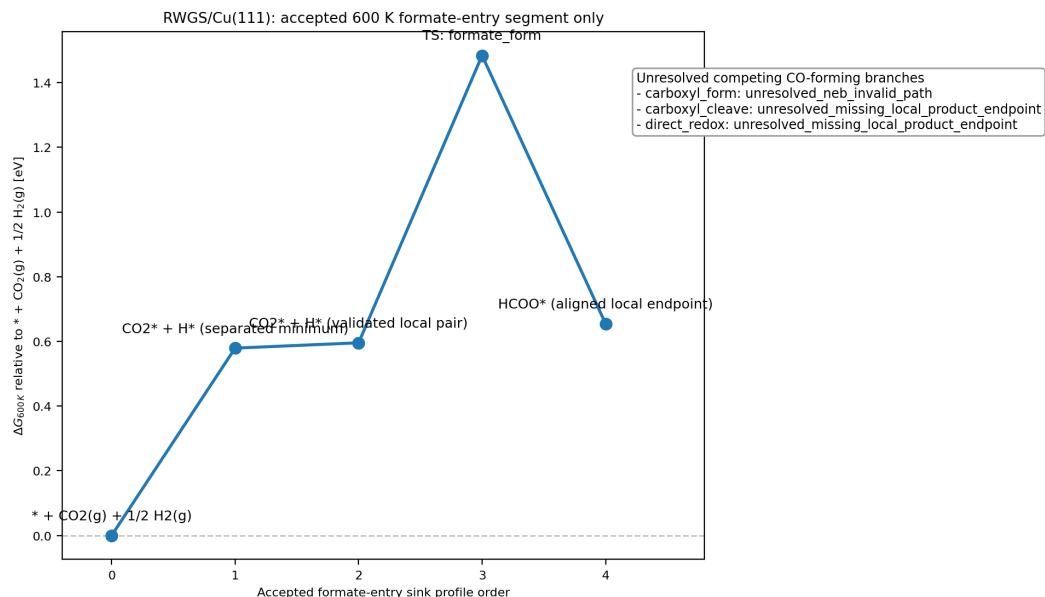


Figure 1: 600 K Gibbs free-energy profile for the accepted formate-entry segment on clean Cu(111). The profile is intentionally limited to the validated local $\text{CO}_2^* + \text{H}^* \rightarrow \text{HCOO}^*$ pathway because competing CO-forming branches were not converged.

prove that formate controls RWGS under all Cu(111) conditions. What it shows is narrower and more defensible: on a clean four-layer 3×3 Cu(111) terrace treated exclusively with MACE-mh-1+D and strict geometry-aware QC, literature-priority CO-forming branches could not be validated as quantitative single-step events. Intact COOH^* was stable as a minimum, yet neither its formation nor its cleavage passed the criteria needed for kinetic use. Likewise, direct/redox chemistry produced only precursor-like OCO states rather than a validated local $\text{CO}^* + \text{O}^*$ product.

The decision to leave those branches unresolved rather than to backfill them with estimated barriers is therefore essential to the scientific interpretation. Surrogate values would have implied a completeness that the present calculations did not earn. In a network study framed around autonomous mechanism discovery and strict single-step validation, the absence of an accepted local elementary step is itself a result. The correct mechanistic message is consequently not that formate is globally preferred over carboxyl on Cu(111), but that formate entry is the only branch that remains quantitatively defensible under this exact clean-terrace MACE protocol.

7 Conclusions

A strict from-scratch, geometry-aware MACE-only RWGS network study was carried out on clean 4-layer 3×3 Cu(111). Autonomous mechanism discovery recovered the literature baseline in which carboxyl chemistry is prioritized on clean Cu(111), direct dissociation serves as a disfavored comparator, and formate is a genuine competing branch. When those branch families were tested *de novo* with MACE-mh-1+D, float64 endpoint validation, and single-step NEB criteria, only one elementary event was accepted quantitatively: $\text{CO}_2^* + \text{H}^* \rightarrow \text{HCOO}^*$ with $E_a = 0.798390$ eV, $\Delta E = -0.238081$ eV, and $\Delta G^\ddagger(600 \text{ K}) = 0.888528$ eV. The corresponding local-pair-to-HCOO* free-energy change is +0.058987 eV.

All alternative CO-forming branches remained unresolved on this clean-terrace model. The best carboxyl-formation NEB was multi-step and high-force, no unconstrained local $\text{CO}^* + \text{OH}^*$ cleavage product minimum survived, and no local $\text{CO}^* + \text{O}^*$ product minimum survived beyond precursor-like OCO states. The resulting conclusion is therefore a bounded negative result: on ideal clean Cu(111) under the present MACE-mh-1+D protocol, local formate entry is the only quantitatively accepted RWGS elementary step, whereas literature-priority carboxyl and direct/redox CO-forming branches remain unresolved rather than disproven.

References

- [1] Amit A. Gokhale, James A. Dumesic, and Manos Mavrikakis. On the mechanism of low-temperature water gas shift reaction on copper. *Journal of the American Chemical Society*, 2008. doi: 10.1021/ja0768237.
- [2] Qian-Lin Tang, Zhao-Xu Chen, and Xiang He. A theoretical study of the water gas shift reaction mechanism on cu(111) model system. *Surface Science*, 2009. doi: 10.1016/j.susc.2009.04.011.
- [3] Fahdzi Muttaqien, Yuji Hamamoto, Kouji Inagaki, and Yoshitada Morikawa. Dissociative adsorption of CO_2 on flat, stepped, and kinked cu surfaces. *The Journal of Chemical Physics*, 2014. doi: 10.1063/1.4887362.
- [4] Baran Eren, Robert S. Weatherup, Nikos Liakakos, Gabor A. Somorjai, and Miquel Salmeron. Dissociative carbon dioxide adsorption and morphological changes on cu(100) and cu(111) at ambient pressures. *Journal of the American Chemical Society*, 2016. doi: 10.1021/jacs.6b04039.
- [5] Yinjuan Ren, Kaidi Yuan, Xiong Zhou, Haicheng Sun, Kai Wu, Steven L. Bernasek, Wei Chen, and Guo Qin Xu. Catalytic intermediates of CO_2 hydrogenation on cu(111) probed by in operando near-ambient pressure technique. *Chemistry - A European Journal*, 2018. doi: 10.1002/chem.201802931.
- [6] Lang Xu, Joshua Lin, Yunhai Bai, and Manos Mavrikakis. Atomic and molecular adsorption on cu(111). *Topics in Catalysis*, 2018. doi: 10.1007/s11244-018-0943-0.
- [7] Ya-Fan Zhao, Yong Yang, Charles A. Mims, Charles H. F. Peden, Jun Li, and Donghai Mei. Insight into methanol synthesis from CO_2 hydrogenation on cu(111): Complex reaction network and the effects of H_2O . *Journal of Catalysis*, 2011. doi: 10.1016/j.jcat.2011.04.012.
- [8] Gui-Chang Wang, Ling Jiang, Xian-Yong Pang, Zunsheng Cai, Yinming Pan, Xuezhuan Zhao, Yoshitada Morikawa, and Junji Nakamura. A theoretical study of surface-structural sensitivity of the reverse water-gas shift reaction over cu(hkl) surfaces. *Surface Science*, 2003. doi: 10.1016/S0039-6028(03)00876-8.
- [9] Gui-Chang Wang and Junji Nakamura. Structure sensitivity for forward and reverse water-gas shift reactions on copper surfaces: A dft study. *The Journal of Physical Chemistry Letters*, 2010. doi: 10.1021/jz101150w.
- [10] Isao Nakamura, H. Nakano, Tadahiro Fujitani, T. Uchijima, and Junji Nakamura. Synthesis and decomposition of formate on cu(111) and cu(110) surfaces: Structure sensitivity. *Journal of Vacuum Science & Technology A: Vacuum, Surfaces, and Films*, 1999. doi: 10.1116/1.581856.

- [11] A. Sotiropoulos, P. K. Milligan, Bruce C. C. Cowie, and Malcolm Kadodwala. A structural study of formate on cu(111). *Surface Science*, 2000. doi: 10.1016/S0039-6028(99)01050-X.

Appendix A. NEB trial record and thermochemical bookkeeping

Appendix A exposes the trial-level NEB record, the network-relevant relaxed state inventory, and the 600 K bookkeeping used for the bounded RWGS network on clean Cu(111).

A1. NEB optimization trials attempted for the constructed network

Table 2: NEB optimization trials retained for the constructed RWGS network on clean Cu(111).

Reaction / branch	Attempt label	Local endpoints (initial → final)	Accepted?	Final max force (eV/Å)	Barrier (eV) QC / raw	Reaction energy (eV)	QC note
$\text{CO}_2 + \text{H}^* \rightarrow \text{HCOO}^-$	Plain_relaxed/ formate_form (parent band)	C02_H_local_bridge → HC00_bidentate	Rejected	0.096414	0.712415 0.476494	-0.238081	Earlier 7-image plain-band formate trial from the canonical artifact root; unconverged and above the 0.05 eV/Å acceptance threshold.
$\text{CO}_2 + \text{H}^* \rightarrow \text{HCOO}^-$	img_plain_con tinuation	C02_H_local_bridge → HC00_bidentate	Rejected	0.224684	0.712659 0.476550	-0.238081	Continued plain-band formate attempt; lower barrier estimate was not accepted because the band remained high-force.
$\text{CO}_2 + \text{H}^* \rightarrow \text{HCOO}^-$	img_plain	C02_H_local_bridge → HC00_bidentate	Rejected	0.324868	0.719039 0.443035	-0.238081	Coarser plain-band formate attempt; retained only as a rejected trial because the force remained well above the acceptance threshold.
$\text{CO}_2 + \text{H}^* \rightarrow \text{HCOO}^-$	img_plain_rot ated_formate	C02_H_local_bridge → HC00_rotated	Rejected	0.535880	0.922056 0.644887	-0.237450	Rotated-formate endpoint variant; high-force path and higher-energy endpoint were not retained quantitatively.
$\text{CO}_2 + \text{H}^* \rightarrow \text{HCOO}^-$	img_ci_from_b est_plain	C02_H_local_bridge → HC00_bidentate	Accepted	0.049562	0.798390 0.798390	-0.238081	Accepted float64 CI-NEB; QC supports a single local H-transfer event without a separate terrace-diffusion substep.
$\text{CO}_2 + \text{H}^* \rightarrow \text{COOH}$	Plain_relaxed/ carboxyl_form (original attempt)	C02_H_local_variant_hcp → COOH_intact	Rejected	0.354928	6.838527 5.072906	+0.454791	Earlier plain-band carboxyl trial remained grossly unconverged and far above the force criterion; the repaired-endpoint follow-up retry below became the decisive carboxyl test.

6

Reaction / branch	Attempt label	Local endpoints (initial → final)	Accepted?	Final max (eV) / raw	Barrier (eV) (eV) / raw	Reaction energy (eV)	note
$\text{CO}_2 + \text{H}^* \rightarrow \text{COOH}$	8img_plain_idp p_hcp_to_bridg elean_cooH	C02_H_local_variant_hcp → C00H_intact	Rejected	0.184556	0.861458 0.596883	+0.443938	Follow-up carboxyl-formation retry remained invalid because the profile showed two maxima, with COOH formed mid-band and a later OH reorientation substep.
$\text{CO}_2 \rightarrow$ activated OCO-like precursor	8img_plain_idp p_flat_C02_to_ best_precursor	C02_capture_top → Best activated OCO-like precursor (not a validated CO* + O* minimum)	Rejected	0.300311	1.213421 0.866740	+0.671012	Precursor-approach NEB remained invalid: O ejection and multistep/nonphysical character prevented use as a direct/redox barrier.

Branches excluded before any validated NEB are listed separately below so that missing endpoints are explicit rather than folded into artificial trial rows.

Table 3: Constructed branches excluded before any validated NEB because required local endpoints were not retained.

Branch without NEB trial	Missing validated endpoint	Basis for exclusion
$\text{COOH}^* \rightarrow \text{CO}^* + \text{OH}^*$	No unconstrained local $\text{CO}^* + \text{OH}^*$ product minimum	Four float64 product seeds relaxed to separated $\text{CO}^* + \text{OH}^*$ (C-to-OH about 3.35–3.51 Å), and one bridge-like seed reclosed to intact COOH^* .
$\text{CO}_2^* \rightarrow \text{CO}^* + \text{O}^*$ (true product state)	No distinct local $\text{CO}^* + \text{O}^*$ product minimum	Explicit $\text{CO}^* + \text{O}^*$ seeds collapsed into bent OCO-like precursor states; only the precursor-approach NEB listed above was attempted.
$\text{O}^* + \text{H}^* \rightarrow \text{OH}^*$	No distinct local $\text{O}^* + \text{H}^*$ reactant minimum	All local $\text{O}^* + \text{H}^*$ repair seeds collapsed directly to OH^* during unconstrained relaxation.
$\text{OH}^* + \text{H}^* \rightarrow \text{H}_2\text{O}^*$	No stable local $\text{OH}^* + \text{H}^*$ prereactive minimum	Close $\text{OH}^* + \text{H}^*$ seeds either collapsed to H_2O^* or relaxed back to separated $\text{OH}^* + \text{H}^*$.

A2. Endpoint relaxations retained for the constructed network

Table 4: Endpoint relaxations retained for the bounded RWGS network on clean Cu(111).

State label	Motif	Energy (eV)	Max force (eV/Å)	Status	Role in the network / appendix
*	clean Cu(111) 4L 3×3; bottom 2 layers fixed	-142.303384	0.018452	accepted	Clean-slab reference used throughout the bounded network and in the 600 K reference definition.
H*	hollow-like terrace H	-145.995323	0.017518	accepted	Adsorbed H reference needed to interpret local CO ₂ * + H* pairing and the unresolved O*/OH* hydrogenation branches.
CO ₂ * (top capture)	weak flat physisorbed/top-like CO ₂ capture state	-165.419899	0.018546	accepted	Flat CO ₂ capture reference and starting point for the rejected direct/precursor NEB.
CO ₂ * (hcp capture)	weak flat physisorbed/hcp-like CO ₂ capture state	-165.421776	0.019055	metastable	Near-degenerate alternative CO ₂ capture motif retained as part of the adsorption landscape.
CO ₂ * + H* (separated minimum)	separated neighboring CO ₂ + H coadsorbate	-169.119353	0.019498	accepted	Separated coadsorbate reference; the accepted formate NEB instead starts from a repaired local CO ₂ _H_local_bridge endpoint documented in A1/A3 rather than as a separate state-inventory row.
COOH*	intact HOCO / top-cis-like carboxyl	-168.646738	0.017853	accepted	Only intact carboxyl minimum retained; parent state for the unresolved cleavage branch, while the bridge-leaning repaired NEB endpoint is tracked in A1 rather than as a separate inventory row.
HCOO*	bidentate formate	-169.342896	0.019038	accepted	Stable formate sink/product minimum; the accepted NEB used an aligned local endpoint at -169.339199 eV, slightly above this inventory minimum, as listed in A1/A3.
HCOO* (rotated)	rotated bidentate formate metastable	-169.245650	0.017225	metastable	Alternative formate endpoint tested in the rejected rotated-formate NEB.
CO*	bridge/hollow-like C-down CO minimum	-158.120164	0.012075	accepted	Lowest CO minimum retained for product-side comparison after unresolved CO-forming branches.
CO* (atop)	atop C-down CO metastable	-157.989304	0.019745	metastable	Metastable CO motif used when seeding local COOH-cleavage and direct/redox product searches.

State label	Motif	Energy (eV)	Max force (eV/Å)	Status	Role in the network / appendix
O*	hollow-like terrace O	-148.930730	0.012491	accepted	Oxygen reference for the unresolved direct/redox and O* hydrogenation bookkeeping.
OH*	hollow-like OH	-153.182634	0.013932	accepted	Hydroxyl product minimum retained after local O* + H* seeds collapsed during repair.
H ₂ O*	molecular H ₂ O atop/flat	-156.903720	0.018534	accepted	Water product minimum retained after local OH* + H* seeds collapsed or separated.
CO* + OH* (separated)	separated CO + OH coadsorbate	-168.921490	0.019985	accepted	Product-side reference only; local cleavage products relaxed to this separated class rather than surviving as a local reactive pair.
O* + H* (separated)	diffusion-separated O + H coadsorbate	-152.635691	0.016396	accepted	Diffusion-separated reference; not a validated local prereactive pair for O* hydrogenation.
OH* + H* (separated)	separated OH + H coadsorbate	-156.818992	0.011573	accepted	Diffusion-separated reference; not a validated local prereactive pair for OH* hydrogenation.

A3. 600 K corrections retained for the bounded network

Table 5: 600 K free-energy bookkeeping retained for the accepted bounded network.

State / step label	Electronic energy (eV)	Free-energy correction (eV)	G at 600 K (eV)	Relative G at 600 K (eV)	Status	Note
* + CO ₂ (g) + $\frac{1}{2}$ H ₂ (g)	-168.578274	-1.225187	-169.803462	0.000000	reference_defined	Reference state used for the accepted formate-entry free-energy segment at 600 K and 1 atm.
CO ₂ + H* (separated minimum)	-169.119353	-0.104877	-169.224231	0.579231	accepted	Accepted separated coadsorbate minimum under the adsorbate-only harmonic convention.
CO ₂ + H* (validated local pair)	-169.101118	-0.106709	-169.207827	0.595635	accepted_local_repair	Validated local endpoint used for the accepted NEB; 0.018236 eV above the separated minimum on the electronic surface.
TS: formate_form	-168.302728	-0.016572	-168.319299	1.484162	accepted_neb_ci	Highest-energy image from the accepted CI-NEB after dropping one imaginary mode from the harmonic sum.
HCOO* (aligned local endpoint)	-169.339199	+0.190359	-169.148840	0.654621	accepted_neb_endpoint	Product endpoint from the accepted formate NEB; 0.003697 eV above the separate HCOO* inventory minimum.
carboxyl_form	—	—	—	—	unresolved_neb_invalid_path/not_profiled	Not profiled at 600 K because the carboxyl-formation branch did not yield an accepted single-step NEB.
carboxyl_cleave	—	—	—	—	unresolved_mis싱_local_product_endpoint/not_profiled	Not profiled at 600 K because no validated local CO* + OH* product endpoint survived.
direct_redox	—	—	—	—	unresolved_mis싱_local_product_endpoint/not_profiled	Not profiled at 600 K because no validated local CO* + O* product endpoint survived; only precursor-like states were retained.

15

6.3 Cu(111) RWGS Autonomous-Exploration Short Paper

The following pages reproduce the original CatMaster-written autonomous Cu(111) RWGS short paper from `Materials/project_space/Cu111_RWGS_NewHint_a/files/writing/rwgs_cu111_autonomous_short_paper.pdf`. The corresponding archived source file is `Materials/project_space/Cu111_RWGS_NewHint_a/files/writing/rwgs_cu111_autonomous_short_paper.tex`.

A 41-Minimum, Partially Continuous RWGS Network on Cu(111) from Autonomous MACE Exploration

Abstract

A formal execution-facing account is now possible for a completed MACE-only reverse water-gas shift (RWGS) campaign on clean Cu(111). Starting from literature-unseeded low-coverage $C_1O_2H_2$ state enumeration on a four-layer 3×3 Cu(111) slab, the workflow combined relaxation, deduplication, connectivity-aware endpoint repair, short plain-NEB probing, hidden-state extraction, relaxation-based localization, geometry-safe decomposition, and seeded tightening to assemble an auditable reaction network under a single MACE protocol. The final low-coverage network contains 41 unique relaxed minima spanning $CHO_2^* + H^*$, $CH_2O_2^*$, $CHO^* + HO^*$, $CO^* + H^* + HO^*$, and $CO^* + H_2O^*$ regions. Accepted segments support local start-side dissociation, CHO_2 entry, CH_2O_2 same-basin relaxation, localized cleavage into $CHO^* + HO^*$, split-basin entry, strict split-basin handoff closure, and product closure. After exhaustive recursive probing across four named continuity gaps, the network remains partially continuous but still globally discontinuous: only gap 4 closed strictly, whereas gaps 1–3 remained unresolved because their best candidates were high-force, plateau-like, or placeholder-dependent under the final rule. The campaign therefore supports chemically meaningful RWGS network motifs on Cu(111) while also exposing MACE NEB high-force sticking and incomplete convergence as observed limitations that required corrective localization and tightening rather than direct mechanistic overclaim.

1 Introduction

Clean Cu(111) is a stringent baseline for RWGS network construction because terrace hydrogen activation is difficult and even ideal Cu facets can sustain competing oxygenated hydrogenation pathways rather than a single trivial route [Sakong and Groß \[2003\]](#), [Cao et al. \[2018\]](#), [Zhao et al. \[2011\]](#), [Grabow and Mavrikakis \[2011\]](#). The central scientific question is therefore which low-coverage minima and chemistry-changing connections remain defensible when the network is built without literature seeding and evaluated under one uniform class-and-force rule.

That perspective matters for Cu(111), where formate-like, carboxyl-related, and CO/OH/ H_2O motifs are all chemically relevant reference points in the broader Cu surface literature [Grabow and Mavrikakis \[2011\]](#), [Takeyasu et al. \[2022\]](#), [Li et al. \[2022\]](#). The present network is therefore informative not only for the accepted motifs it contains, but also for the chemically specific discontinuities that remain unresolved after systematic continuity testing. Accepted local motifs were retained, failed and high-force NEB attempts were preserved in the audit trail, and recursive continuity-gap closure was pursued explicitly rather than inferred from suggestive but noncompliant paths.

The resulting picture is scientifically useful precisely because it remains incomplete in a controlled way. Autonomous exploration discovers a nontrivial 41-minimum low-coverage network containing a $CHO_2^* + H^*$ basin and a downstream $CH_2O_2/CHO^* + HO^*/CO^* + H^* + HO^*/CO^* + H_2O^*$ packet, but exhaustive recursive closure does not merge those packets into a fully continuous mechanism. The final Cu(111) network must therefore be reported as partially continuous and still globally discontinuous after exhaustive recursive probing.

2 Methods

All calculations used a clean Cu(111) terrace represented as a four-layer 3×3 slab with 15 Å vacuum and the bottom two layers fixed. The explored composition space was low-coverage $C_1O_2H_2$ chemistry relevant to RWGS-like Cu(111) reactivity. Relaxations, frequencies, and NEB-based path searches were carried out within a MACE-only workflow using MACE-mh-1 with dispersion for the reported electronic energies, with float64 used for the reported campaign energetics and NEB analyses.

The network was initiated from literature-unseeded graph-based state enumeration rather than from a curated RWGS mechanism. Relaxed structures were deduplicated into unique nodes after connectivity reassignment, so node identity followed post-relaxation bonding and adsorption character rather than only the nominal input state. In the completed campaign, autonomous discovery and enrichment expanded the Cu(111) network to 41 unique relaxed minima.

Endpoint construction was made connectivity-aware whenever relaxed images indicated gas-like excursions, local-equivalent relays, or endpoint mismatch. Candidate endpoint images were reclassified by fragment connectivity and adsorption state, mapped onto stable nodes or explicitly labeled pseudo-states when they were local-equivalent shoulders rather than promoted minima, and repaired when a chemically local endpoint pair could be defined more cleanly than the original long-range band.

Path search was deliberately layered. Short plain-NEB probes first tested the nearest chemically plausible endpoint pairs. When a probe revealed an interior image with distinct connectivity or a local-equivalent shoulder, that image was extracted as a hidden or pseudo-state and then relaxed or reused as a localized endpoint candidate. Longer unresolved probes were decomposed into shorter segments when the bonding pattern suggested that only part of the path was chemically interpretable. Promising low-force local chains were then tightened by reseeding stable-to-stable NEB bands. This corrective workflow was motivated by a recurring campaign limitation: MACE NEBs on the present Cu(111) RWGS problem often stuck in high-force regions, broad shoulders, or plateau-like profiles even when the underlying chemistry suggested a local rearrangement worth isolating.

Accepted chemistry-changing segments were filtered conservatively. A relaxed local minimum had to satisfy a $0.03\text{ eV}/\text{Å}$ force criterion. For the strict recursive closure campaign, a continuity gap counted as closed only when the final connector remained in-family, belonged to an allowed accepted class (*primitive*, *primitive_localized_single_shoulder*, *localized_shoulder_segment*, or *downhill_same_basin_relaxation* as appropriate), and converged with maximum NEB force not exceeding $0.10\text{ eV}/\text{Å}$. Off-family relays, local-equivalent placeholders, non-promoted shoulder images, and otherwise interpretable but high-force paths were retained as context but were not counted as accepted closure.

Thermochemical interpretation was restricted to the completed 600 K packet. Adsorbate-only harmonic corrections were constructed with the slab frozen and active adsorbate indices [36, 37, 38, 39, 40]. Modes below 50 cm^{-1} were floored before building the harmonic correction, and transition-state-like values for shoulder or highest-image states were treated as approximate because they derive from NEB images rather than independently optimized first-order saddle points. A recent high-level Cu(111) study further underscores that delicate barrier ordering on this surface can be method-sensitive, reinforcing the value of reporting the present campaign as a bounded MACE-only network result rather than a universal mechanistic adjudication [Chen et al. \[2025\]](#).

3 Results

3.1 Network overview

The completed MACE-only campaign discovered a 41-minimum low-coverage RWGS-like network on clean Cu(111). The supported node families span an all-bound $\text{CHO}_2^* + \text{H}^*$ basin, CH_2O_2^* minima, $\text{CHO}^* + \text{HO}^*$ cleavage products, a split $\text{CO}^* + \text{H}^* + \text{HO}^*$ basin, and the product-side $\text{CO}^* + \text{H}_2\text{O}^*$ state. This topology already shows that the search does not collapse into a single smooth route: a low-lying formate-like branch is present, a chemically credible downstream oxygenated branch is present, and the dominant methodological question becomes whether strict in-family continuity can be established between them.

The completed 600 K packet emphasizes the same point. `start_rhnode_002` is the selected free-energy reference minimum, `start_unode_030` lies +0.870 eV above it, and the downstream representatives `mid_unode_008` and `mid_unode_010` both lie near +0.276 eV. The final interpretation is therefore not blocked by obviously inaccessible downstream thermodynamics, but by the inability to certify low-force accepted connectors across the unresolved continuity gaps. In the plotted dominant packet, `start_unode_030` denotes a local $\text{CO}_2^* + \text{H}_2^*$ molecular- H_2 start state, `start_rhnode_002` the all-bound $\text{CHO}_2^* + \text{H}^*$ basin representative, `mid_unode_014/mid_unode_008` CH_2O_2^* basin representatives, `mid_unode_027/mid_unode_029` $\text{CHO}^* + \text{HO}^*$ cleavage and split-entry states, `mid_hnode_006/mid_hnode_005` $\text{CO}^* + \text{H}^* + \text{HO}^*$ split-basin states, and `mid_unode_010` the $\text{CO}^* + \text{H}_2\text{O}^*$ product state.

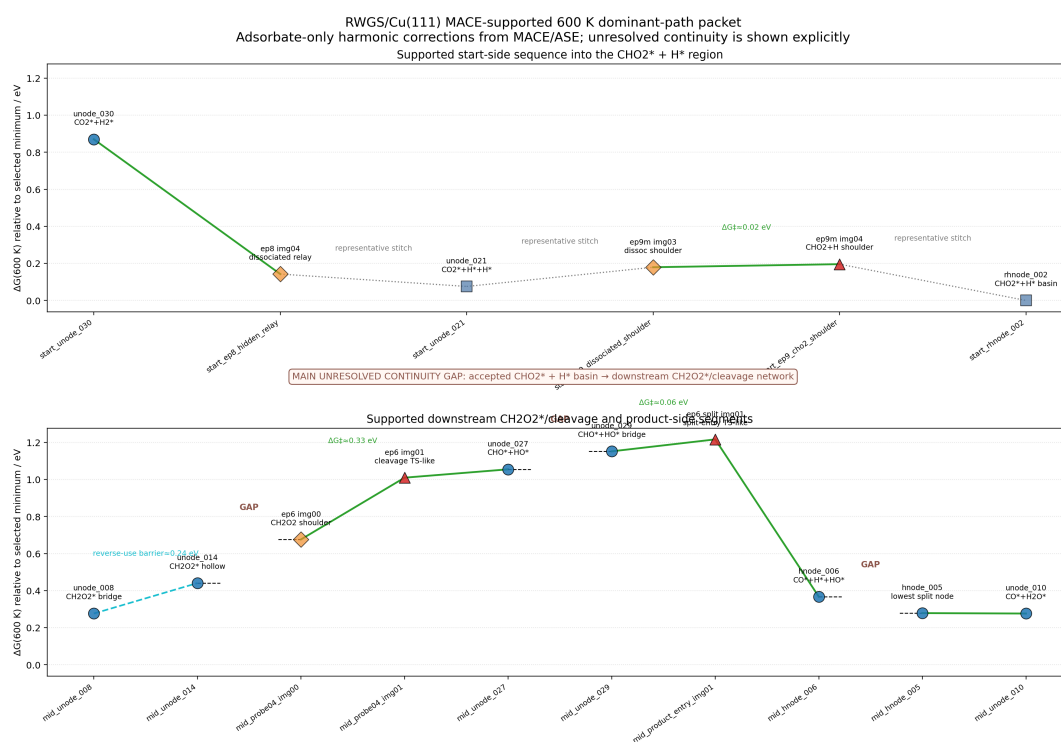


Figure 1: Dominant 600 K RWGS profile on Cu(111). Node IDs correspond to the chemically audited states described in the text, so the plotted packets can be read as molecular-H₂/CHO₂* + H* start-side chemistry, CH₂O₂* and CHO* + HO* downstream oxygenate chemistry, and CO* + H* + HO*/CO* + H₂O* product-side chemistry. The packet includes accepted microsegments and downstream accepted segments, while the unresolved upstream continuity gap is kept explicit. The final post-recursive interpretation is partially continuous but still globally discontinuous because only the split-basin handoff gap closed strictly.

3.2 Accepted segments and strict gap outcomes

The accepted start-side chemistry begins from `start_unode_030`, a local $\text{CO}_2^* + \text{H}_2^*$ molecular- H_2 state. A short probe resolved an accepted start-dissociation microsegment to an adjacent dissociated $\text{CO}_2^* + \text{H}^* + \text{H}^*$ relay with a 0.0000 eV forward barrier and 0.0496 eV/Å maximum NEB force. Direct CH_2O_2 entry from that dissociated region was not accepted, but a refined adjacent probe isolated an accepted CHO_2 -forming microsegment from the final dissociated shoulder to the $\text{CHO}_2^* + \text{H}^*$ bridge-entry shoulder with a 0.0261 eV forward barrier and 0.0351 eV/Å maximum force. Together, these steps place the search into the low-lying $\text{CHO}_2^* + \text{H}^*$ basin region represented by `start_rhnode_002`.

The downstream branch contains several accepted local motifs. Within the CH_2O_2 family, the accepted `mid_unode_014` \rightarrow `mid_unode_008` same-basin relaxation is downhill in the accepted direction, with a 0.0000 eV forward barrier, 0.2438 eV reverse barrier, and 0.0490 eV/Å maximum force. Localization around a shoulder anchor produced an accepted cleavage segment into `mid_unode_027` with a 0.3642 eV forward barrier and 0.0498 eV/Å maximum force. The late branch then supports an accepted split-basin entry `mid_unode_029` \rightarrow `mid_hnode_006` with a 0.1543 eV forward barrier, 0.8902 eV reverse barrier, and 0.0490 eV/Å maximum force, followed by the accepted product closure `mid_hnode_005` \rightarrow `mid_unode_010`, which is barrierless in the forward direction.

The most important strict closure result lies inside the split-product family. Gap 4, the `mid_hnode_006` \rightarrow `mid_hnode_005` handoff, was not accepted by the initial direct short probe because the direct band remained high-force at 0.159071 eV/Å. Recursive localization first isolated an accepted local placeholder-supported segment, and seeded stable-to-stable tightening then produced a strict primitive connector with a 0.0112 eV forward barrier, a 0.1333 eV reverse barrier, and a 0.0499 eV/Å maximum NEB force. This is the only continuity gap that closed strictly under the final campaign rule.

Table 1: Main accepted segments and final strict gap status for the Cu(111) RWGS network. The added chemical-event column decodes the node IDs into chemically legible state changes. Blank quantities were not explicitly reported in retained artifacts.

Segment or gap	Chemical event / meaning	Final interpretation	Forward barrier (eV)	Reverse barrier (eV)	Max force (eV/Å)
start_unode_030 → adjacent dissociated relay	$\text{CO}_2^* + \text{H}_2^*$ start state dissociates to an adjacent relay	Accepted start dissociation	0.0000	—	0.0496
Dissociated shoulder → CHO₂-entry shoulder	$\text{CO}_2^* + \text{H}^* + \text{H}^*$ relay dissociated $\text{CO}_2/\text{H}/\text{H}$ shoulder reorganizes toward $\text{CHO}_2^* + \text{H}^*$ formation	Accepted CHO_2 -forming step	0.0261	—	0.0351
mid_unode_014 → mid_unode_008	Higher CH_2O_2^* basin relaxes into the lower CH_2O_2^* representative	Accepted downhill same-basin relaxation	0.0000	0.2438	0.0490
CH_2O_2 shoulder anchor → mid_unode_027	Localized CH_2O_2^* cleavage yields $\text{CHO}^* + \text{HO}^*$ products	Accepted localized cleavage	0.3642	0.0122	0.0498
mid_unode_029 → mid_hnode_006	$\text{CHO}^* + \text{HO}^*$ split-entry state enters the $\text{CO}^* + \text{H}^* + \text{HO}^*$ basin	Accepted split-basin entry	0.1543	0.8902	0.0490
mid_hnode_006 → mid_hnode_005	Internal split-basin handoff reaches the lowest accepted $\text{CO}^* + \text{H}^* + \text{HO}^*$ node	Accepted strict split-basin handoff	0.0112	0.1333	0.0499
mid_hnode_005 → mid_unode_010	Product-side closure forms the $\text{CO}^* + \text{H}_2\text{O}^*$ state	Accepted product closure	0.0000	not reported	0.0350
start_rhnode_002 → downstream	Missing strict connector from the $\text{CHO}_2^* + \text{H}^*$ basin into the downstream oxygenate packet	Not accepted; gap 1 open	—	—	—
Stable CH_2O_2 basin → cleavage entry region	Missing strict handoff from stable CH_2O_2^* minima into the cleavage-entry shoulder region	Not accepted; gap 2 open	—	—	—
mid_unode_027 → mid_unode_029	Missing strict connector within the $\text{CHO}^* + \text{HO}^*$ family before split-basin entry	Not accepted; gap 3 open	—	—	—

The recursive closure campaign makes the global network status unambiguous. Gap 1 remained unresolved after one direct probe, five decomposition-derived probes, and one tightening attempt. The best force-limited primitive candidate, `rhnode_002` \rightarrow `unode_001`, retained a maximum force of 0.12611 eV/Å, while the best low-force downstream tightening reached 0.04999 eV/Å but still classified as *shoulder_or_plateau*. Gap 2 also remained unresolved: recursive localization repeatedly collapsed onto existing CH_2O_2 and $\text{CHO}^* + \text{HO}^*$ states, and the best tightened local candidate `unode_024` \rightarrow `unode_027` still retained a 0.94286 eV/Å maximum force. Gap 3 came closest to formal acceptance in force terms, because the tightened band reached 0.09029 eV/Å, but it still behaved as a two-shoulder plateau and therefore remained outside the accepted class list. Gap 4 alone closed strictly through recursive localization plus seeded tightening. These unresolved handoffs are chemically meaningful because they separate distinct oxygenate manifolds on Cu(111)—a formate-like $\text{CHO}_2^* + \text{H}^*$ packet, CH_2O_2^* basin variants, and CO/OH/ H_2O -containing downstream states—rather than merely relabeling one shallow minimum family [Grabow and Mavrikakis \[2011\]](#), [Zhao et al. \[2011\]](#), [Takeyasu et al. \[2022\]](#), [Li et al. \[2022\]](#).

The final network is therefore partially continuous, but still globally discontinuous after exhaustive recursive probing. The accepted start-side $\text{CHO}_2^* + \text{H}^*$ packet and the accepted downstream CH_2O_2 /cleavage/product packet are both chemically meaningful, yet they are not joined by a strict accepted in-family connector.

4 Discussion and Limitations

The present network establishes a strong topology-level claim while also defining its scope. Autonomous MACE-only exploration without literature seeding recovers a nontrivial RWGS-like Cu(111) network with chemically interpretable entry, cleavage, split-basin, and product-closure motifs. The accepted segments are not arbitrary: each survives the final class-and-force rule, and the downstream packet is strengthened by a genuinely strict product-side split-basin handoff.

The principal limitation is equally clear. In this campaign, MACE NEB optimization on Cu(111) often became trapped in high-force or plateau-like regions even when a local rearrangement appeared chemically plausible. Endpoint repair, hidden-state extraction, relaxation-based localization, decomposition, and seeded tightening mitigated that behavior and recovered accepted local chemistry, but they did not eliminate the unresolved status of gaps 1–3. Some accepted segments are therefore localized microsegments involving shoulder or pseudo-state endpoints rather than direct stable-minimum-to-stable-minimum barriers, and the 600 K corrections for TS-like images remain approximate because they are based on NEB images rather than optimized saddles. The resulting interpretation is intentionally conservative: this campaign supports an audited partial network and an effective corrective workflow, but it does not certify one fully continuous RWGS mechanism on clean Cu(111).

5 Conclusions

Autonomous MACE-only exploration on clean Cu(111) discovered a 41-minimum low-coverage RWGS-like network spanning $\text{CHO}_2^* + \text{H}^*$, CH_2O_2^* , $\text{CHO}^* + \text{HO}^*$, $\text{CO}^* + \text{H}^* + \text{HO}^*$, and $\text{CO}^* + \text{H}_2\text{O}^*$ regions. Accepted segments support local start-side dissociation, CHO_2 entry, CH_2O_2 same-basin relaxation, localized cleavage into $\text{CHO}^* + \text{HO}^*$, split-basin entry, strict split-basin handoff closure, and product closure. However, strict recursive closure across the four named continuity gaps closed only gap 4. Gaps 1–3 remained unresolved because their best candidates were high-force, plateau-like, or placeholder-dependent under the final rule.

The final Cu(111) MACE network must therefore be reported as partially continuous and still globally discontinuous after exhaustive recursive probing. That outcome is the central audited result of the campaign: autonomous MACE-only exploration recovered a substantial RWGS-like network on Cu(111), while the full trial ledger also shows exactly where high-force NEB sticking motivated corrective localization and where strict continuity could still not be claimed.

References

- Sung Sakong and Axel Groß. Dissociative adsorption of hydrogen on strained cu surfaces. *Surface Science*, 525(1–3):107–118, 2003. doi: 10.1016/S0039-6028(02)02550-5.
- Kun Cao, Gernot Fuchs, Aart W. Kleyn, and Ludo B. F. Juurlink. Hydrogen adsorption and desorption from Cu(111) and Cu(211). *Physical Chemistry Chemical Physics*, 20(35):22477–22488, 2018. doi: 10.1039/C8CP03386B.
- Ya-Fan Zhao, Yong Yang, Charles A. Mims, Charles H. F. Peden, Jun Li, and Donghai Mei. Insight into methanol synthesis from CO₂ hydrogenation on Cu(111): Complex reaction network and the effects of H₂O. *Journal of Catalysis*, 281(2):199–211, 2011. doi: 10.1016/j.jcat.2011.04.012.
- Lars C. Grabow and Manos Mavrikakis. Mechanism of methanol synthesis on cu through CO₂ and CO hydrogenation. *ACS Catalysis*, 1(4):365–384, 2011. doi: 10.1021/cs200055d.
- Kotaro Takeyasu, Yasutaka Sawaki, Takumi Imabayashi, Septia Eka Marsha Putra, Harry Handoko Halim, Jiamei Quan, Yuji Hamamoto, Ikutaro Hamada, Yoshitada Morikawa, Takahiro Kondo, Tadahiro Fujitani, and Junji Nakamura. Hydrogenation of formate species using atomic hydrogen on a Cu(111) model catalyst. *Journal of the American Chemical Society*, 144(27):12158–12166, 2022. doi: 10.1021/jacs.2c02797.
- Zhiyuan Li, Na Li, Nan Wang, Bing Zhou, Pan Yin, Boyu Song, Jun Yu, and Yusen Yang. Mechanism investigations on water gas shift reaction over Cu(111), Cu(100), and Cu(211) surfaces. *ACS Omega*, 7(4):3514–3521, 2022. doi: 10.1021/acsomega.1c05991.
- Zheng Chen, Zhangyun Liu, and Xin Xu. Clarifying the methanol synthesis mechanism via CO₂ hydrogenation on the Cu(111) surface: Insights from accurate doubly hybrid density functionals. *ACS Catalysis*, 15(6):5039–5045, 2025. doi: 10.1021/acscatal.5c01099.

Supporting Information / Appendices

This appendix preserves the retained Appendix A and Appendix B coverage from the audited manuscript package. The tabulations are transcribed directly from the canonical CSV artifacts. The longtables are intentionally dense and primarily serve as machine-readable audit ledgers for the endpoint packet and the full NEB trial history; the main text should be used for the claim-critical continuity interpretation. Blank cells indicate quantities that were not explicitly reported in the retained artifacts.

Appendix A. Endpoint relaxations and 600 K corrections for the constructed network

Table A1 summarizes the endpoint relaxations and 600 K corrections transcribed from the canonical Appendix A CSV. The tabulation retains the constructed-network state identities together with branch labels, state kinds, electronic energies, 600 K corrected free energies, offsets relative to the selected reference minimum `start_rhnode_002`, and source notes. Where a note predates the final recursive-closure state, the main-text continuity statement remains authoritative.

Table A1: Endpoint relaxations and 600 K corrections for the constructed Cu(111) RWGS network.

State ID	Label	Branch	State kind	Electronic E (eV)	$G_{600\text{ K}}$ (eV)	ΔE ref. (eV)	$\Delta G_{600\text{ K}}$ ref. (eV)	Note
mid_unode_008	Bridge CH ₂ O ₂ * basin representative (unode_008)	downstream branch	stable	-172.716	-172.408	0.309	0.276	stable gap-main gap endpoint Lowest supported CH ₂ O ₂ * basin representative on the downstream branch.
mid_unode_014	Higher-lying CH ₂ O ₂ * hollow-site basin representative (unode_014)	downstream branch	stable	-172.472	-172.244	0.553	0.441	stable supported gap endpoint Accepted same-basin site/orientation state linked downhill to unode_008.
mid_probe04_img00	Local-equivalent CH ₂ O ₂ * cleavage shoulder anchor (episode 6 image 00)	downstream branch	pseudo	-172.249	-172.008	0.776	0.676	pseudo gap-local Pseudo-state anchor for the localized cleavage segment; no direct accepted connector is claimed from unode_014 to this shoulder image.
mid_probe04_img01	CHO ₂ /CHOOH cleavage TS-like highest image (episode 6 image 01)	downstream branch	TS-like	-171.884	-171.675	1.141	1.010	TS-like supported Accepted highest image of the localized cleavage segment; treated as TS-like for 600 K correction purposes.
mid_unode_027	CHO* + HO* hollow-site cleavage product (unode_027)	downstream branch	stable	-171.897	-171.630	1.128	1.055	stable supported gap endpoint Stable endpoint of the accepted localized cleavage segment.
mid_unode_029	CHO* + HO* bridge-side split-entry reactant (unode_029)	downstream branch	stable	-171.725	-171.533	1.300	1.152	stable gap-family gap endpoint Stable CHO*+HO* representative used as the reactant for the accepted split-entry segment; no accepted connector is claimed from unode_027.
mid_product_entry_img01	Split-entry TS-like image to CO* + H* + HO* basin (episode 6 image 01)	downstream branch	TS-like	-171.571	-171.468	1.454	1.216	TS-like supported Accepted highest image for entry into the split-product basin; treated as TS-like for 600 K correction purposes.
mid_hnode_006	CO* + H* + HO* split-basin surrogate (hnode_006)	downstream branch	stable	-172.461	-172.318	0.564	0.367	stable supported gap endpoint Stable endpoint of the accepted split-entry segment.
mid_hnode_005	Lowest CO* + H* + HO* split-basin node (hnode_005)	downstream branch	stable	-172.583	-172.406	0.442	0.279	stable gap-split gap endpoint Lowest accepted split node; shown separately because the hnode_006 -> hnode_005 handoff is not resolved by an accepted segment.
mid_unode_010	CO* + H ₂ O* product state (unode_010)	downstream branch	stable	-172.588	-172.408	0.437	0.276	stable supported Stable product-side endpoint of the accepted closure segment from hnode_005.
start_unode_030	CO ₂ * + H ₂ * local molecular-H ₂ state (unode_030)	start-side branch	stable	-171.678	-171.815	1.347	0.870	stable supported Accepted start-side molecular-H ₂ reactant-state representative from unique-relaxed-nodes.

Continued on next page

Table A1: Endpoint relaxations and 600 K corrections for the constructed Cu(111) RWGS network (continued).

State ID	Label	Branch	State kind	Electronic E (eV)	$G_{600\text{ K}}$ (eV)	ΔE ref. (eV)	$\Delta G_{600\text{ K}}$ ref. (eV)	Note
start_ep8_hidden_relay	Adjacent dissociated $\text{CO}_2^* + \text{H}^* + \text{H}^*$ hidden relay (episode 8 endpoint image 04)	start-side branch	pseudo	-172.278	-172.542	0.747	0.142	pseudo supported Endpoint of accepted primitive start-dissociation microsegment.
start_unode_021	Stable dissociated $\text{CO}_2^* + \text{H}^* + \text{H}^*$ basin representative (unode_021)	start-side branch	stable repr.	-172.286	-172.609	0.739	0.076	stable repr. representative only Stable fully adsorbed $\text{CO}_2/\text{H}/\text{H}$ representative shown for start-side context; no direct accepted connector is claimed to adjacent hidden relay or later shoulder image.
start_ep9_dissociated_shoulder	Final dissociated shoulder immediately before CHO_2 formation (episode 9 micro image 03)	start-side branch	pseudo	-172.243	-172.505	0.781	0.179	pseudo supported Reactant-side endpoint of accepted adjacent CHO_2 -forming microsegment.
start_ep9_cho2_shoulder	$\text{CHO}_2^* + \text{H}^*$ bridge-entry shoulder (episode 9 micro image 04)	start-side branch	TS-like	-172.236	-172.489	0.789	0.196	TS-like supported Accepted adjacent CHO_2 -forming endpoint; treated as TS-like/highest-image shoulder for 600 K correction purposes.
start_rhnode_002	All-bound $\text{CHO}_2^* + \text{H}^*$ bridge-side basin representative (rhnode_002)	start-side branch	stable repr.	-173.025	-172.685	0.000	0.000	stable repr. representative only gap endpoint Accepted $\text{CHO}_2^* + \text{H}^*$ basin representative used in the episode 10 continuity test; shown without a claimed accepted connector from the episode 9 micro shoulder image.

Appendix B. Comprehensive NEB optimization-trial table

Table B1 preserves the full NEB-trial ledger transcribed from the canonical CSV, including direct probes, decomposition and localization probes, tightening attempts, accepted segments, and context-only runs that informed the final network interpretation. The appendix follows the same column coverage as the audited markdown manuscript bundle for compilation reliability.

Table B1: Comprehensive NEB optimization-trial table for the Cu(111) RWGS campaign.

Episode	Trial ID	Reaction label	From	To	Opt. steps	Relax. steps	Max force (eV/Å)	Fwd barrier (eV)	Rev barrier (eV)	Class	Status	Accepted	Context
frontier_episode10_cho2h_to_ch2o2_bridge	task_01_direct_001_rhnode_002_to_unode_008_localeq	rhnode_002 -> unode_008-matched local-equivalent CH2O2 basin image	rhnode_002	probe_02_ch2o2_bridge_final_from_split2_img03	160		0.4380	1.1706	0.0000	shoulder/plat.	not converged; completed	no	Episode 10 continuity test: no accepted downstream connector.
frontier_episode10_cho2h_to_ch2o2_bridge	task_02_direct_002_rhnode_002_to_unode_014_localeq	rhnode_002 -> unode_014-matched local-equivalent CH2O2 basin image	rhnode_002	probe_02_hidden_hh_to_ch2o2_u008_img03	160		0.1860	1.0762	0.0000	shoulder/plat.	not converged; completed	no	Episode 10 continuity test: no accepted downstream connector.
frontier_episode10_cho2h_to_ch2o2_bridge	task_03_direct_006_rhnode_002_to_unode_009_localeq	rhnode_002 -> unode_009-matched local-equivalent CH2O2 basin image	rhnode_002	probe_02_ch2o2_fu02_img02_to_img04_img03	160		0.2418	0.8487	0.0000	shoulder/plat.	not converged; completed	no	Episode 10 continuity test: no accepted downstream connector.
frontier_episode10_cho2h_to_ch2o2_bridge	task_04_fallback_001_rhnode_002	rhnode_002 -> local-equivalent all-bound CHO2* + H* bridge-side shoulder	rhnode_002	probe_03_ch2o2_final_img03_to_img04_img04	160		0.1337	1.8172	1.0284	shoulder/plat.	not converged; completed	no	Episode 10 continuity test: no accepted downstream connector.
frontier_episode10_cho2h_to_ch2o2_bridge	task_05_fallback_002_rhnode_002	rhnode_002 -> local-equivalent all-bound CHO2* + H* bridge-side shoulder	rhnode_002	probe_03_ch2o2_final_img03_to_img04_img03	160		0.1430	1.8230	1.0415	shoulder/plat.	not converged; completed	no	Episode 10 continuity test: no accepted downstream connector.
frontier_episode11_gap1_recursive_closure	task_01_direct_rhnode002_to_downstream_cho2h_img04_shoulder_short	short direct probe: rhnode_002 -> accepted downstream CHO2/H shoulder img04	rhnode_002	probe_03_ch2o2_final_img03_to_img04_img04	15		2.0375	4.5394	3.7506	shoulder/plat.	not converged; completed	no	Recursive-closure flag.
frontier_episode11_gap1_recursive_closure	task_02_decomp_rhnode002_to_unode001_short	short decomposition probe: rhnode_002 -> unode_001 gas-like CHO2/H local equivalent	rhnode_002	unode_001	15		0.1261	0.1263	0.1385	primitive	not converged; completed	no	Gap 1 recursive closure: best start-adjacent decomposition candidate.
frontier_episode11_gap1_recursive_closure	task_03_decomp_relax_task04_img01_to_downstream_cho2h_img04_shoulder_short	short decomposition probe: relaxed HOCO-like gas-like shoulder -> downstream CHO2/H shoulder img04	relax_ep10_task04_img01	probe_03_ch2o2_final_img03_to_img04_img04	15	ep10_task04_img01:46	10.9685	2.8259	3.8302	shoulder/plat.	not converged; completed	no	Recursive-closure flag.
frontier_episode11_gap1_recursive_closure	task_04_decomp_relax_task04_img02_to_downstream_cho2h_img04_shoulder_short	short decomposition probe: relaxed ep10 dissociated CO2+H+H shoulder -> downstream CHO2/H shoulder img04	relax_ep10_task04_img02	probe_03_ch2o2_final_img03_to_img04_img04	15	ep10_task04_img02:60	2.5447	2.0151	2.9225	shoulder/plat.	not converged; completed	no	Recursive-closure flag.

Continued on next page

Table B1: Comprehensive NEB optimization-trial table for the Cu(111) RWGS campaign (continued).

Episode	Trial ID	Reaction label	From	To	Opt. steps	Relax. steps	Max force (eV/Å)	Fwd barrier (eV)	Rev barrier (eV)	Class	Status	Accepted	Context
frontier_episode11_gap1_recursive_closure	task_05_decomp_g3_t1img03_to_g3_t4img03_short	short decomposition probe: direct-derived dissociated shoulder -> localized unode_019-like dissociated basin	relax_gen2_t1_img03	relax_gen2_t4_img03	15	gen2_t1_img03; 200;	2.2296	0.4113	1.4353	shoulder/plat.	not converged; completed	no	Recursive-closure flag.
frontier_episode11_gap1_recursive_closure	task_06_decomp_g3_t4img03_to_downstream_cho2_h_shoulders_img04	short decomposition probe: localized unode_019-like dissociated basin -> downstream CHO2/H shoulder	relax_gen2_t1_img03	probe_03_cho2_final_img03_to_img04_img04	15	gen2_t4_img03; 200	0.0983	0.0341	0.0000	shoulder/plat.	lower; completed; converged	no	Recursive-closure flag.
frontier_episode11_gap1_recursive_closure	task_07_tighten_g3_t4img03_to_downstream_cho2_h_shoulders_img04	tightening probe: localized unode_019-like dissociated basin -> downstream CHO2/H shoulder	relax_gen2_t1_img03	probe_03_cho2_final_img03_to_img04_img04	120	gen2_t4_img03; 200	0.0500	0.0341	0.0000	shoulder/plat.	high; completed; converged	no	Gap 1 recursive closure: best localized downstream candidate after tightening.
frontier_episode12_gap2_recursive_closure	task_01_direct_unode008_to_midprobe04img00	direct short probe: stable CH2O2 basin unode_008 -> localized cleavage shoulder anchor mid-probe04-img00	unode_008	mid_probe04_img00	16		0.8648	0.6802	0.2132	primitive	not converged; completed	no	Recursive-closure flag.
frontier_episode12_gap2_recursive_closure	task_02_direct_unode014_to_midprobe04img00	direct short probe: stable CH2O2 basin unode_014 -> localized cleavage shoulder anchor mid-probe04-img00	unode_014	mid_probe04_img00	16		4.3175	4.3533	4.1300	shoulder/plat.	not converged; completed	no	Recursive-closure flag.
frontier_episode12_gap2_recursive_closure	task_03_decomp_unode024_to_midprobe04img00	decomposition-derived short probe: stable CH2O2 unode_024 -> localized cleavage shoulder anchor mid-probe04-img00	unode_024	mid_probe04_img00	16		1.3969	0.6114	0.7122	invalid	not converged; completed	no	Recursive-closure flag.
frontier_episode12_gap2_recursive_closure	task_04_decomp_unode024_to_unode027_short	decomposition-derived short probe: stable CH2O2 unode_024 -> stable CHO* + HO* entry node unode_027	unode_024	unode_027	16		1.7378	1.4030	1.1518	prim-localized	not converged; completed	no	Recursive-closure flag.
frontier_episode12_gap2_recursive_closure	task_05_localization_relaxgen1img02_to_midprobe04img00	localization short probe: relaxed direct-probe image02 local equivalent -> localized cleavage shoulder anchor mid-probe04-img00	relax_gen1_img02	mid_probe04_img00	16	gen1_img02; task02_img02; 135	2.8728	1.1313	1.2414	primitive	not converged; completed	no	Recursive-closure flag.

Continued on next page

Table B1: Comprehensive NEB optimization-trial table for the Cu(111) RWGS campaign (continued).

Episode	Trial ID	Reaction label	From	To	Opt. steps	Relax. steps	Max force (eV/Å)	Fwd barrier (eV)	Rev barrier (eV)	Class	Status	Accepted	Context
frontier_episode12_gap2_recursive_closure	task_06_tighten_unode024_to_unode027_from_gen3_task04	tightening attempt: decomposition-derived local candidate unode_024 -> unode_027 from gen3 task04 seeded band	unode_024	unode_027	160		0.9429	0.5936	0.3424	prim.-localized	not converged; completed	no	Recursive-closure flag.
frontier_episode13_gap3_recursive_closure	task_01_direct_unode027_to_unode029_short	direct short probe: supported CHO*+HO* family state unode_027 -> supported CHO*+HO* family state unode_029	unode_027	unode_029	16		2.8357	0.8849	0.7136	shoulder/plat.	not converged; completed	no	Recursive-closure flag.
frontier_episode13_gap3_recursive_closure	task_02_localize_unode027_to_ep12img02_short	localization short probe: stable unode_027 -> episode12 bridge/hollow CHO+HO shoulder	unode_027	ep12_task04_img02	16	ep12_task04_img02: 196	0.5837	1.1518	0.0000	primitive	not converged; completed	no	Recursive-closure flag.
frontier_episode13_gap3_recursive_closure	task_03_localize_ep12img02_to_unode029_short	localization short probe: episode12 bridge/hollow CHO+HO shoulder -> stable unode_029	ep12_task04_img02	unode_029	16	ep12_task04_img02: 196	2.2110	0.0000	0.9805	loc. shoulder	not converged; completed	no	Recursive-closure flag.
frontier_episode13_gap3_recursive_closure	task_04_localize_unode027_to_gen1img01_short	localization short probe: stable unode_027 -> direct-probe CHO ontop + HO hollow local equivalent	unode_027	task_01_to_unode029_short_img01	16		0.3556	0.7050	0.0000	loc. shoulder	not converged; completed	no	Recursive-closure flag.
frontier_episode13_gap3_recursive_closure	task_05_localize_gen1img01_to_gen1img02_short	localization short probe: direct-probe local equivalent img01 -> img02 within the CHO+HO family	task_01_direct_unode027_to_unode029_short_img01	task_01_direct_unode027_to_unode029_short_img02	16		0.4713	0.1799	0.0000	primitive	not converged; completed	no	Recursive-closure flag.
frontier_episode13_gap3_recursive_closure	task_06_localize_gen1img02_to_unode029_short	localization short probe: direct-probe CHO ontop + HO bridge local equivalent -> stable unode_029	task_01_direct_unode027_to_unode029_short_img01	unode_029	16		0.1919	0.0000	0.7136	loc. shoulder	not converged; completed	no	Recursive-closure flag.
frontier_episode13_gap3_recursive_closure	task_07_tighten_unode027_to_unode029_from_local_chain	tightening attempt: decomposition-derived in-family local chain unode_027 -> unode_029	unode_027	unode_029	160		0.0903	0.1713	0.0000	shoulder/plat. lower:	not completed; not converged	no	Recursive-closure flag.

Continued on next page

Table B1: Comprehensive NEB optimization-trial table for the Cu(111) RWGS campaign (continued).

Episode	Trial ID	Reaction label	From	To	Opt. steps	Relax. steps	Max force (eV/Å)	Fwd barrier (eV)	Rev barrier (eV)	Class	Status	Accepted	Context
frontier_episode14_gap4_recursive_closure	task_01_direct_hnode006_to_hnode005_short	direct short probe: supported CO* + H* + HO* split-basin state hnode_006 -> supported CO* + H* + HO* split-basin state hnode_005	hnode_006	hnode_005	18		0.1591	0.0080	0.1300	primitive	not converged; completed	no	Recursive-closure flag.
frontier_episode14_gap4_recursive_closure	task_02_localize_hnode006_to_stepping03_short	localization short probe: stable hnode_006 -> prior step1 hnode_006-like interior image03	hnode_006	step1_unode_029_to_hnode_006_img03	16		0.2766	0.5346	0.0000	loc. shoulder	not converged; completed	no	Recursive-closure flag.
frontier_episode14_gap4_recursive_closure	task_03_localize_stepping03_to_stepping04_short	localization short probe: prior step1 hnode_006-like image03 -> prior step1 hnode_005-like image04	step1_unode_029_to_hnode_006_img03	step1_unode_029_to_hnode_006_img04	16		0.1950	0.0000	0.3849	downhill basin	not converged; completed	no	Recursive-closure flag.
frontier_episode14_gap4_recursive_closure	task_04_localize_stepping04_to_hnode005_short	localization short probe: prior step1 hnode_005-like image04 -> stable hnode_005	step1_unode_029_to_hnode_006_img04	hnode_005	16		0.1769	0.0000	0.2718	downhill basin	not converged; completed	no	Recursive-closure flag.
frontier_episode14_gap4_recursive_closure	task_05_localize_hnode006_to_stepping04_short	localization short probe: stable hnode_006 -> prior step1 hnode_005-like image04	hnode_006	step1_unode_029_to_hnode_006_img04	16		0.0941	0.1497	0.0000	primitive	lower; completed; converged	yes	Recursive-closure flag.
frontier_episode14_gap4_recursive_closure	task_06_tighten_hnode006_to_hnode005_from_task05_chain	tightening attempt: decomposition-derived local chain hnode_006 -> hnode_005 from task05 seeded band	hnode_006	hnode_005	300		0.0499	0.0112	0.1333	primitive	high; completed; converged	yes	Recursive-closure flag.
frontier_episode3_product_split	step1_unode_029_to_hnode_005	unode_029 -> hnode_005	unode_029	hnode_005	80		0.1091	0.1278		shoulder/plat.	completed; converged	context only	Episode 3 probe-level split exploration; informative but superseded by later accepted split-entry/closure segments.
frontier_episode3_product_split	step2_hnode_005_to_unode_010	hnode_005 -> unode_010	hnode_005	unode_010	80		0.0350	0.0000		primitive	completed; converged	context only	Episode 3 probe-level split exploration; informative but superseded by later accepted split-entry/closure segments.
frontier_episode3_product_split	step2_hnode_005_to_unode_010	hnode_005 -> unode_010			300		0.0350	0.0000		primitive	completed; converged	yes	Accepted product-side closure carried into the final network interpretation.

Continued on next page

Table B1: Comprehensive NEB optimization-trial table for the Cu(111) RWGS campaign (continued).

Episode	Trial ID	Reaction label	From	To	Opt. steps	Relax. steps	Max force (eV/Å)	Fwd barrier (eV)	Rev barrier (eV)	Barrier Class	Status	Accepted	Context
frontier_episode6_mid_product_refinement	mid_local_equiv_unode_026_to_unode_029		unode_026	unode_029	500		0.1651	0.4386	0.2219	shoulder/plat.	not converged; completed	no	Not accepted in the episode 6 dominant-path interpretation (not converged).
frontier_episode6_mid_product_refinement	mid_local_equiv_unode_028_to_unode_029		unode_028	unode_029	500		0.1680	0.1307	0.0000	hidden intern.	not converged; completed	no	Not accepted in the episode 6 dominant-path interpretation (not converged).
frontier_episode6_mid_product_refinement	mid_shoulder_probe04_img02_to_img02_to_unode_027		probe_04_img02_local_equivalent	unode_027	500		0.0498	0.3642	0.0122	loc. shoulder	high; completed; converged	yes	Accepted in the episode 6 dominant-path interpretation (mid-cleavage shoulder localization).
frontier_episode6_mid_product_refinement	mid_step0_unode_014_to_unode_008		unode_014	unode_008	500		0.0490	0.0000	0.2438	downhill basin	high; completed; converged	yes	Accepted in the episode 6 dominant-path interpretation (mid-site hop within the CH ₂ O ₂ basin).
frontier_episode6_mid_product_refinement	product_entry_unode_029_to_hnode_006_seeded		unode_029	hnode_006	500		0.0490	0.1543	0.8902	prim-localized	high; completed; converged	yes	Accepted in the episode 6 dominant-path interpretation (split-basin local-equivalent entry).
frontier_episode8_adjacent_resolution	probe_01_u030_to_hidden_dissociated	unode_030 local molecular-H2 state -> adjacent dissociated hidden relay	probe_02_h2_cleavage_micro_extended_img02	probe_02_h2_cleavage_micro_extended_img03	400		0.0496	0.0000		primitive	high; completed; converged	yes	Episode 8 start probe; primitive; high.
frontier_episode8_adjacent_resolution	probe_02_hidden_hh_to_ch2o2_u008	adjacent hidden CO2+H+H relay -> adjacent CH2O2 basin image (u008-like)	probe_03_ch2o2_entry_plateau_to_local_basin_img02	probe_03_ch2o2_entry_plateau_to_local_basin_img03	400		1.0432	0.5643		hidden intern.	not accepted; not converged	no	Episode 8 first-basin probe; hidden intern.; not accepted.
frontier_episode9_start_basin_final_micro	probe_01_ch2o2_bridge_final_from_split1	final adjacent dissociated shoulder -> unode_008-like CH2O2 bridge basin	probe_01_ch2o2_hollow_entry_img02_to_img03	probe_01_ch2o2_hollow_entry_img02_to_img03	300		0.2781	0.5338		hidden intern.	not accepted; not converged	no	Episode 9 microprobe acceptance from probe analysis.
frontier_episode9_start_basin_final_micro	probe_02_ch2o2_bridge_final_from_split2	alternate final adjacent dissociated shoulder -> unode_008-like CH2O2 bridge basin	probe_02_ch2o2_ontop_entry_img02_to_img03	probe_02_ch2o2_ontop_entry_img02_to_img03	300		0.1777	0.9421		invalid	not accepted; not converged	no	Episode 9 microprobe acceptance from probe analysis.

Continued on next page

Table B1: Comprehensive NEB optimization-trial table for the Cu(111) RWGS campaign (continued).

Episode	Trial ID	Reaction label	From	To	Opt. steps	Relax. steps	Max force (eV/Å)	Fwd barrier (eV)	Rev barrier (eV)	Class	Status	Accepted	Context
frontier_episode9_start_basin_final_micro	probe_03_cho2_final_img03_to_img04	final adjacent dissociated shoulder -> CHO2 bridge-entry shoulder	probe_03_cho2_u019_entry_img02_to_img03_img03_img04	probe_03_cho2_u019_entry_img02_to_img03_img03_img04	300		0.0351	0.0261		primitive	high; completed; converged	yes	Episode 9 microprobe acceptance from probe analysis.

6.4 SAC Main Manuscript

The following pages reproduce the final SAC main manuscript produced by CatMaster from `Materials/project_space/SAC_New/files/writing/co2rr_sac_submission_grade/manuscript.pdf`. The corresponding archived source file is `Materials/project_space/SAC_New/files/writing/co2rr_sac_submission_grade/manuscript.tex`.

Solvated Thermodynamics of Graphene-Supported MN_4 Single-Atom Catalysts Identify B– CoN_4 and NiN_3B as Leading CO_2 -to-CO Motifs

Author metadata to be supplied before submission

Institutional affiliations to be supplied before submission

E-mail:

Abstract

Balancing $COOH^*$ formation against CO release remains the central thermodynamic challenge in designing single-atom catalysts for two-electron CO_2 reduction to CO. Here we examine graphene-supported MN_4 motifs with first-shell and second-shell heteroatom substitution by combining a 35-motif DFT matrix, limited implicit-solvation validation, solvated explicit-frequency computational hydrogen electrode analysis, and held-out-validated local surrogate alignment used only to prioritize targeted follow-up. Vacuum DFT retains CoN_4 , N– CoN_4 , NiN_3B , and B– CoN_4 as the strongest structurally stable motifs, whereas P– CoN_4 already couples favorable early proton-coupled electron transfer energetics to a large CO-desorption penalty. Implicit solvation moves B– CoN_4 to the leading electronic position, and the solvated explicit free-energy ordering becomes B– CoN_4 (0.015 eV), NiN_3B (0.062 eV), N– NiN_3B (0.080 eV), CoN_4 (0.118 eV), P– CoN_4 (0.211 eV), N– CoN_4 (0.361 eV), and CuN_4 (1.409 eV) by increasing limiting proton-coupled electron transfer cost. B– CoN_4 is therefore the strongest activation-side

motif, NiN₃B the closest overall competitor, and N–NiN₃B a validated Ni-family extension discovered through aligned-model prioritization and confirmed by DFT. P–CoN₄ remains chemically informative because strong early stabilization ($\Delta G_1 = -0.868$ eV) is paired with severe CO overbinding ($\Delta G_3 = 1.292$ eV). The resulting design picture is a coordination-controlled redistribution of ΔG_1 , ΔG_2 , and ΔG_3 : B–CoN₄ and NiN₃B are activation-side leaders, CoN₄ shifts the limiting proton-coupled electron transfer to COOH* reduction, and P–CoN₄/CuN₄ bracket the overbinding and underactivation extremes. Second-shell boron around Co and boron-containing NiN₃ coordination therefore emerge as the most effective routes to low thermodynamic CO₂-to-CO activation cost on this graphene MN₄ platform.

Introduction

Metal–nitrogen–carbon single-atom catalysts offer a compact platform for tuning the elementary thermodynamics of electrochemical CO₂-to-CO conversion because the adsorption pocket can be modified at the metal center, within the first coordination shell, or in the surrounding graphitic lattice while retaining atomic dispersion. Across this broader M–N–C family, both Ni- and Co-centered motifs can access strong CO selectivity when COOH* formation is sufficiently activated without locking the surface into strongly bound CO* intermediates.^{1–7}

Local coordination engineering therefore provides a chemically direct design variable. First-shell substitution changes the identity of the immediate metal coordination pocket, a control lever already shown to alter CO₂RR behavior in Co single-site systems, whereas second-shell heteroatoms perturb the same pocket more indirectly through the surrounding graphene framework.^{8–10} Recent studies have also emphasized that apparent activity gains must be weighed against adsorption imbalance and structural retention under operating conditions.¹¹ Phosphorus modification is an especially plausible test case because P incorporation can improve CO₂RR performance in some M–N–C families,¹² yet strong stabilization

of late intermediates remains a recurrent concern.

Here we examine that balance on a common graphene-supported MN_4 scaffold. The study begins from motif exploration on the shared template, but the rank-defining conclusions are assigned to DFT, limited solvation validation, and solvated explicit thermodynamics. A held-out-validated local MACE alignment is used only to prioritize a narrow follow-up within the Co/Ni N_3B neighborhood, where it nominates N-Ni N_3B for DFT confirmation. The final picture is a chemically differentiated catalyst set in which B-Co N_4 and Ni N_3B minimize the thermodynamic activation cost, N-Ni N_3B extends the Ni family, Co N_4 and N-Co N_4 anchor the more release-favored edge of the landscape, Cu N_4 defines the easy-release boundary, and P-Co N_4 serves as an overbinding comparator.

Computational Methods

Figure 1 summarizes the evidence hierarchy used in this study. Initial motif exploration was carried out on a common graphene-supported MN_4 scaffold with the MACE `mh-1` foundation model and dispersion-inclusive relaxations.¹³ All quantitative catalyst comparisons, however, were assigned to a 35-motif DFT matrix comprising five pristine MN_4 sites ($M = \text{Fe, Co, Ni, Cu, Zn}$), fifteen single first-shell substitutions, and fifteen single second-shell substitutions on the same structural template. A motif was retained only when bare, COOH*, and CO* relaxations converged while preserving the intended four-anchor pocket.

DFT slab calculations used spin-polarized PAW-PBE relaxations in VASP¹⁴⁻¹⁶ with fixed in-plane lattice vectors, `ISIF = 2`, `ISPIN = 2`, `ENCUT = 520 eV`, `EDIFF = 10-6 eV`, `EDIFFG = -0.02 eV Å-1`, up to 500 ionic steps, and D3 dispersion (`IVDW = 12`).¹⁷ The core-state

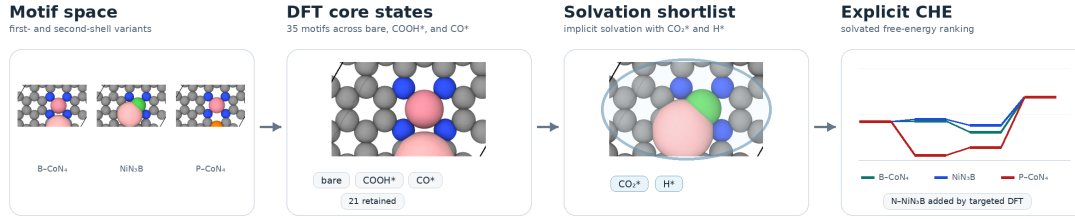


Figure 1: Chemistry-first overview of the evidence hierarchy used to define the final catalyst set. Motif exploration on the graphene-supported MN_4 scaffold was followed by DFT screening of bare, COOH^* , and CO^* states, limited implicit-solvation and extra-state validation, and solvated explicit CHE ranking. Targeted follow-up within the N_3B family added N–NiN₃B only after direct DFT confirmation.

electronic descriptors were evaluated as

$$\Delta E_1 = E(\text{COOH}^*) - E(*) - [E(\text{CO}_2) + \frac{1}{2}E(\text{H}_2)], \quad (1)$$

$$\Delta E_2 = E(\text{CO}^*) + E(\text{H}_2\text{O}) - E(\text{COOH}^*) - \frac{1}{2}E(\text{H}_2), \quad (2)$$

$$\Delta E_3 = E(\text{CO}) + E(*) - E(\text{CO}^*). \quad (3)$$

The compact vacuum and solvated “scores” reported below are lower-is-better electronic descriptors used for down-selection within the retained set; they are not the final thermodynamic ranking criterion.

Limited implicit-solvation validation then evaluated bare, CO_2^* , COOH^* , CO^* , and H-on-anchor states for the retained shortlist with VASPsol (LSOL = True, EB_K = 78.4, TAU = $5.25\text{e-}4$), followed by a later extension that placed N–NiN₃B on the same footing.¹⁸ The final ranking used a computational hydrogen electrode treatment¹⁹ at 298.15 K and 0 V_{RHE} with explicit adsorbate-only finite-difference vibrational corrections for COOH^* and CO^* on the retained catalyst set, processed consistently with VASPKIT.²⁰ Throughout this manuscript, “solvated explicit” denotes implicit-solvation electronic energies combined with explicit adsorbate vibrational corrections; no explicit solvent molecules were included. Final thermodynamic ordering is based on $\max(\Delta G_1, \Delta G_2)$ together with the CO-release penalty

ΔG_3 . Auxiliary ΔG_H and $\Delta G_{\text{CO}_2, \text{ads}}$ values remain mixed-source contextual descriptors and are discussed only as supporting context.

The aligned surrogate was evaluated independently of the catalyst ranking on a held-out set of 1633 structures from `dataset_v2_ref/test.extxyz`. It was then used only to prioritize a focused Co/Ni N₃B follow-up, after which the nominated motifs were reassessed by DFT before any inclusion in the final catalyst set.

Results and Discussion

DFT arbitration defines the retained catalyst space

DFT arbitration compresses the broad motif space into a chemically interpretable retained set. Of the 35 motifs in the primary matrix, 21 preserve the intended four-anchor pocket across bare, COOH*, and CO* states. The best vacuum electronic scores within this retained set are CoN₄ (0.246 eV), N-CoN₄ (0.329 eV), NiN₃B (0.428 eV), and B-CoN₄ (0.553 eV), with B-CuN₄ remaining a vacuum-competitive context motif that is documented in the Supporting Information. These values show that both first-shell and second-shell perturbations can survive structural arbitration, but they do not yet resolve whether early activation is purchased at the cost of severe late-stage binding.

The principal motifs carried into the main-text discussion are shown in Figure 2. B-CoN₄ and P-CoN₄ preserve the CoN₄ core while perturbing the surrounding graphene environment, whereas NiN₃B and N-NiN₃B directly demonstrate how first-shell boron and second-shell nitrogen reshape the Ni-centered pocket. The preserved local geometries emphasize that the eventual ranking is not controlled by collapse of the anchoring motif, but by how local coordination redistributes thermodynamic penalties across COOH* formation, COOH* reduction, and CO release.

P-CoN₄ already illustrates the central design tension at the vacuum DFT level. Its strongly favorable front-end descriptor ($\Delta E_1 = -1.410$ eV) is coupled to a large CO-

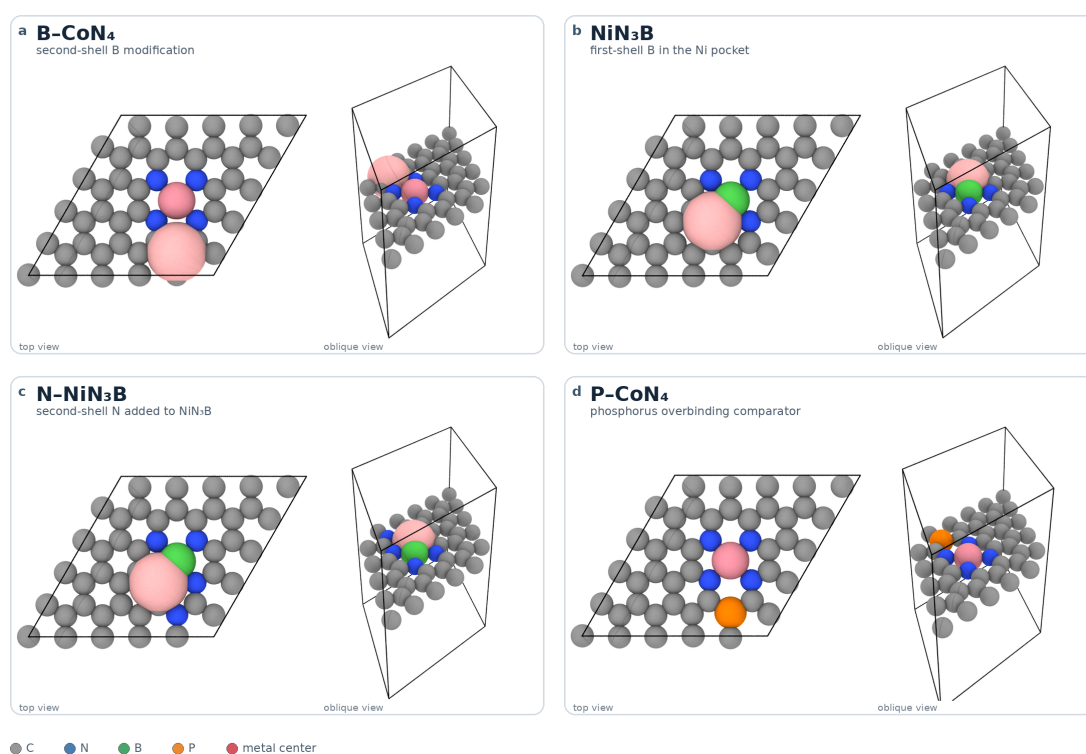


Figure 2: Bare-site geometries of the principal motifs advanced to the main-text catalyst discussion. Top views distinguish first-shell and second-shell substitution patterns, while oblique views show the retained four-anchor coordination pocket for B-CoN₄, NiN₃B, N-NiN₃B, and the overbinding comparator P-CoN₄. Atom colors are gray for C, blue for N, green for B, orange for P, and pink for the metal center.

desorption penalty ($\Delta E_3 = 1.836$ eV), whereas CuN_4 defines the opposite boundary with easy CO release ($\Delta E_3 = 0.163$ eV) but strongly uphill activation ($\Delta E_1 = 0.967$ eV). The most useful question is therefore not which motif dominates a single descriptor, but which motifs remain balanced once solvation and thermochemical corrections are introduced.

Table 1: Selected DFT and thermodynamic descriptors for the final catalyst set. Vacuum and solvated scores are lower-is-better electronic descriptors from the core-state screen and limited-solvation validation. Final ordering is determined by the solvated explicit CHE step free energies.

Motif	Role	Vacuum score (eV)	Solvated score (eV)	ΔG_1 (eV)	ΔG_2 (eV)	ΔG_3 (eV)	Limiting PCET (eV)
B-CoN ₄	activation lead	0.553	0.097	0.015	-0.288	0.908	0.015
NiN ₃ B	closest competitor	0.428	0.239	0.062	-0.152	0.725	0.062
N-NiN ₃ B	validated Ni motif	0.232	0.454	0.080	0.045	0.510	0.080
CoN ₄	Co benchmark	0.246	0.482	0.006	0.118	0.512	0.118
P-CoN ₄	overbinding comparator	1.036	0.581	-0.868	0.211	1.292	0.211
N-CoN ₄	release-favored comparator	0.329	0.513	0.361	0.164	0.110	0.361
CuN ₄	release baseline	0.967	0.674	1.409	-0.537	-0.237	1.409

Limiting PCET = $\max(\Delta G_1, \Delta G_2)$ at 298.15 K and 0 V_{RHE}. The stepwise free energies are from the solvated explicit CHE treatment and define the final thermodynamic ranking discussed in the main text.

Table 1 promotes the rank-defining thermodynamic evidence into the main text by reporting the stepwise solvated CHE free energies for the final catalyst set. Those data show directly that favorable early proton-coupled electron transfer can coexist with severe CO overbinding, and they clarify why P-CoN₄ and CuN₄ are retained as chemically informative comparators rather than as leading motifs.

Solvation and explicit thermodynamics identify the leading motifs

Limited implicit solvation sharpens the distinction between the leading motifs and the comparators. B-CoN₄ moves to the best solvated electronic score (0.097 eV), followed by NiN₃B (0.239 eV), whereas CoN₄ and N-CoN₄ shift to 0.482 and 0.513 eV, respectively. P-CoN₄ remains strongly activation-favored on the early steps but does not recover as a balanced candidate. Direct extra-state calculations place it at the strong-adsorption edge of the shortlist, with $E_{\text{CO}_2,\text{ads}} = -1.439$ eV and $E_{\text{H,ads}} = -0.867$ eV under implicit solvation, while the non-P motifs retained in the final set remain endergonic for H adsorption in this limited-solvation

validation. These direct solvated DFT observables reinforce the view that P-CoN₄ sits on the overbinding side of the retained chemical space.

The decisive ranking emerges from the solvated explicit CHE analysis. By increasing limiting proton-coupled electron transfer cost, the retained motifs order as B-CoN₄ (0.015 eV), NiN₃B (0.062 eV), N-NiN₃B (0.080 eV), CoN₄ (0.118 eV), P-CoN₄ (0.211 eV), N-CoN₄ (0.361 eV), and CuN₄ (1.409 eV). Figure 3 recasts these data as catalysis-style stepwise free-energy diagrams, but the step-resolved values are equally important because they show how each motif distributes thermodynamic cost across COOH* formation, COOH* reduction, and CO release. B-CoN₄ and NiN₃B are both ΔG_1 -limited activation leaders, with $\Delta G_1 = 0.015$ and 0.062 eV and exergonic ΔG_2 values of -0.288 and -0.152 eV, respectively. Their advantage therefore comes from making COOH* formation accessible without converting the subsequent COOH* \rightarrow CO* proton-coupled electron transfer into the limiting step. Second-shell boron around Co is especially effective because it preserves the near-thermoneutral entry step of CoN₄ while shifting ΔG_2 from $+0.118$ eV for CoN₄ to -0.288 eV for B-CoN₄, even though the CO-release penalty rises from 0.512 to 0.908 eV.

N-NiN₃B occupies a different mechanistic niche. It remains formally ΔG_1 -limited (0.080 eV), but $\Delta G_2 = 0.045$ eV and $\Delta G_3 = 0.510$ eV show that its penalty is distributed much more evenly between COOH* formation and late-stage release. CoN₄, by contrast, is essentially thermoneutral for COOH* formation ($\Delta G_1 = 0.006$ eV) and becomes ΔG_2 -limited (0.118 eV), which explains why it remains a benchmark for balanced turnover rather than the strongest activation motif. N-CoN₄ pushes the same Co-based manifold farther toward the release-favored edge, lowering ΔG_3 to 0.110 eV but raising ΔG_1 to 0.361 eV. CuN₄ defines the easy-release boundary of the present dataset with $\Delta G_3 = -0.237$ eV, yet its $\Delta G_1 = 1.409$ eV makes initial COOH* formation prohibitively costly.

P-CoN₄ is the clearest counterexample to optimizing the first proton-coupled electron transfer step in isolation. Although $\Delta G_1 = -0.868$ eV, that over-stabilization converts the pathway into a deep intermediate well, leaving $\Delta G_2 = 0.211$ eV and a large CO-release

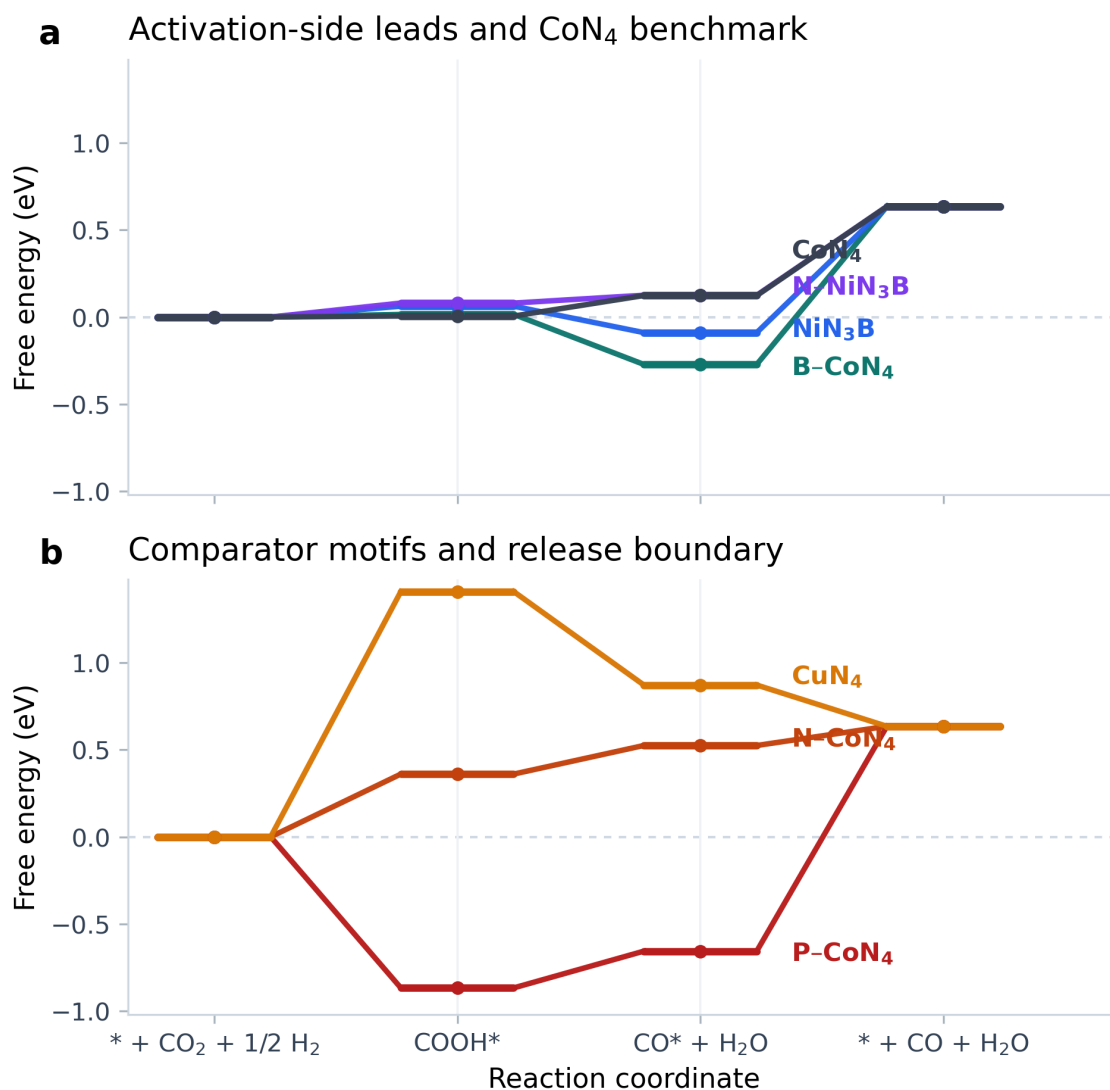


Figure 3: Solvated explicit free-energy diagrams for the final catalyst set at 298.15 K and 0 V_{RHE}. Panel (a) compares the leading activation-side motifs B-CoN₄ and NiN₃B with N-NiN₃B and the CoN₄ benchmark. Panel (b) collects the comparator motifs P-CoN₄, N-CoN₄, and CuN₄. Zero corresponds to * + CO₂ + 1/2 H₂. B-CoN₄ gives the smallest limiting proton-coupled electron transfer cost, N-NiN₃B narrows the gap to the NiN₃B parent while lowering the CO-release penalty, and P-CoN₄ forms the deepest bound intermediate well despite favorable early-step thermodynamics.

penalty of $\Delta G_3 = 1.292$ eV. The mechanistic distinction among the retained motifs is therefore not a single universal optimum but a redistribution of thermodynamic penalties among COOH* formation, COOH* reduction, and CO release, consistent with broader catalyst-design arguments that efficient CO₂-to-CO sites must balance intermediate formation against desorption rather than maximize one step alone.^{7,21}

Because no targeted transition-state barriers were computed for COOH* formation, COOH* reduction, or CO desorption, Figure 3 should be interpreted as a solvated thermodynamic landscape rather than as a complete kinetic mechanism. Even so, the descriptor-resolved separation is chemically informative: P-CoN₄ and CuN₄ are penalized for opposite reasons, whereas B-CoN₄, NiN₃B, N-NiN₃B, and CoN₄ occupy a narrower mechanistic corridor in which no single step becomes catastrophically uphill.

Held-out validated local alignment expands the Ni family without changing the evidence hierarchy

The aligned local model improves held-out agreement with DFT from 149.754 to 11.723 meV atom⁻¹ in energy MAE and from 0.10906 to 0.02699 eV Å⁻¹ in force MAE on the 1633-structure test set, while leaving the stress MAE effectively unchanged. Those gains justify using the aligned model to prioritize a narrow follow-up queue, but not to replace DFT as the source of quantitative catalyst comparisons.

That distinction matters most in the Ni family. The focused aligned-model scan nominated B-NiN₃B and N-NiN₃B for direct follow-up. DFT then separated the two motifs cleanly: N-NiN₃B enters the final catalyst set with a vacuum score of 0.232 eV, a solvated electronic score of 0.454 eV, and a solvated explicit limiting proton-coupled electron transfer cost of 0.080 eV, whereas B-NiN₃B showed strongly favorable H adsorption and was not advanced. The scientific value of the alignment step is therefore not surrogate-led ranking, but the DFT-backed identification of N-NiN₃B as a competitive Ni-family extension.

Coordination-level design rules from the DFT-arbitrated set

Taken together, the step-resolved solvated CHE data do more than rank motifs; they define three portable coordination-level principles for this graphene MN_4 family. First, beneficial activation-side tuning is not equivalent to simply maximizing $COOH^*$ binding: the best motifs keep $\max(\Delta G_1, \Delta G_2)$ near zero without creating the deep CO^* well exemplified by P-CoN₄. Second, second-shell modification can be decisive when it selectively reshapes the balance between ΔG_1 and ΔG_2 while preserving the MN_4 pocket. B-CoN₄ illustrates this point by retaining near-thermoneutral $COOH^*$ formation while rendering the $COOH^*$ reduction step exergonic, which is why it outperforms the CoN₄ benchmark on limiting proton-coupled electron transfer despite a larger release penalty. Third, boron-containing NiN₃ coordination is intrinsically competitive, and heteroatom tuning within that local pocket moves the motif along the activation-versus-release axis rather than improving every step monotonically. NiN₃B sits closer to the activation extreme, whereas N-NiN₃B sacrifices little limiting proton-coupled electron transfer while cutting the CO-release penalty from 0.725 to 0.510 eV, a direction consistent with prior reports that low-coordinate and heteroatom-modified Ni single sites can improve CO₂-to-CO catalysis.^{22,23}

The clearest negative design rule concerns phosphorus within the present Co-based template. P-CoN₄ does not fail because the early steps are weak; it fails because strong early stabilization is coupled to a deep late-intermediate well and a large CO-release penalty on both the limited-solvation electronic scale and the solvated explicit free-energy scale. Within the retained main-text set, the chemically useful corridor is therefore bounded on one side by P-CoN₄-style overbinding and on the other by N-CoN₄/CuN₄-style underactivation.

Conclusions

Solvated thermodynamics identify a chemically coherent leading set for graphene-supported MN_4 single-atom catalysts for two-electron CO₂ reduction to CO. B-CoN₄ is the strongest

supported activation-side motif, NiN₃B is the closest overall competitor, and N–NiN₃B is a validated third-ranked Ni-family extension discovered through targeted follow-up and confirmed by DFT. CoN₄ and N–CoN₄ define the more release-favored edge of the retained landscape, CuN₄ remains the easy-CO-release boundary, and P–CoN₄ serves as a chemically instructive overbinding comparator.

The central design message is therefore not a single descriptor optimum but a local-coordination redistribution of ΔG_1 , ΔG_2 , and ΔG_3 . Second-shell boron around Co lowers the limiting proton-coupled electron transfer primarily by relieving the COOH* \rightarrow CO* step while keeping COOH* formation nearly thermoneutral, whereas boron-containing NiN₃ motifs define a parallel Ni-centered activation manifold whose release penalty can be moderated further by second-shell nitrogen. The chemically useful corridor is therefore bounded by P–CoN₄-style CO* trapping on one side and N–CoN₄/CuN₄-style underactivation on the other. Within this thermodynamic map, the B–CoN₄/NiN₃B/N–NiN₃B trio defines the most promising motif family presently supported by the retained DFT and thermodynamic evidence.

Associated Content

Supporting Information. A Supporting Information PDF accompanies this manuscript and contains the full 35-motif vacuum DFT ranking table, extended shortlist and extra-state validation tables, complementary thermodynamic plots, aligned-model validation metrics, DFT follow-up for aligned-model suggestions, QC notes, and coordinates/data-availability details.

Data Availability

All data supporting the findings of this study are provided within the manuscript and Supporting Information. Additional structure files, derived tables, and electronic-structure out-

puts supporting the DFT primary matrix, solvation validation, aligned follow-up, and explicit thermochemistry analyses are available from the authors upon reasonable request.

Author Information

Metadata required before submission

Author names, institutional affiliations, and corresponding-author contact information are to be inserted by the authors before submission.

Notes

The authors declare no competing financial interest.

Acknowledgments

Funding information, computational-resource acknowledgments, and any project-specific acknowledgments are to be supplied by the authors before submission.

References

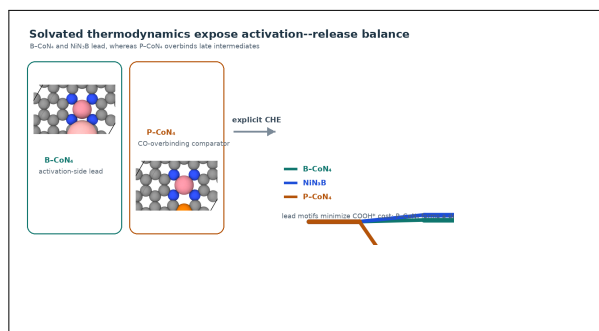
- (1) Ju, W.; Bagger, A.; Hao, G.-P.; Varela, A. S.; Sinev, I.; Bon, V.; Roldan Cuenya, B.; Kaskel, S.; Rossmeisl, J.; Strasser, P. Understanding activity and selectivity of metal-nitrogen-doped carbon catalysts for electrochemical reduction of CO₂. *Nature Communications* **2017**, *8*.
- (2) Paul, S.; Kao, Y.-L.; Ni, L.; Ehnert, R.; Herrmann-Geppert, I.; van de Krol, R.; Stark, R. W.; Jaegermann, W.; Kramm, U. I.; Bogdanoff, P. Influence of the Metal Center in M–N–C Catalysts on the CO₂ Reduction Reaction on Gas Diffusion Electrodes. *ACS Catalysis* **2021**, *11*, 5850–5864.

- (3) Li, X.; Bi, W.; Chen, M.; Sun, Y.; Ju, H.; Yan, W.; Zhu, J.; Wu, X.; Chu, W.; Wu, C.; Xie, Y. Exclusive Ni–N₄ Sites Realize Near-Unity CO Selectivity for Electrochemical CO₂ Reduction. *Journal of the American Chemical Society* **2017**, *139*, 14889–14892.
- (4) Jiang, K.; Siahrostami, S.; Zheng, T.; Hu, Y.; Hwang, S.; Stavitski, E.; Peng, Y.; Dynes, J.; Gangisetty, M.; Su, D.; Attenkofer, K.; Wang, H. Isolated Ni single atoms in graphene nanosheets for high-performance CO₂ reduction. *Energy & Environmental Science* **2018**, *11*, 893–903.
- (5) Yang, H. B. et al. Atomically dispersed Ni(I) as the active site for electrochemical CO₂ reduction. *Nature Energy* **2018**, *3*, 140–147.
- (6) Pan, Y. et al. Design of Single-Atom Co–N₅ Catalytic Site: A Robust Electrocatalyst for CO₂ Reduction with Nearly 100% and Remarkable Stability. *Journal of the American Chemical Society* **2018**, *140*, 4218–4221.
- (7) Vijay, S.; Ju, W.; Bruckner, S.; Tsang, S.-C.; Strasser, P.; Chan, K. Unified mechanistic understanding of CO₂ reduction to CO on transition metal and single atom catalysts. *Nature Catalysis* **2021**, *4*, 1024–1031.
- (8) Wang, X.; Chen, Z.; Zhao, X.; Yao, T.; Chen, W.; You, R.; Zhao, C.; Wu, G.; Wang, J.; Huang, W.; Yang, J.; Hong, X.; Wei, S.; Wu, Y.; Li, Y. Regulation of Coordination Number over Single Co Sites: Triggering the Efficient Electroreduction of CO₂. *Angewandte Chemie International Edition* **2018**, *57*, 1944–1948.
- (9) Pei, J.; Shang, H.; Mao, J.; Chen, Z.; Sui, R.; Zhang, X.; Zhou, D.; Wang, Y.; Zhang, F.; Zhu, W.; Wang, T.; Chen, W.; Zhuang, Z. A replacement strategy for regulating local environment of single-atom Co–S_xN_{4–x} catalysts to facilitate CO₂ electroreduction. *Nature Communications* **2024**, *15*.
- (10) Takele Menisa, L.; Cheng, P.; Qiu, X.; Zheng, Y.; Huang, X.; Gao, Y.; Tang, Z. Single

- atomic Fe-N₄ active sites and neighboring graphitic nitrogen for efficient and stable electrochemical CO₂ reduction. *Nanoscale Horizons* **2022**, *7*, 916–923.
- (11) Cui, Y.; Ren, C.; Wu, M.; Chen, Y.; Li, Q.; Ling, C.; Wang, J. Structure–Stability Relation of Single-Atom Catalysts under Operating Conditions of CO₂ Reduction. *Journal of the American Chemical Society* **2024**, *146*, 29169–29176.
- (12) Li, K.; Zhang, S.; Zhang, X.; Liu, S.; Jiang, H.; Jiang, T.; Shen, C.; Yu, Y.; Chen, W. Atomic Tuning of Single-Atom Fe–N–C Catalysts with Phosphorus for Robust Electrochemical CO₂ Reduction. *Nano Letters* **2022**, *22*, 1557–1565.
- (13) Batatia, I. et al. A foundation model for atomistic materials chemistry. *The Journal of Chemical Physics* **2025**, *163*.
- (14) Kresse, G.; Furthmüller, J. Efficient iterative schemes for ab initio total-energy calculations using a plane-wave basis set. *Physical Review B* **1996**, *54*, 11169–11186.
- (15) Kresse, G.; Joubert, D. From ultrasoft pseudopotentials to the projector augmented-wave method. *Physical Review B* **1999**, *59*, 1758–1775.
- (16) Perdew, J. P.; Burke, K.; Ernzerhof, M. Generalized Gradient Approximation Made Simple. *Physical Review Letters* **1996**, *77*, 3865–3868.
- (17) Grimme, S.; Ehrlich, S.; Goerigk, L. Effect of the damping function in dispersion corrected density functional theory. *Journal of Computational Chemistry* **2011**, *32*, 1456–1465.
- (18) Mathew, K.; Sundararaman, R.; Letchworth-Weaver, K.; Arias, T. A.; Hennig, R. G. Implicit solvation model for density-functional study of nanocrystal surfaces and reaction pathways. *The Journal of Chemical Physics* **2014**, *140*, 084106.
- (19) Nørskov, J. K.; Rossmeisl, J.; Logadottir, A.; Lindqvist, L.; Kitchin, J. R.; Bligaard, T.;

- Jonsson, H. Origin of the Overpotential for Oxygen Reduction at a Fuel-Cell Cathode. *The Journal of Physical Chemistry B* **2004**, *108*, 17886–17892.
- (20) Wang, V.; Xu, N.; Liu, J.-C.; Tang, G.; Geng, W. T. VASPKIT: A user-friendly interface facilitating high-throughput computing and analysis using VASP code. *Computer Physics Communications* **2021**, *267*, 108033.
- (21) Zhou, Y.; Zhou, Q.; Liu, H.; Xu, W.; Wang, Z.; Qiao, S.; Ding, H.; Chen, D.; Zhu, J.; Qi, Z.; Wu, X.; He, Q.; Song, L. Asymmetric dinitrogen-coordinated nickel single-atomic sites for efficient CO₂ electroreduction. *Nature Communications* **2023**, *14*, 3776.
- (22) Song, J.; Lei, X.; Mu, J.; Li, J.; Song, X.; Yan, L.; Ding, Y. Boron-Doped Nickel-Nitrogen-Carbon Single-Atom Catalyst for Boosting Electrochemical CO₂ Reduction. *Small* **2023**, *19*, 2305666.
- (23) Zhang, Y.; Jiao, L.; Yang, W.; Xie, C.; Jiang, H.-L. Rational Fabrication of Low-Coordinate Single-Atom Ni Electrocatalysts by MOFs for Highly Selective CO₂ Reduction. *Angewandte Chemie International Edition* **2021**, *60*, 7607–7611.

TOC Graphic



6.5 SAC Supporting Information

The following pages reproduce the original SAC Supporting Information produced by CatMaster from `Materials/project_space/SAC_New/files/writing/co2rr_sac_submission_grade/supporting_information.pdf`. The corresponding archived source file is `Materials/project_space/SAC_New/files/writing/co2rr_sac_submission_grade/supporting_information.tex`.

Supporting Information for “Solvated Thermodynamics of Graphene-Supported MN_4 Single-Atom Catalysts Identify B– CoN_4 and NiN_3B as Leading CO_2 -to- CO Motifs”

Author metadata to be supplied before submission

Institutional affiliations to be supplied before submission

E-mail:

Computational Details

The manuscript combines four evidence layers: motif exploration on a common graphene-supported MN_4 template, a 35-motif vacuum DFT arbitration matrix, limited implicit-solvation validation on the retained shortlist, and explicit adsorbate-frequency CHE analysis for the final catalyst set. The initial exploration used the MACE *mh-1* model with dispersion-inclusive relaxations on pristine motifs, first-shell substitutions, second-shell substitutions, and a limited combined-shell follow-up.¹ That stage is used only to map the design space and to prioritize targeted follow-up.

The primary DFT matrix contains five pristine motifs, fifteen single first-shell substitutions, and fifteen single second-shell substitutions. Twelve of those thirty-five motifs were not part of the initial MACE stage and therefore broaden the catalyst comparison beyond the exploratory surrogate space. All slab calculations used the retained spin-polarized PAW-PBE, fixed-cell, dispersion-inclusive VASP setup described in the main text.^{2–5} Structural

retention required convergence of bare, COOH*, and CO* states together with preservation of the intended four-anchor pocket.

Implicit solvation used `LSOL = True`, `EB_K = 78.4`, and `TAU = 5.25e-4`.⁶ The initial validation covered B-CoN₄, NiN₃B, CoN₄, N-CoN₄, B-CuN₄, CuN₄, and P-CoN₄ for bare, CO₂*, COOH*, CO*, and H-on-anchor states. N-NiN₃B was later placed on the same footing with five additional solvated calculations. Asterisk-filled SOL: counters in some VASPsol outputs prevented reliable extraction from the stock XML parser, so solvated energies were taken from final OSZICAR records. In the original seven-motif validation, 34 of 35 jobs returned status code 0 with the standard ionic-convergence phrase; the only exception was B-CoN₄ bare, for which the reported energy came from a rescue static calculation on the final solvated geometry after a late ZBRENT bracketing failure.

The explicit thermochemistry package retained B-CoN₄, NiN₃B, CoN₄, N-CoN₄, CuN₄, and P-CoN₄, together with a later two-frequency-job extension for N-NiN₃B. CHE conditions were 298.15 K and 0 V_{RHE}.⁷ Here “solvated explicit” denotes implicit-solvation electronic energies combined with explicit adsorbate vibrational corrections within CHE; no explicit solvent molecules were included. COOH* and CO* corrections came from adsorbate-only finite-difference frequency calculations processed with VASPKIT, while gas references were shared across the package.⁸ The direct limited-solvation observables $E_{\text{H,ads}}$ and $E_{\text{CO}_2,\text{ads}}$ are therefore distinct from the derived mixed-source ΔG_{H} and $\Delta G_{\text{CO}_2,\text{ads}}$ columns used only as contextual descriptors in the explicit thermochemistry tables.

The local alignment repair was assessed on a held-out 1633-structure test set and then used for a focused Co/Ni N₃B-family prioritization exercise. The repaired v3 aligned model completed cleanly and serves as the authoritative local surrogate for that follow-up scan. The focused aligned-model relaxation campaign completed 33 of 34 structures to the requested force threshold; the single unconverged case was CO₂/B-NiN₃B.

Primary-Matrix DFT Arbitration

The full vacuum DFT ranking of the 35-motif primary matrix is provided in Table S1. Twenty-one motifs satisfy the structural-retention criterion. The highest-ranked stable motifs in the primary matrix are CoN₄, N-CoN₄, NiN₃B, B-CoN₄, and B-CuN₄, whereas the P-containing motifs consistently move toward the overbinding side of the descriptor space because strongly favorable ΔE_1 values are paired with large ΔE_3 penalties.

Table S1: Vacuum DFT arbitration across the 35-motif primary matrix. Scores use the manuscript screening descriptor on the DFT electronic energies; lower values are better.

Rank	Motif	Family	Stable	Score (eV)	ΔE_1 (eV)	ΔE_2 (eV)	ΔE_3 (eV)
1	CoN4	pristine	Yes	0.246	-0.460	0.246	0.937
2	N_CoN4	second_shell	Yes	0.329	-0.187	0.329	0.581
3	NiN3B	first_shell	Yes	0.428	-0.495	-0.010	1.228
4	B_CoN4	second_shell	Yes	0.553	-0.489	-0.141	1.353
5	B_CuN4	second_shell	Yes	0.589	0.589	-0.234	0.367
6	B_NiN4	second_shell	Yes	0.643	0.643	-0.124	0.205
7	N_FeN4	second_shell	Yes	0.795	-0.527	-0.344	1.595
8	B_FeN4	second_shell	Yes	0.823	-0.288	-0.611	1.623
9	FeN4	pristine	Yes	0.854	-0.314	-0.617	1.654
10	CoN3S	first_shell	Yes	0.860	-0.960	0.023	1.660
11	NiN4	pristine	Yes	0.917	0.917	-0.381	0.187
12	N_NiN4	second_shell	Yes	0.961	0.961	-0.427	0.190
13	CuN4	pristine	Yes	0.967	0.967	-0.407	0.163
14	P_CoN4	second_shell	Yes	1.036	-1.410	0.297	1.836
15	CuN3B	first_shell	Yes	1.172	-0.660	1.172	0.211
16	CoN3P	first_shell	Yes	1.355	-1.210	-0.222	2.155

Rank	Motif	Family	Stable	Score (eV)	ΔE_1 (eV)	ΔE_2 (eV)	ΔE_3 (eV)
17	FeN3B	first_shell	Yes	1.377	-0.859	-0.595	2.177
18	CoN3B	first_shell	Yes	1.520	-1.089	-0.507	2.320
19	FeN3S	first_shell	Yes	1.775	-1.423	-0.428	2.575
20	FeN3P	first_shell	Yes	2.053	-1.536	-0.594	2.853
21	P_FeN4	second_shell	Yes	2.164	-1.878	-0.363	2.964
22	NiN3P	first_shell	No	2.407	-0.219	-0.235	1.177
23	ZnN4	pristine	No	2.459	0.249	0.223	0.251
24	B_ZnN4	second_shell	No	2.481	0.082	0.294	0.347
25	ZnN3B	first_shell	No	2.827	-0.297	0.414	0.606
26	N_ZnN4	second_shell	No	2.943	-0.236	0.679	0.280
27	NiN3S	first_shell	No	2.955	-0.372	-0.517	1.613
28	P_NiN4	second_shell	No	3.022	-0.518	-0.554	1.795
29	N_CuN4	second_shell	No	3.043	0.719	-0.795	0.800
30	P_ZnN4	second_shell	No	3.251	-1.759	0.659	1.822
31	CuN3P	first_shell	No	3.684	-0.875	-0.511	2.110
32	ZnN3P	first_shell	No	3.717	-1.844	0.477	2.091
33	P_CuN4	second_shell	No	3.847	-0.677	-0.966	2.366
34	ZnN3S	first_shell	No	4.024	-2.254	0.545	2.433
35	CuN3S	first_shell	No	4.130	-1.036	-0.758	2.518

Shortlist Extra States and Limited-Solvation Validation

The final catalyst shortlist was assembled by combining the vacuum primary-matrix ranking with direct DFT checks for CO₂* and H-on-anchor adsorption. That logic preserved CoN₄, N-CoN₄, NiN₃B, B-CoN₄, and B-CuN₄ as primary leads, kept CuN₄ as the easy-release baseline, and retained P-CoN₄ as a chemically informative overbinding comparator. P-NiN₄ was not advanced because

it failed the structural criterion in the unified vacuum DFT table and also showed favorable H adsorption.

Table S2 summarizes the vacuum-to-solvated descriptor changes for the retained shortlist plus N-NiN₃B. B-CuN₄ remains documented here because it was a vacuum-competitive context motif, but it is not part of the final explicit free-energy package and is therefore excluded from the main-text catalyst set.

Table S2: Vacuum and limited-solvation electronic descriptors for the manuscript-facing shortlist and the B_CuN₄ context motif.

Motif	Vacuum score (eV)	Solvated score (eV)	$E_{\text{CO}_2,\text{ads}}^{\text{solv}}$ (eV)	$E_{\text{H},\text{ads}}^{\text{solv}}$ (eV)	Solvated rank	Role
B_CoN4	0.553	0.097	-0.374	0.440	1	final shortlist
NiN3B	0.428	0.239	-0.269	0.676	2	final shortlist
N_NiN3B	0.232	0.454	-0.268	0.670	3	validated new entry
CoN4	0.246	0.482	-0.349	0.638	4	final shortlist
N_CoN4	0.329	0.513	-0.274	1.100	5	final shortlist
CuN4	0.967	0.674	-0.205	0.749	7	baseline
P_CoN4	1.036	0.581	-1.439	-0.867	6	P-doped comparator
B_CuN4	0.589	0.685	-0.247	0.443	7	drops under solvation

Explicit Thermochemistry Package

The solvated explicit free-energy data used for the manuscript-level ranking are summarized in Table S3. The limiting proton-coupled electron transfer ordering is B-CoN₄ < NiN₃B < N-NiN₃B < CoN₄ < P-CoN₄ < N-CoN₄ \ll CuN₄. The main text carries the journal-style free-energy diagrams and the selected catalyst summary table; the figures here provide complementary whole-set and auxiliary thermodynamic views.

Table S3: Explicit thermochemistry summary for the retained catalyst set. Auxiliary ΔG_{H} and $\Delta G_{\text{CO}_2,\text{ads}}$ remain mixed-source quantities and are contextual only.

Motif	Phase	ΔG_1 (eV)	ΔG_2 (eV)	ΔG_3 (eV)	Limiting PCET (eV)	ΔG_{H} (eV)	$\Delta G_{\text{CO}_2,\text{ads}}$ (eV)
B_CoN4	vacuum	0.311	-0.525	0.850	0.311	0.842	0.192
B_CoN4	solvated	0.015	-0.288	0.908	0.015	0.682	0.015
NiN3B	vacuum	0.321	-0.401	0.715	0.321	1.030	0.195
NiN3B	solvated	0.062	-0.152	0.725	0.062	0.919	0.120
N_NiN3B	vacuum	0.308	-0.177	0.504	0.308	1.028	0.185
N_NiN3B	solvated	0.080	0.045	0.510	0.080	0.912	0.120
CoN4	vacuum	0.346	-0.118	0.408	0.346	1.001	0.207
CoN4	solvated	0.006	0.118	0.512	0.118	0.880	0.040
N_CoN4	vacuum	0.597	-0.019	0.058	0.597	1.364	0.178
N_CoN4	solvated	0.361	0.164	0.110	0.361	1.342	0.115
CuN4	vacuum	1.702	-0.813	-0.254	1.702	1.134	0.279
CuN4	solvated	1.409	-0.537	-0.237	1.409	0.991	0.184
P_CoN4	vacuum	-0.598	-0.073	1.306	-0.073	-0.667	-1.009
P_CoN4	solvated	-0.868	0.211	1.292	0.211	-0.625	-1.050

For the N–NiN₃B extension, the two adsorbate-only frequency jobs both completed successfully and no imaginary adsorbate-only modes were detected for either COOH* or CO*. The explicit adsorbate corrections for N–NiN₃B remain close to the parent NiN₃B values, with 0.539 eV for COOH* and 0.110 eV for CO*.

Aligned-Model Validation and Follow-up

Held-out metrics for the baseline and aligned models are listed in Table S4. The archived alignment dataset contains 11 859 training, 1233 validation, and 1633 held-out test configurations drawn from

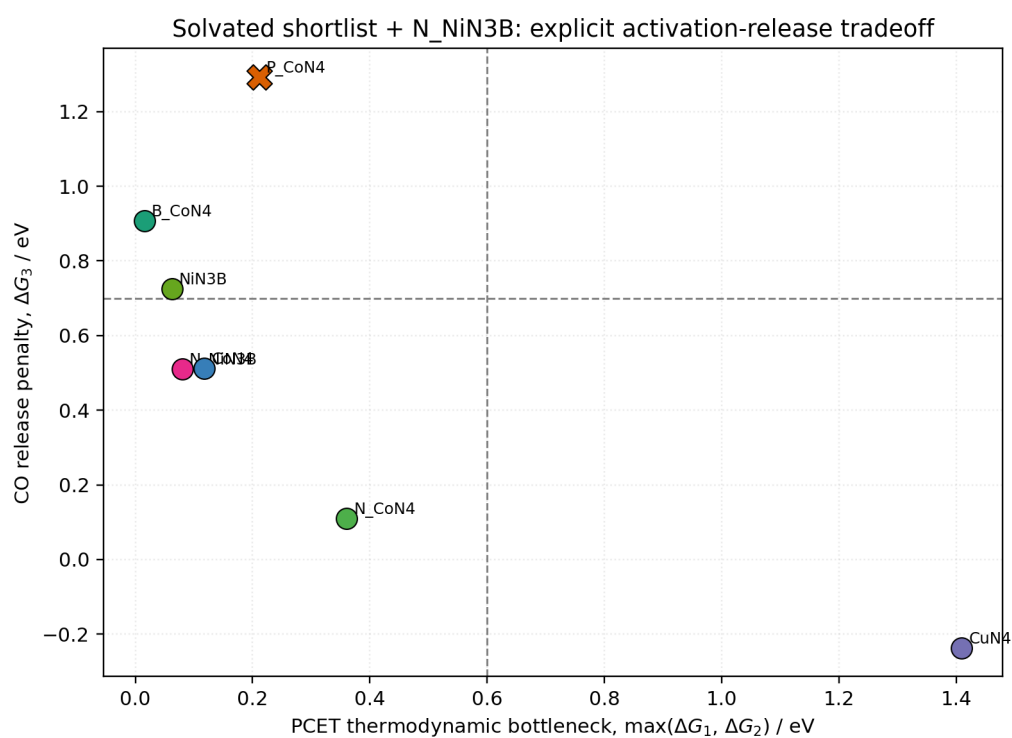


Figure S1: Activation-versus-release map from the solvated explicit CHE analysis at 298.15 K and 0 V_{RHE} . The horizontal axis is $\max(\Delta G_1, \Delta G_2)$ and the vertical axis is ΔG_3 . The plot complements the main-text free-energy diagrams by showing the same thermodynamic ordering as a two-descriptor landscape.

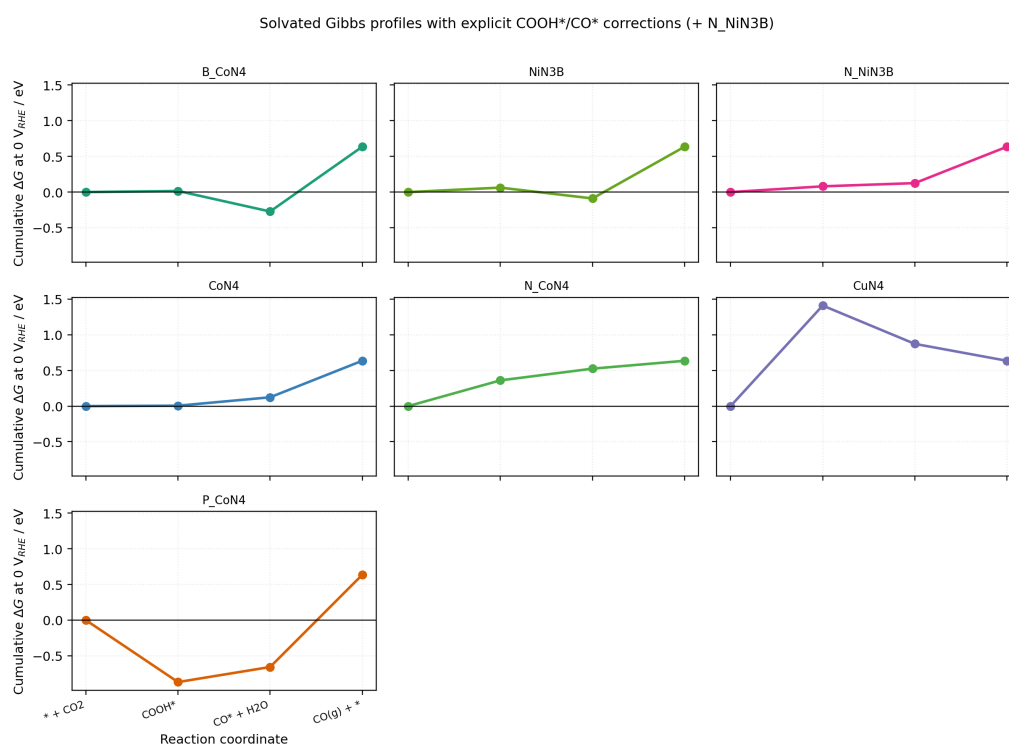


Figure S2: Full retained-set free-energy profiles from the solvated explicit CHE package. This plot complements the main-text catalysis-style diagrams by showing all retained motifs on one common energy axis.

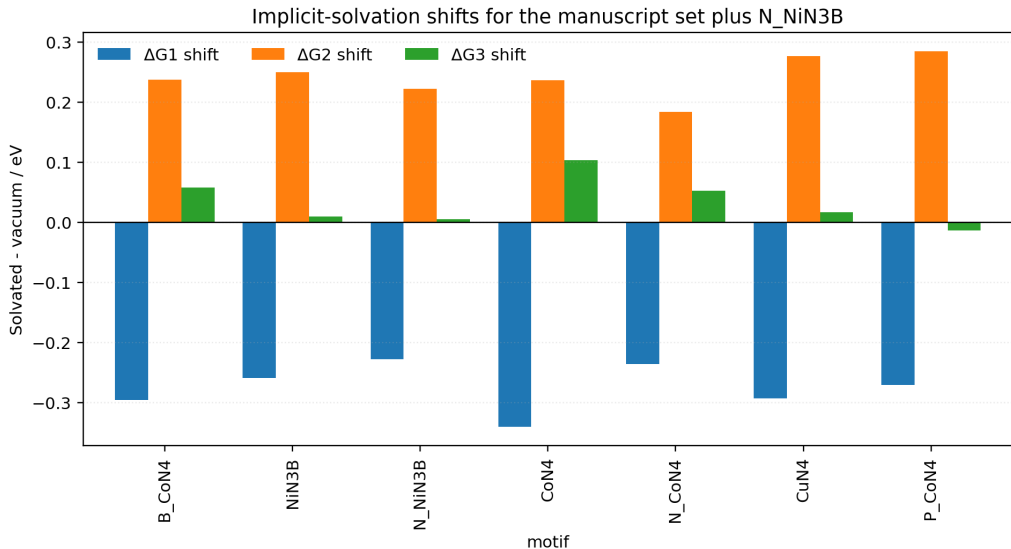


Figure S3: Step-resolved solvent-induced shifts from the explicit thermochemistry package after inclusion of N-NiN₃B. The plot shows how the limited-solvation and explicit-correction treatment reshapes the relative COOH*, CO*, and CO-release terms across the retained catalyst set.

the DFT relaxation and extra-state set, and the successful v3-repair aligned model is the authoritative artifact used unchanged for the focused follow-up scan reported here. The aligned model improves energy and force accuracy by 12.8 \times and 4.0 \times , respectively, relative to the baseline model, while stress accuracy is essentially unchanged. This improvement is sufficient to justify targeted prioritization in a narrow chemical neighborhood, but it is not used in place of DFT for any final catalyst claim.

Table S4: Held-out test-set metrics for the baseline and aligned MACE models on 1633 structures.

Model	Energy MAE (meV/atom)	Force MAE (eV/Å)	Stress MAE (eV/Å ³)	Frames
Baseline mh-1	149.754	0.109	0.001623	1633
Aligned mh-1 v3	11.723	0.027	0.001614	1633

DFT follow-up for the two aligned-model suggestions is summarized in Table S5. N-NiN₃B is the only promoted motif. B-NiN₃B was not added to the final catalyst set because its favorable H adsorption indicates a strong H-binding signature despite a competitive core-state vacuum score.

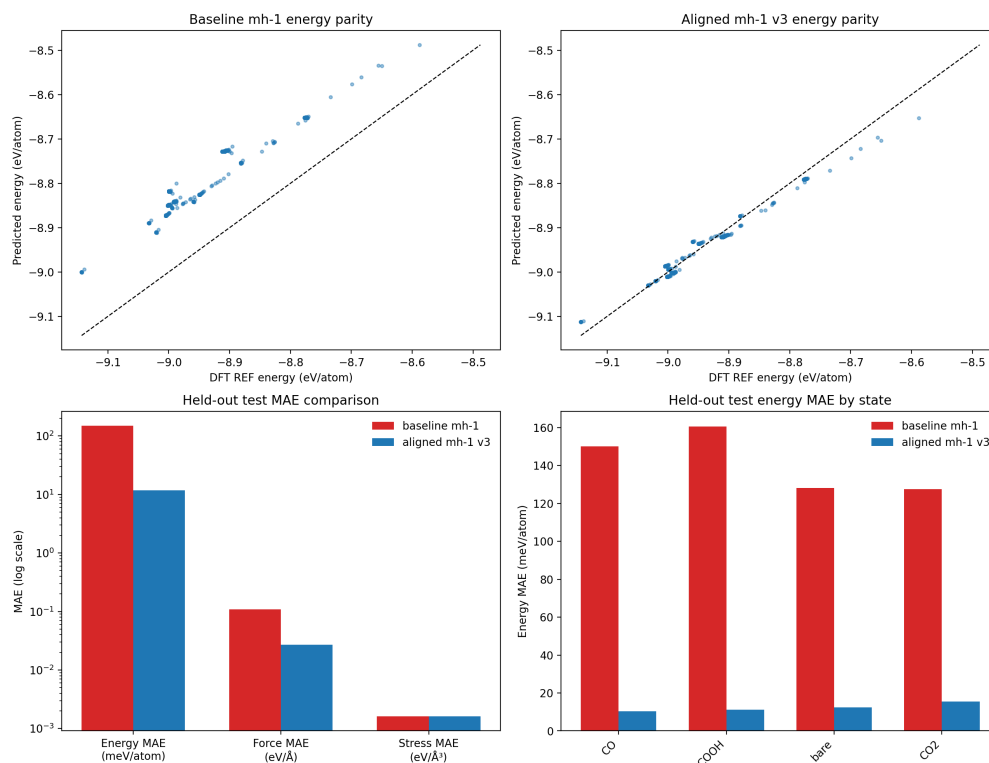


Figure S4: Held-out parity comparison for the baseline and aligned models on the authoritative test set. Local alignment substantially tightens the energy and force agreement relative to the baseline model, supporting its use for targeted follow-up rather than final catalyst ranking.

Table S5: DFT follow-up for aligned-model suggestions in the NiN₃B family.

Motif	Vacuum score (eV)	ΔE_1 (eV)	ΔE_2 (eV)	ΔE_3 (eV)	$E_{H,ads}$ (eV)	Decision
B_NiN ₃ B	0.511	-0.811	0.223	1.311	-1.023	Rejected
N_NiN ₃ B	0.232	-0.513	0.232	1.004	0.786	Promoted

QC Notes, Parser Details, Coordinates, and Data Availability

The most important QC notes for peer review are collected here.

- Vacuum DFT primary-matrix conclusions are based on converged bare, COOH*, and CO* states for the full 35-motif matrix, with the structural-retention criterion used to distinguish the 21 stable motifs from off-plane or coordination-loss cases.
- In the original limited-solvation validation, 34 of 35 jobs returned status code 0 and included the standard ionic-convergence phrase. B-CoN₄ bare required a rescue static calculation on the final solvated geometry after a late ZBRENT failure.
- Final solvated energies were taken from OSZICAR records whenever asterisk-filled SOL: counters prevented reliable extraction from the stock XML parser.
- The N-NiN₃B solvation extension returned 5 of 5 converged jobs with the same OSZICAR-based energy parsing used for the base solvated set.
- The explicit thermochemistry extension for N-NiN₃B returned 2 of 2 collected-complete frequency jobs with no imaginary adsorbate-only modes.
- The focused aligned-model scan completed 33 of 34 requested relaxations; the only unconverged case was CO₂/B-NiN₃B.

Primary narrative summaries and derived tables are organized with the manuscript package and its supporting calculation folders. The retained figures, helper tables, coordinate files, manifests, and electronic-structure outputs are sufficient to reproduce the ranking tables reported in the manuscript and Supporting Information, and can be supplied by the authors upon reasonable request.

References

- (1) Batatia, I. et al. A foundation model for atomistic materials chemistry. *The Journal of Chemical Physics* **2025**, *163*.

- (2) Kresse, G.; Furthmüller, J. Efficient iterative schemes for ab initio total-energy calculations using a plane-wave basis set. *Physical Review B* **1996**, *54*, 11169–11186.
- (3) Kresse, G.; Joubert, D. From ultrasoft pseudopotentials to the projector augmented-wave method. *Physical Review B* **1999**, *59*, 1758–1775.
- (4) Perdew, J. P.; Burke, K.; Ernzerhof, M. Generalized Gradient Approximation Made Simple. *Physical Review Letters* **1996**, *77*, 3865–3868.
- (5) Grimme, S.; Ehrlich, S.; Goerigk, L. Effect of the damping function in dispersion corrected density functional theory. *Journal of Computational Chemistry* **2011**, *32*, 1456–1465.
- (6) Mathew, K.; Sundararaman, R.; Letchworth-Weaver, K.; Arias, T. A.; Hennig, R. G. Implicit solvation model for density-functional study of nanocrystal surfaces and reaction pathways. *The Journal of Chemical Physics* **2014**, *140*, 084106.
- (7) Nørskov, J. K.; Rossmeisl, J.; Logadottir, A.; Lindqvist, L.; Kitchin, J. R.; Bligaard, T.; Jonsen, H. Origin of the Overpotential for Oxygen Reduction at a Fuel-Cell Cathode. *The Journal of Physical Chemistry B* **2004**, *108*, 17886–17892.
- (8) Wang, V.; Xu, N.; Liu, J.-C.; Tang, G.; Geng, W. T. VASPKIT: A user-friendly interface facilitating high-throughput computing and analysis using VASP code. *Computer Physics Communications* **2021**, *267*, 108033.

References

- [1] Mavroudis, V. Langchain (2024).
- [2] LangChain. Deep agents overview (2026). URL <https://docs.langchain.com/oss/python/deepagents/overview>. Accessed March 27, 2026.